FINAL REPORT

Large-Scale Laboratory Experiments of Incipient Motion, Transport, and Fate of Underwater Munitions under Waves, Currents, and Combined-Flows

SERDP Project MR-2410

APRIL 2018

Marcelo H. Garcia, PhD
Blake J. Landry, PhD
University of Illinois at Urbana-Champaign

Distribution Statement A
This document has been cleared for public release

SERDP
DOD ▪ EPA ▪ DOE

Page Intentionally Left Blank

This report was prepared under contract to the Department of Defense Strategic Environmental Research and Development Program (SERDP). The publication of this report does not indicate endorsement by the Department of Defense, nor should the contents be construed as reflecting the official policy or position of the Department of Defense. Reference herein to any specific commercial product, process, or service by trade name, trademark, manufacturer, or otherwise, does not necessarily constitute or imply its endorsement, recommendation, or favoring by the Department of Defense.

Page Intentionally Left Blank

REPORT DOCUMENTATION PAGE

Form Approved
OMB No. 0704-0188

The public reporting burden for this collection of information is estimated to average 1 hour per response, including the time for reviewing instructions, searching existing data sources, gathering and maintaining the data needed, and completing and reviewing the collection of information. Send comments regarding this burden estimate or any other aspect of this collection of information, including suggestions for reducing the burden, to Department of Defense, Washington Headquarters Services, Directorate for Information Operations and Reports (0704-0188), 1215 Jefferson Davis Highway, Suite 1204, Arlington, VA 22202-4302. Respondents should be aware that notwithstanding any other provision of law, no person shall be subject to any penalty for failing to comply with a collection of information if it does not display a currently valid OMB control number.
PLEASE DO NOT RETURN YOUR FORM TO THE ABOVE ADDRESS.

1. REPORT DATE *(DD-MM-YYYY)*	2. REPORT TYPE	3. DATES COVERED *(From - To)*
04/25/2018	SERDP Final Report	7/1/2014 - 7/1/2018

4. TITLE AND SUBTITLE
Large-Scale Laboratory Experiments of Incipient Motion, Transport, and Fate of Underwater Munitions under Waves, Currents, and Combined-Flows

5a. CONTRACT NUMBER
Contract: 14-C-0032

5b. GRANT NUMBER

5c. PROGRAM ELEMENT NUMBER

6. AUTHOR(S)
Marcelo H. Garcia, PhD
Blake J. Landry, PhD

5d. PROJECT NUMBER
MR-2410

5e. TASK NUMBER

5f. WORK UNIT NUMBER

7. PERFORMING ORGANIZATION NAME(S) AND ADDRESS(ES)
University of Illinois at Urbana-Champaign
Department of Civil and Environmental Engineering
205 North Mathews Avenue
Urbana, IL 61801

8. PERFORMING ORGANIZATION REPORT NUMBER
MR-2410

9. SPONSORING/MONITORING AGENCY NAME(S) AND ADDRESS(ES)
Strategic Environmental Research and Development Program
4800 Mark Center Drive, Suite 17D03
Alexandria, VA 22350-3605

10. SPONSOR/MONITOR'S ACRONYM(S)
SERDP

11. SPONSOR/MONITOR'S REPORT NUMBER(S)
MR-2410

12. DISTRIBUTION/AVAILABILITY STATEMENT
Distribution A; unlimited public release

13. SUPPLEMENTARY NOTES

14. ABSTRACT
This project looks at the need to improve the understanding of the phenomenology of entrainment, transport and fate of underwater munitions. A recent white paper identified several knowledge gaps in the predictive skill of munitions mobility models. This research effort aligns to address these gaps in environments with hard bottom substrates. Ultimately, the fundamental work herein provides a critical data set and initiation of motion predictors to improve existing field scale models for munitions mobility (i.e., Underwater Munitions Expert System, UnMES; Rennie and Brandt, 2015) that are difficult or practically impossible to obtain with existing field measurements.

15. SUBJECT TERMS
Initiation of Motion of Munitions, Motion Tracking, Munition Migration, Oscillatory Flow, Particle Image Velocimetry, Physical Laboratory Experiments, Unidirectional Flow

16. SECURITY CLASSIFICATION OF:			17. LIMITATION OF ABSTRACT	18. NUMBER OF PAGES	19a. NAME OF RESPONSIBLE PERSON
a. REPORT	b. ABSTRACT	c. THIS PAGE			Marcelo Garcia
UNCLASS	UNCLASS	UNCLASS	UNCLASS	117	19b. TELEPHONE NUMBER *(Include area code)* 217-244-4484

Page Intentionally Left Blank

Table of Contents

Table of Contents ii
List of Tables iii
List of Figures iv
List of Acronyms vii
Keywords viii
Acknowledgements viii
1. Abstract 9
2. Objective 9
3. Background 10
4. Technical Approach 17
4.1 Range of Surrogate Munitions Test Subjects 18
4.2 Initiation of Motion Experiments 22
4.2.1 Procedure for Unidirectional Flow Experiments 24
4.2.2 Procedure for Oscillatory Flow Experiments 26
5. Results and Discussion 26
5.1 Unidirectional Flows 26
5.2 Oscillatory Flows 34
5.3 Unified Scaling 35
6. Conclusions 52
Initiation of Motion Findings on Hard Substrates 52
Unified Scaling 53
Literature Cited 54
Appendix A: Experimental Facilitates 59
Appendix B: Additional Details for Angle of Attack Experiments 66
Appendix C: Table of Experimental Results 67
Appendix D: The Acceleration/inertia Correction Factor, f_I 91
Appendix E: Enhanced Flow Measurements 93
Appendix F: Numerical Modeling 101
Appendix G: Python Script in a Jupyter Notebook for Initiation of Munition Motion on Hard Substrates 109

List of Tables

Table 1: Geometry properties of surrogate munitions. The identifier of the munitions corresponds to the labels in Figure 4. Note that the diameter is taken as the maximum diameter of the tested object. First column: the number of experiment; second column: the surrogate type; third column (D): the nominal diameter of the tested object; fourth column (L): the length of the tested object; fifth column: the volume of the tested object; sixth column: the mass of the tested object; seventh column: the density of the tested object. 20

Table 2: An overview of the initiation of motion experiments conducted on a fixed bed. 24

Table 3: Flow and munition variables. 37

Table 4: Unidirectional flow experimental initiation of motion matrix illustrating the various trials for each experimental condition..... 66

Table 5: Unidirectional Experimental Data. First column (#): the number of experiment, second column: the flume used for the experiment, third column: the nominal diameter of the examined munition or object, fourth column: the angle of attack, fifth column: the slope of the flume, sixth column: the projected area of the munition of object, seventh column (ρ_m): the munition density, eighth column (ν): the kinematic viscosity of water, ninth column (ρ_w); the water density, tenth column (H_c): the characteristic depth of the flow (water depth for open channel flows and half the channel height for channel flows), eleventh column (U): critical velocity for initiation of motion, twelfth column (T): the period of the flow for the case of oscillatory flows. 68

Table 6: Oscillatory Experimental Data. First column (#): the number of experiment, second column: the flume used for the experiment, third column: the nominal diameter of the examined munition or object, fourth column: the angle of attack, fifth column: the slope of the flume, sixth column: the projected area of the munition of object, seventh column (ρ_m): the munition density, eighth column (ν): the kinematic viscosity of water, ninth column (ρ_w); the water density, tenth column (H_c): the characteristic depth of the flow (water depth for open channel flows and half the channel height for channel flows), eleventh column (U): critical velocity for initiation of motion, twelfth column (T): the period of the flow for the case of oscillatory flows. 89

Table 7: The conditions of the experiments in IHFF..... 93

Table 8: The conditions of the experiments in the Small Oscillatory Tunnel 94

Table 9: Constants used for the RNG k-ε 104

List of Figures

Figure 1: Schematic of selective grain entrainment (Komar 1996) 13

Figure 2: Schematic of a pivoting particle of size D lying on a rough bed with roughness elements of size "k". Two forces are present at the instant of imminent motion, shear driven drag (F_d) and immerse weight (W_i). A moment balance around the contact point "p" 16

Figure 3: Contact angles of ellipsoidal gravel particles and the corresponding motion types, where D_b and K_b are the intermediate axial diameters of pivoting particle and bed particles, respectively, and Φ denotes the contact angle. (from Li and Komar, 1986) 17

Figure 4: The surrogates (blue) and canonical-shape (yellow) objects tested in the initiation of motion experiments..... 19

Figure 5: Overview of initiation of motion facilities (refer to Appendix A for additional facility details)..... 23

Figure 6: Zoom in on the apparatus in the WHOI flume: an aluminum beam spanning the flume supported a point gauge and line laser. A video camera was mounted above to record trials. Munition offset was calculated as the angular distance of the rotational axis of symmetry from the stream-wise direction, In the case of 0 degree the munition projectile was pointed upstream. 25

Figure 7: Schematic of initial motion behavior for cartridges (top image) and warheads (bottom image). Cartridges rolled on two weight-bearing points in a conical motion. Warheads rolled linearly on a cylindrical weight bearing surface (weight-bearing contacts indicated by orange points or lines)..... 27

Figure 8: Initiation of motion for munitions and warheads on a horizontal PVC bottom. Note the * denotes that the NRL surrogate used. 28

Figure 9: Overview of observed transport behaviors over PVC patch in STF (observations 1, 2, and 3 are listed from top to bottom)..... 29

Figure 10: Effect of angle of attack on the streamwise drag forces from accompanying CFD modeling 30

Figure 11: Effect of steel bed slope on cartridge offset trials. Two flume slopes are a mild slope of 0.4° and horizontal slope (Horz.) (slope of 0.04°, taken as horizontal). 31

Figure 12: (top) Effect of horizontal bottom rough on cartridge initiation of motion. WHOI flume was used for PVC bottom and STF was used for the steel bed. (bottom) same plot excluding 0 degree angle of attack data..... 32

Figure 13: Comparison of the current initiation of motion experiments (from Figure 8, Figure 11, and Figure 12) to data compiled by Friedrichs (2013). Light gray symbols (bottom right of legend) are data compiled from Friedrichs (2013), references to each data set are included. All remaining symbols (black, dark gray, yellow, green, red, and blue) are from current experiments.

Each legend entry for current experiments denotes munition type and substrate type. All flows are unidirectional unless denoted with "oscillatory" in the legend entry for oscillatory flows conditions. All experimental data listed in Appendix C is included in this figure. 33

Figure 14: The Shields parameter plotted against the ratio of the particle size to bed roughness size and compared with the results obtained by James (1990). The dashed line with a minus one slope is superimposed for comparison. 34

Figure 15: The threshold for initiation of motion at different flow periods shows that the impact of acceleration reduces at about T = 6 sec 35

Figure 16: Isbash analysis plot (R^2=0.056) 39

Figure 17: a) Schematic of flow around munition, b) flow around a plate (right-top), and c) flow around a cylinder 40

Figure 18: Isbash analysis plot (Φ_{Isbash} vs D_{Isbash}/l) (R^2=0.228) 41

Figure 19: Isbash analysis plot (Φ_{Isbash} vs l/s) (total R^2=0.364) 42

Figure 20: Modified Isbash analysis plot (Φ_{Isbash} vs l/s) (R^2=0.929) 43

Figure 21: Experimental observation using Rennie et al. (2017) scaling (R^2=0.242) 46

Figure 22: Experimental observation of critical flow velocity for the initiation of motion of different munitions (total R^2=0.268) 47

Figure 23: Modified mobility parameter Φ_2 which includes acceleration effects (f_I) versus l/s (R^2=0.933) 48

Figure 24: Modified mobility parameter Φ_2 versus l/s with additional oscillatory data from Williams (2001). 49

Figure 25: Modified mobility parameter Φ_3 which neglects acceleration effects (f_I = 1) versus l/s (R^2=0.929) 50

Figure 26: Modified mobility parameter Φ_2 versus D/k_s (R^2=0.776) 51

Figure 27: WHOI flume used for unidirectional flow initiation of motion experiments. 59

Figure 28: The Small Tilting Flume (STF) was used to continue unidirectional flow initiation of motion experiments from the WHOI. 60

Figure 29: Overview of aluminum frame spanning the width of the Small Tilting Flume (STF) with attached point gauge and line laser. Experiments located 5 m from the upstream of the flume. 61

Figure 30: The STF bed is made of rough (pitted), painted steel. 61

Figure 31: The Cavitation Tunnel used for unidirectional high flow rates to test the threshold for initiation of motion of munitions at small angle of attack. 62

Figure 32: Sketch of the Illinois Hyporheic Flow Facility 63

Figure 33: Large Oscillatory Sediment Water Tunnel (LOWST) used for initiation of motion experiments in oscillatory flows. 64

Figure 34: Sketch of the Small Oscillatory Tunnel, side view. 65

Figure 35: Inertia/acceleration correction factor f_I..... 92

Figure 36: The top view of the locations on the munition where the slices of PIV measurements were taken. “Slice a” is the closest to the camera. 95

Figure 37: The contours of the mean streamwise velocity field around the munition across the centerline under five different free stream flow velocities (shown in Table 7). Flow is from left to right. 97

Figure 38: The vorticity around the munition across the centerline under different free stream velocities (shown in Table 7). The positive vorticity is counterclockwise. 98

Figure 39: The contour of the streamwise mean velocity at each phase in a cycle. In this test, the period of the piston is 3 sec and the half stroke is 0.04 m 99

Figure 40: Synchronized PIV and IMU data support phase lead of initiation of motion. The red dot denotes the time when the initiation of motion occurred..... 100

Figure 41: Computational Domain for a) Oscillatory and b) unidirectional flow experiments.. 102

Figure 42: Comparison between PIV measurements and CFD results for the case of unidirectional flow. 106

Figure 43: CFD results for the case of unidirectional flow: a) complex flow pattern and relative pressure field distribution on the munition surface b) velocity vectors for a slice close to the center of mass of the 20 mm munition c) velocity vectors for a slice close to the tip of the 20 mm munition 107

Figure 44: Comparison between PIV measurements and CFD results for the case of oscillatory flow. 108

List of Acronyms

CAD	Computer Aided Design
CFD	Computational Fluid Dynamics
GUI	Graphical User Interface
IHFF	Illinois Hyporheic Flow Facility
LOWST	Large Oscillatory Water-Sediment Tunnel (LOWST)
MP	Megapixels
NRL-Stennis	Naval Research Laboratory; Stennis Space Center, Mississippi
PIV	Particle Image Velocimetry
PVC	Polyvinyl Chloride
RANS	Reynolds Averaged Navier Stokes
RNG k-ε	Re-Normalization Group (RNG) k - ε
SERDP	Strategic Environmental Research and Development Program
SOT	Small Oscillatory Flume
STF	Small Tilting Flume
UIUC	University of Illinois at Urbana-Champaign
UMES	Underwater Munitions Expert System
UXO	Unexploded Ordnance
VTCHL	Ven Te Chow Hydrosystems Lab
WHOI	Woods Hole Oceanographic Institution Flume (named after the original location from which the Hydrosystems Lab procured the flume)

Keywords

Initiation of Motion of Munitions, Motion Tracking, Munition Migration, Oscillatory Flow, Particle Image Velocimetry, Physical Laboratory Experiments, Unidirectional Flow

Acknowledgements

We would like to express gratitude to the research team for their dedication and continuous energy in helping to move the project forward, which includes the follows researchers:

Carlo Zuniga Zamalloa, PhD (postdoctoral researcher)
Heng Wu (PhD student)
Dimitrios K. Fytanidis (PhD student)
Sarah Wenzel (hourly undergraduate student)
Stephen Gates (hourly undergraduate student)
Andrew Waratuke, MS (research engineer)
Alejandro Vitale, PhD (visiting researcher from Argentina)
Nils Oberg, BS (research programmer)
W. David Null (hourly undergraduate student)
Hannah Morch (hourly undergraduate student)
Nicholas Moller (MS student)

Also, we you like to thank the Dr. Joe Calantoni at NRL-Stennis for providing surrogate munitions for our CEE Machine Shop to duplicate for laboratory testing.

1. Abstract

Our research project responds directly to MRSON-14-01 with an emphasis on the need to improve our understanding of the phenomenology of entrainment, transport and fate of underwater munitions. A recent white paper (SERDP 2010, p.4) identified several knowledge gaps in the predictive skill of munitions mobility models. Our research effort aligns to address these gaps in environments with hard bottom substrates. Ultimately, the fundamental work herein provides a critical data set and initiation of motion predictors to improve existing field scale models for munitions mobility (i.e., Underwater Munitions Expert System, UnMES; Rennie and Brandt, 2015) that are difficult or practically impossible to obtain with existing field measurements.

Work presented herein provides physical laboratory results for initiation of motion and transport of various surrogate munitions over various hard substrates having different roughness (smooth PVC, pitted steel, 1.4 cm marbles, 3.5 cm gravel, and 3.81cm spheres) in unidirectional flow and oscillatory flows. In addition, based on flows resulting in initiation of motion, particle image velocimetry (PIV) measurements were conducted in both unidirectional and oscillatory flows to resolve the flow structure and estimate drag forces to ultimately help develop relationships to predict initiation and transport of munitions.

2. Objective

We seek to quantify the incipient motion, transport and fate of underwater munitions in coastal environments comprised of mobile beds and/or hard bottoms (e.g., sandy and gravel/rock) under a range of relevant hydrodynamic conditions (e.g., waves, currents). The existing underwater phenomenology of munitions expects mobility to be maximized when munitions are proud (i.e., unburied). It has been suggested that the degree of mobility may be orders of magnitude larger when munitions are transported over a hard gravel-like substrate where there is little or no sediment cover (e.g., such as on coral reefs) versus a sandy or muddy bottom. However, there is a dearth of direct observations made under a wide range of controlled hydrodynamics conditions representative of waves and currents. Through an extensive set of detailed large-scale laboratory experiments we develop a more complete picture of the phenomena involved in the entrainment, transport, and fate of underwater munitions, especially on hard substrates of various roughnesses. The laboratory experiments allowed for detailed measurements over a controlled range of conditions (e.g., hydrodynamic forcing, turbulence characteristics, bed composition, and properties of munitions) which are not practically possible to achieve in field experiments and cannot be completely simulated with numerical models due to the high Reynolds number and wide-range of bottom roughness observed under field conditions. Leveraging our prior experience with scour and burial of mines, the results of the physical munition experiments presented herein provides critical data as well as newly developed initiation of motion predictors to improve existing field scale models for munitions mobility and eventually integration into the Underwater Munitions Expert System (UnMES), (Rennie and Brandt, 2015).

3. Background

Abandoned underwater munitions are a source of danger to humans and the environment alike. In addition to their ability to explode, unexploded ordnance (UXO) are subject to corrosive degradation that allows hazardous materials to leach into the surrounding environment (Edwards et al., 2016). These risk factors combined with the potential for munitions to migrate to more sensitive, human frequented, locations have given rise to laws mandating the remediation of unexploded ordnance in many areas classified under the Formerly Used Defense Sites program (SERDP, 2010). There have been over 400 sites identified as potentially containing abandoned, submerged munitions, encompassing more than 10 million acres of aquatic environment (SERDP, 2010). Cost estimates for the complete remediation of a select three of these sites have been issued as high as $2.7B (Jenkins et al., 2012). As such, a method of risk assessment for triage has been identified as a research priority. In response to this issue, the Strategic Environmental Research and Development Program (SERDP) has joined the remediation effort through the development of a probabilistic expert system to assess the likelihood of munition burial and migration. This system termed the Underwater Munitions Expert System (UnMES; Rennie and Brandt, 2015) will combine site data with specialized models to aid in assessing the various risks posed at each site, enabling higher confidence in triage efforts.

One of the primary concerns of SERDP to be modeled by the UnMES is the mobility of munitions under a variety of conditions found in coastal zones. To aid in informing this aspect of the expert system, recent munition-specific mobility models have been proposed based on sediment transport mechanics (Rennie et al., 2017; Jenkins et al., 2012) Additionally, several teams have conducted field work on in-situ munitions found in characteristic environments (Calantoni, 2014; Traykovski and Austin, 2017). The recent advances expand our understanding of UXO migration from larger sea mines (Wilkens and Richardson, 2007; Traykovski et al., 2007) to the sizes and densities commonly found in abandoned munition sites. However, all existing studies have ignored the effect of object shape and orientation as a mobility parameter. The present study seeks to establish an experimentally verified model that considers the effect of munition shape and orientation on mobility.

The dynamics of the interaction between objects and the seafloor in waves and currents are highly complex, but are relevant to an extensive range of phenomena, from scouring around objects, to their burial dynamics and initiation of motion/transport of objects when they are placed above hard substrates. Numerous studies have been conducted over years to enhance the general understanding of the underlying dynamics focusing mainly on the scour and burial dynamics. In the past, a large amount of both experimental and numerical work has been done regarding the study of scour phenomenon around an object positioned on the seafloor and the dynamics and flow structure around it (Voropayev et al., 1998; Bennett, 2000; Richardson and Traykovski, 2002; Cataño-Lopera and García, 2007; Cataño-Lopera et al., 2013; Cataño-Lopera et al., 2017). The prior studies enhanced the general understanding of the underlying dynamics of scouring around objects and the complex object-seabed-flow interaction. Relevant are also the previous studies on combined flows, in the laboratory and in the field, which have also shown that both the ultimate scour depth and the time scale of the self-burial process of short cylinders

are primarily functions of the Keulegan-Carpenter number, KC[1], and the Shields parameter, ψ[2], (Bayram and Larson, 2000; Sumer and Fredsøe, 2001). The same parameters also affect the scour around vertical piles in the field subject to combined waves and currents (Sumer and Fredsøe, 2001).

Furthermore, the study of mine burial resulted in significant advances in understanding the burial dynamics under waves, currents and combined flows (Voropayev et al. 1999; Voropayev et al 2003; Cataño-Lopera and García 2006; Wilkens and Richardson, 2007; Demir and García, 2007, Friedrichs et al., 2016). The prior works highlight the dynamic mechanisms of the burial of mines and objects of various shapes (e.g., cylindrical and manta) and properties (e.g., densities etc). Voropayev et al. (1999) studied the dynamics of disk-shaped objects (i.e., cobbles) placed on a sandy bottom under an oscillatory flow and showed that the burial depth of the cobble does not depend on the cobble density (for the hydrodynamic conditions tested). Similar results were obtained for the case of a cylinder horizontally placed over a sandy bed (Sumer and Fredsøe, 2001). More Recently, Voropayev et al. (2003) have investigated the burial of finite-length cylinders over a sandy floor with a sloped bottom under shoaling waves. Such studies showed that the final burial depth depends on both the KC number and the Shields parameter while the length of the scour hole depends mostly on the KC number. Additionally, Voropayev et al. (2003) showed that the cylinder might undergo periodic burial depending on the ratio of cylinder diameter to the height of migrating ripples. Similar observations were reported later by Cataño-Lopera and García (2006) for the case of a horizontal bottom under combined waves and currents. Subsequent work (Cataño-Lopera and García, 2007) showed the importance of the cylinder's angle of attack, which expanded on the scour geometries discussed in Voropayev et al. (2003).

While the above studies have enhanced our current knowledge for the interaction between objects-seabed-flow, there are still significant knowledge gaps regarding the behavior and the fate of objects positioned on a hard substrate (as is often encountered in numerous littoral zones across the globe, especially around coral reefs), especially, the mechanics of the initiation of motion of objects of different shapes and densities. These mechanics are extremely important, especially for the development of predicting models for the simulation of the mobility, transport and fate of munitions. Although various numerical models have been developed, e.g., the popular Vortex Lattice model (Jenkins et al., 2007), all models are lacking key parameter values, which ultimately affects the accuracy and reliability of the model results. While some work has been done recently for the case of initiation of motion of cylinders (Rennie et al., 2017), the effects of the shape of the examined objects (e.g., bluff versus streamlined/hydrodynamic bodies), the effect of the orientation of objects with respect to the mean flow direction (i.e., angle of attack), and the effect of bed roughness on the critical flow conditions for the initiation of motion of these objects remain unknown. The present work is an extensive large-scale experimental investigation of the critical parameters for the initiation of motion and the study the effects of

[1] $KC = U_m T/D$, where U_m is the maximum value of the undisturbed orbital velocity at the bed, T is the wave period, and D is the cylinder diameter

[2] $\psi = \frac{\tau_w}{gD(\rho_s - \rho)}$, where τ_w is the bed shear stress, ρ_s is the density of the sediment particle, ρ is the density of the water, g is the acceleration of gravity, and D is the cylinder diameter

angle of attack, shape, density, roughness and flow characteristics on the initiation of motion of munitions.

Of relevant interest is the previous work conducted in the field of sediment transport for the initiation of motion of grains of different diameters, shapes, and densities. Throughout the literature, several approaches have been adopted for the definition of threshold conditions for the initiation of motion of single sediment grains. These approaches can be categorized as follows: i) empirical/semi-empirical formulas or ii) process-based, single-grain pivoting or sliding models for the initiation of motion of single exposed particles. An extensive review of the above models of sediment entrainment can be found in Garcia (2008) and Komar (1996).

Various empirical formulas are available in the literature dealing with the evaluation of sediment particles threshold of motion. While these formulas (e.g., Shields 1936; Niell 1967 and 1968; Niell and Yalin 1969; Yalin 1972; Yalin and Karahan 1979) are mainly based on laboratory flume experiments, uniform sediment diameter distributions, and well-flatted sediment beds to eliminate preferential exposure of individual grains. More recent advances in the field deal with natural sediments of various size and densities and indicate that variations in grain diameter and densities play an important role on the selective entrainment of grains in mixed sediments (Komar 1996).

In Figure 1, a schematic of the selective particle/object entrainment stress as a function of grain diameter is presented. In sands which carry minerals of different densities, there may be selective entrainment and sorting of the different density (and size) grains. An inverse relationship between density and particle diameter is observed for the minerals that are typically carried with sand (Li and Komar 1992; Komar and Wang 1984). Heavy minerals (e.g., zircon, garnet, ilmenite) tend to be presented as small diameter grains while light minerals (e.g., quartz and feldspars) have larger diameters and can be easier picked up by the flow. For large diameter sediments (e.g., gravels), higher diameter particles require higher flow velocities to be entrained which is an opposite trend from smaller diameter sands.

Models have been developed for the prediction of initiation of motion of exposed particles using analytical relationships. We can separate initiation of motion models in to two categories: i) models based on the work of Iwagaki (1956), Coleman (1967) and Ikeda (1982) for which the flow drag is compared with the Coulomb resistance to estimate the critical flow conditions for the initiation of motion particles of the same diameter, and ii) models based on pivoting models (Rubey 1938; White 1940; Komar and Li 1988) for which the pivot angle of the particle is taken into consideration for the case of a particle of different diameter pivoting over a bed consisting of grains of different diameter. The initiation of motion models can become the basis for the development of a predictive model for the initiation of motion of munitions.

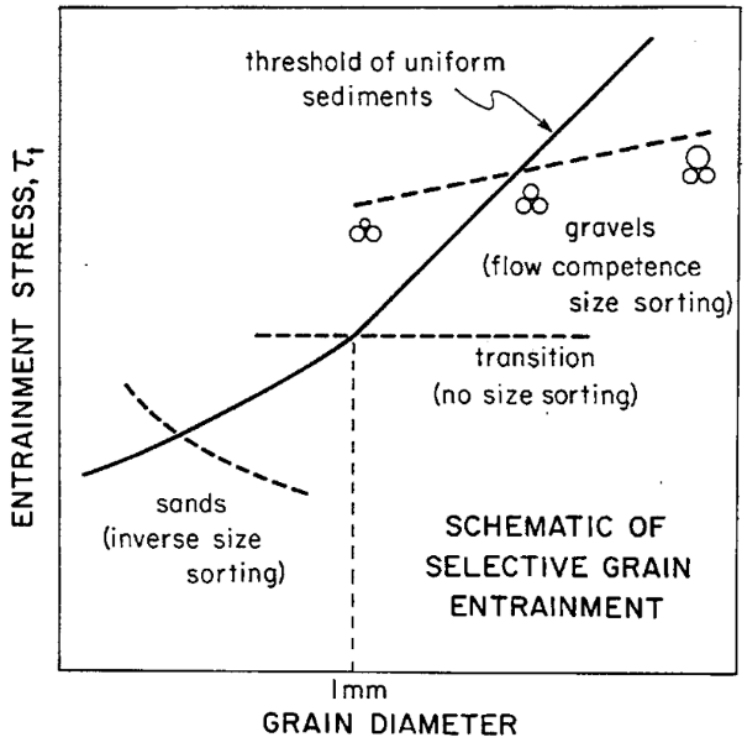

Figure 1: Schematic of selective grain entrainment (Komar 1996)

Analyses by Miller and Byrne (1966) and Li and Komar (1986) have shown a relationship between pivot angles and the ratio between the diameter of the pivoting grain and the diameter of the underlying bed grains over which pivoting take place, $\Phi = \alpha\left(D_{pivoting\ \ particle}/D_{bed}\right)^{\beta}$. The diameter of the bed grains is a measure of bed roughness. In addition, the diameter of the bed grains is typically used to estimate the roughness height; usually multiplied by a factor of α_s which can vary between 1 and 6.6 depending on the characteristic diameter that is chosen for the estimation of roughness height (e.g., D_{50}, D_{65}). Miller and Byrne (1966) and Li and Komar (1986) reported values of α and β for various shape particles (spheres, ellipsoidal, angular particles etc.). The values of β range from -0.2 to -0.4. The relationship between Φ and the ratio of the size of the pivoting grain (D) to the size of the bed element (*k*), D/k, obtained from experiments can be seen in Figure 3, showing the inversely proportional relationship of them when plotting on a semi-log axis as well as the corresponding motion types (sliding or rolling). Li and Komar (1986) further indicate that the motion type depends on the ratio of the smallest axial diameter to the intermediate diameter of the ellipsoidal grain particle.

The mechanical analysis of particle/munitions entrainment into motion involves balancing the moments of the forces acting on the particle (Garcia, 2008). First movement occurs when the fluid forces overcome the object's immersed weight, pivoting the object over the underlying particles through the pivot angle so that the object rotates out of its resting position (James, 1990). This requires a derivation of the threshold condition in terms of the flow velocities or

stresses acting at the particle/object level (Nino et al., 2003). The particle-level velocities can be converted into mean flow velocities and stresses (Garcia, 2008). Fenton and Abbott (1977) conducted a set of pivoting experiments in which they highlighted the importance of the protrusion/hiding of the exposed particle by the neighboring bed particles. Later, James (1990) conducted pivoting experiments for the case of spheres and presented an analytical model for the estimation of critical flow conditions in the form of a Shields-like diagram. He also presented a detailed analysis and review of the important parameters of pivoting analysis. Similar experiments were conducted by Carling et al. (1992) who in addition to spheres studied rods, ellipsoids, discs and cuboids, illustrating that the shape of the grain is an important parameter for the definition of the initiation of motion of the particles. The prior finding is important in the current work for the analysis of initiation of motion of munition positioned in different angles with respect to the mean flow.

In the present study, a subset of experiments was conducted to assess the effects that the flow and bottom roughness have on the initiation of motion of canonical shape objects such as spheres and cylinders. The mechanical analysis of particle/munitions entrainment into motion involves balancing of moments of the forces acting on the particle (Garcia, 2008). The analysis of these experiments on ideal objects is performed following the work of Komar and Li (1988).

Komar and Li (1988) proposed a pivoting model considering the force balance (Figure 2), including the lift, drag, and the immersed weight of the grain, of a sediment particle on a bed. From their model, the critical flow velocity at the particle level that can pivot the sediment particle can be expressed as

$$\overline{u_p} = \Omega \left[\frac{4}{3} \frac{\rho_s - \rho}{\rho} g D_b \frac{\tan \Phi}{\mathrm{A} + \mathrm{B}(D_b / D_c) \tan \Phi} \right]^{0.5}, \qquad \text{Equation 1}$$

where $\mathrm{A} = C_d \xi k_d^2$, $B = C_L k_L^2$, ρ_s is the density of the sediment particle, ρ is the density of the water, g is the acceleration of gravity, D_b and D_c is the intermediate and smallest diameter of the sediment particles (assume ellipsoidal grain), C_d is the drag coefficient, C_L is the lift coefficient, $k_d = u_d / \overline{u_p}$ and $k_L = u_L / \overline{u_p}$ is the ratio of the flow velocity at the level of the effective drag and lift force to the flow velocity at the particle level, ξ is a factor introduced to account for sheltering of the particle being entrained by neighboring particles (hiding factor), Φ is the geometric pivoting angle, and Ω is a factor that accounts for the turbulence in the flow, which is defined as the mean flow velocity at the particle level divided by the maximum instantaneous flow velocity that actually pivot the sediment grain.

From the flow velocity at the level of the center of mass of the observed sediment particle (Equation 1) and using the law of the wall (Garcia, 2008), the bed shear stress required to entrain the particle can be written as

$$\tau_p = (\rho_s - \rho) g D_b \frac{4\Omega^2 / 3}{[5.75 \log(30 z_p / \alpha \overline{D_b})]^2} \left[\frac{\tan \Phi}{A + B(D_b / D_c) \tan \Phi} \right], \qquad \text{Equation 2}$$

where $\overline{D_B}$ is the median diameter of the bed material, α is a roughness coefficient (factor that is applied on the median diameter of the bed to convert the median diameter of the bed into the roughness), z_p is the protrusion of the observed sediment particle from the bed into the flow.

The shear stress can be non-dimensionalized using the immersed weight of the sediment particle

$$\psi = \frac{\tau_p}{(\rho_s - \rho) g D_b} = \frac{4\Omega^2 / 3}{[5.75 \log(30 z_p / \alpha \overline{D_b})]^2} \left[\frac{\tan \Phi}{A + B(D_b / D_c) \tan \Phi} \right]. \qquad \text{Equation 3}$$

For the purpose of preliminary examination of the model for munition mobility, we simplify the model proposed by Komar and Li (1988) by taking in consideration just two forces: shear driven drag and immersed weight while neglecting the lift force. The drag force scales as

$$F_d \sim \tau_w D^2, \qquad \text{Equation 4}$$

where τ_w is the bed shear stress. The gravitational force, F_g, arises from the immersed weight, is given by

$$F_g = W_i - F_b \sim gD^3(\rho_s - \rho), \qquad \text{Equation 5}$$

where W_i is the weight of the object, F_b is the buoyancy acting on the object, g is the acceleration of gravity, and ρ_s and ρ are the density of the object and the fluid, respectively. Considering the respective moment arms for each force, the balance of moments is given by

$$F_d D \cos\varphi = (W_i - F_b) D \sin\varphi, \qquad \text{Equation 6}$$

where φ is the contact angle between the object and the neighboring bed particles. By substituting Equation 4 and Equation 5 into Equation 6, the Shields parameter, ψ, can be determined as

$$\psi = \frac{\tau_w}{gD(\rho_s - \rho)} \sim \tan\varphi. \qquad \text{Equation 7}$$

For the present study, a direct geometric interpretation for the angle, φ, can be expressed as

$$\tan\varphi = \frac{k/D}{\sqrt{1 + 2k/D}}. \qquad \text{Equation 8}$$

When the ratio k/D is small, the above expression can be approximated as $\tan\varphi \sim k/D$. For small k/D, the Shields parameter scales as k/D, which corresponds to the power law for the ideal system of spherical particles (James 1990). The Shields mobility parameter obtained is inversely proportional to the size ratio of the pivoting particle and the rough bed.

Detailed PIV experiments (Wu et al., 2017) allowed estimates of the wall shear velocities in imminent motion of spheres and cylinders and estimate the shear velocity by approximating it to the maximum value of Reynolds stress. The tests for canonical geometries allow us to ascertain that our approximation of shear velocities for highly rough walls is appropriate.

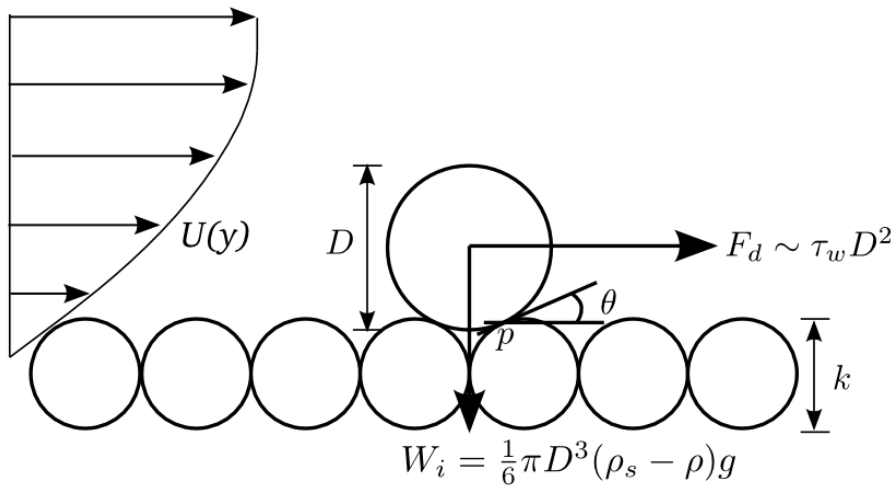

Figure 2: Schematic of a pivoting particle of size D lying on a rough bed with roughness elements of size "k". Two forces are present at the instant of imminent motion, shear driven drag (F_d) and immerse weight (W_i). A moment balance around the contact point "p"

In further examinations of selective entrainment due to differences in particles sizes and densities, it is necessary to focus on the fluid forces acting directly on the individual particles (Komar and Li, 1988; Wiberg and Smith, 1987). A derivation is required of the threshold condition in terms of the flow velocities and stresses acting at the object level (Nino et al., 2003). The particle-level velocities can be converted into mean flow velocities and stresses (Garcia, 2008).

The contact angle is also an important factor in the pivoting analysis and depends on the grain size, the shape and the orientation of the grains which is encapsulated in the proposed relationship

$$\theta = \alpha(D/k)^{-\beta}, \qquad \text{Equation 9}$$

where α and β are empirical coefficients (Li and Komar, 1986).

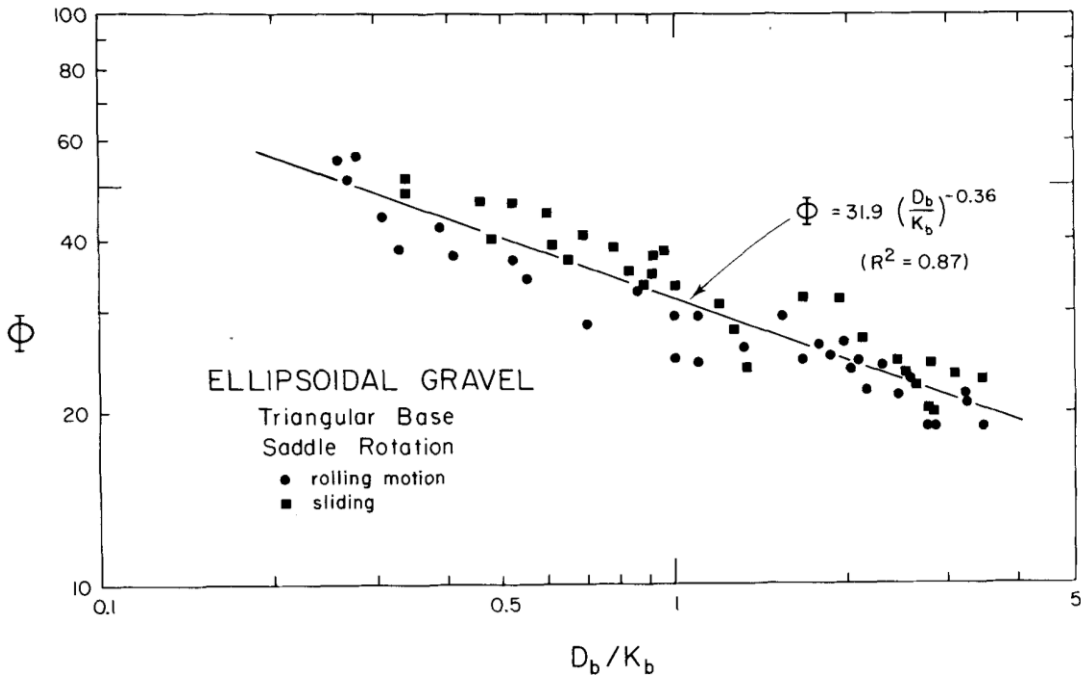

Figure 3: Contact angles of ellipsoidal gravel particles and the corresponding motion types, where D_b and K_b are the intermediate axial diameters of pivoting particle and bed particles, respectively, and Φ denotes the contact angle. (from Li and Komar, 1986)

Cokgor (2002) studied the behavior of the lift and drag coefficients around partially buried cylinders on a rigid bottom exposed to combined waves and currents for low Keulegan-Carpenter (*KC*) numbers ($KC = U_m T/D$, where U_m is the maximum value of the undisturbed orbital velocity at the bed, T is the wave period, and D is the cylinder diameter). For waves, the coefficients for lift and drag are affected by *KC* and Reynolds Number (Sarpkaya 2010; Sumer and Fredøse 2006). In the current study, these effects were incorporated in to the scaling through the inertia/acceleration coefficient as will be shown later (refer to Section 5.3 and Appendix D).

4. Technical Approach

In this study, we observe the incipient motion of surrogate munitions and canonical shapes (cylinders and spheres) through large-scale physical laboratory investigations. Numerous facilities in the Ven Te Chow Hydrosystems Laboratory (VTCHL) at the University of Illinois at Urbana-Champaign (UIUC) were used to examine munitions behavior under unidirectional and oscillatory flows. The following subsections provide details on range of experimental objects as well as experimental facilities.

4.1 Range of Surrogate Munitions Test Subjects

In total, 37 representative objects (7 surrogate munition shapes and 30 canonical objects) were used throughout this study. The seven surrogate munition shapes can be grouped into three surrogate munition types (duplicated from surrogates at NRL-Stennis): 81 mm mortar, 25 mm cartridge, and 20 mm cartridge as depicted in Figure 4. Each surrogate munition type could be separated into two separate pieces: the warhead and the shell casing (for 20 mm and 25 mm munitions) and the main body (or warhead) and the fin (or tail) section (for the 81mm mortar). The warhead (or Projectile) refers to only the stainless steel tip of the munition, detached from the main body, where the casing refers to the black Delrin plastic body of the munition. Herein we will use cartridge (or Round) to refer to the entire munition. For the 81 mm mortar, the tail section refers to the aluminum shaft with attached fins, and the body refers to the remaining black and metallic projectile (composed of stainless steel and Delrin plastic). The word “finless” is also used to identify the 81 mm mortar body alone (i.e., without the tail). Refer to Figure 4 for an overview of the seven surrogate configurations that were tested. (In addition, a modified 81 mm mortar body in a cylindrical shape was created to house an inertial measurement sensor, refer to item G in Figure 4 and Figure 40).

In addition to the surrogate munitions, canonical shapes (i.e., spheres and cylinders) were tested for the threshold for incipient motion on a rough bed. The canonical shapes were constructed of two different materials: acrylic PMMA and acetal with densities 1.19 g/cm^3 and 1.40 g/cm^3, respectively. For each material, there are five different spherical diameters, resulting in a total of ten spheres being tested. Besides the ten spheres, twenty cylinders having the same diameter and material of the spheres were tested. The cylinders of the same two materials and the five diameters as used for the spheres. The 20 cylinders are grouped into two sets. The first set comprised of 10 cylinders having sharing the same length with five different diameters for each of the two materials. The second cylinder set consisted of 10 cylinders having five different lengths for each of the five different diameters and two materials to maintain a constant length to diameter ratio.

Figure 4: The surrogates (blue) and canonical-shape (yellow) objects tested in the initiation of motion experiments.

Table 1: Geometry properties of surrogate munitions. The identifier of the munitions corresponds to the labels in Figure 4. Note that the diameter is taken as the maximum diameter of the tested object. First column: the number of experiment; second column: the surrogate type; third column (D): the nominal diameter of the tested object; fourth column (L): the length of the tested object; fifth column: the volume of the tested object; sixth column: the mass of the tested object; seventh column: the density of the tested object.

Label [Fig. 4]	Nominal Size and Type	Diameter, D [mm]	Length, L [mm]	Volume [$\times 10^{-4} m^3$]	Mass, m [kg]	Density, ρ_m [kg/m^3]
A	20 mm projectile	19.9	61.1	0.15	0.106	8219
B	20 mm shell	29.4	168.2	0.79	0.185	2342
C	25 mm projectile	24.8	78.7	0.21	0.18	7846
D	25 mm shell	37.8	218.8	1.69	0.346	2106
E	81 mm finless	81	357.6	11.98	3.765	3362
F	81 mm mortar	81	514.6	12.10	3.901	3225
G	IMU cylinder	81.5	164	8.566	1.100	1284
H1	19 mm cylinder	19	57	0.16	0.019 0.022	1190 1400
H2	25 mm cylinder	25	70	0.34	0.040 0.048	1190 1400
H3	38 mm cylinder	38	102	1.15	0.137 0.161	1190 1400
H4	51 mm cylinder	51	140	2.85	0.339 0.399	1190 1400
H5	63 mm cylinder	63	171	5.34	0.635 0.748	1190 1400
J1	19 mm cylinder	19	304	0.86	0.102 0.120	1190 1400
J2	25 mm cylinder	25	304	1.49	0.177 0.209	1190 1400

Table 1 continued…

Label [Fig. 4]	Nominal Size and Type	Diameter, D [mm]	Length, L [mm]	Volume [$\times 10^{-4} m^3$]	Mass, m [kg]	Density, ρ_m [kg/m^3]
J3	38 mm cylinder	38	304	3.44	0.409 0.482	1190 1400
J4	51 mm cylinder	51	304	9.48	1.128 1.327	1190 1400
J5	63 mm cylinder	63	304	6.19	0.737 0.867	1190 1400
K1	19 mm sphere	19	-	0.04	0.005 0.006	1190 1400
K2	25 mm sphere	25	-	0.08	0.010 0.011	1190 1400
K3	38 mm sphere	38	-	0.29	0.035 0.041	1190 1400
K4	51 mm sphere	51	-	0.69	0.082 0.010	1190 1400
K5	63 mm sphere	63	-	1.31	0.156 0.183	1190 1400

4.2 Initiation of Motion Experiments

In total, many initiation of motion experiments were conducted in five various flow facilities in the Ven Te Chow Hydrosystems Laboratory as seen in Figure 5 (refer to Appendix A for additional facility details). As indicated in Figure 5, each experimental facility aided in expanded the experimental test matrix (e.g., flow conditions, bed conditions, etc.).

For unidirectional flows, the primary facility was a 17-m recirculating unidirectional flume (WHOI flume). The WHOI flume raceway measures 17.3-m long, 0.6-m wide. The flow was driven by a centrifugal pump capable of a maximum discharge of 55 L/s associated with a maximum observed mean velocity of 0.76 m/s. The discharge from the headbox is lead through a ball pit and flow conditioner composed of array PVC pipes to reduce secondary circulation and surface waves (Further description available in Butman and Chapman (1989)). The bed had two configurations, smooth PVC bed (k = 0.0015 mm) as well as a one-layer cover of glass marbles (k = 14 mm). In the case of a marble bed, the glass marbles were tightly packed and placed on the PVC bed. The flow conditions in all the experiments were not strong enough to move the packed layer of marbles. Measuring instrumentation included an Ultra Magflow flow meter (accuracy 0.0009 m/s) the recirculation pipe, a vernier point-gauge (accuracy 0.0003 mm), and two video cameras used to monitor the experimental test section.

The experimental test section, where the munitions where placed at the beginning of each trial, is located approximately 10 meters downstream of the headbox, ensuring developed flow with minimized entrance-effects (Möller, 2014). Water surface elevations were measured in the center of the flume approximately 0.4 m downstream of the test section. Unidirectional experiments with imposed slope were performed in the 19-m tilting flume. The tilting flume is capable of driving a 90 L/s flow, with a maximum observed mean velocity of 0.73 m/s. The raceway, constructed of a painted, pitted steel bed and plexiglass windows, measures 19.5-m long, 0.9-m wide with an imposed entrance contraction down to 0.55 m. Two slopes of 0.06 and 0.6 were imposed during trials. The water surface elevation is controlled by a downstream gate. Sufficient depths were selected to avoid the proximity of a hydraulic jump with the test section. Water surface elevation were measured upstream of the munition using the aforementioned point-gauge.

An additional set of unidirectional experiments performed in a cavitation tunnel (CT) was used to test munition mobility with flow-rates unattainable in the preceding flumes. The CT is a unidirectional, contracting tunnel with a rectangular cuboid test section of tunnel measuring 1.2-m long, 0.305-m wide and deep. The bed was composed of smooth PVC. The flow is delivered by an impeller capable of driving a flow of 9 m/s when pressurized, which is routed through a series of vanes to reduce flow vorticity. Discharged measurements are obtained from a previously found inverter frequency-discharge relationship calibrated with the Laser Doppler Velocimetry. All experiments were performed when the tunnel was pressurized. The maximum observed mean velocity in the tunnel was 2.39 m/s.

Experiments requiring oscillatory flow conditions were performed in the Large Oscillating Water Sediment Tunnel (LOWST). The tunnel maintains a constant interior width of 0.8 m, a vertical depth of 0.6 m and a length of 12 m. Two bed types were tested, smooth PVC (k_s = 0.0015 mm) and gravel (k = 35 mm). In the case of gravel bed, gravels were placed on the PVC bottom and

the tested flow conditions were not strong enough to induce any motion of the gravels. The oscillatory flow is driven by three pistons. The maximum orbital velocity of experiments ranged from 0.05 - 0.61 m/s with a period range of 2 to 12 seconds. The flow is passed through flow straighteners located at both ends of the 12-m test section. The core velocity was estimated by calibration curve and confirmed with acoustic Doppler velocimetry. Select flow conditions were measured with particle image velocimetry. The LOWST also contains a close-loop pump designed for unidirectional and combined flows. This was used for additional unidirectional flow experiments over gravel.

Additional initiation of motion experiments (especially for canonical shapes) were conducted in the Illinois Hyporheic Flow Facility (IHFF), which is a recirculating open-channel water flume that houses a fixed packed bed. The fixed bed consists of uniform size plastic spheres that have a diameter of 0.0381 m and are arranged in a cubic packing configuration. The plastic spheres were rigidly fixed on stainless steel rods to prevent motion of the bed during experiments. The test region in the flume is 4.8 m long and has zero slope. The rectangular cross section in the test region is 0.35 m wide and 0.3 m high.

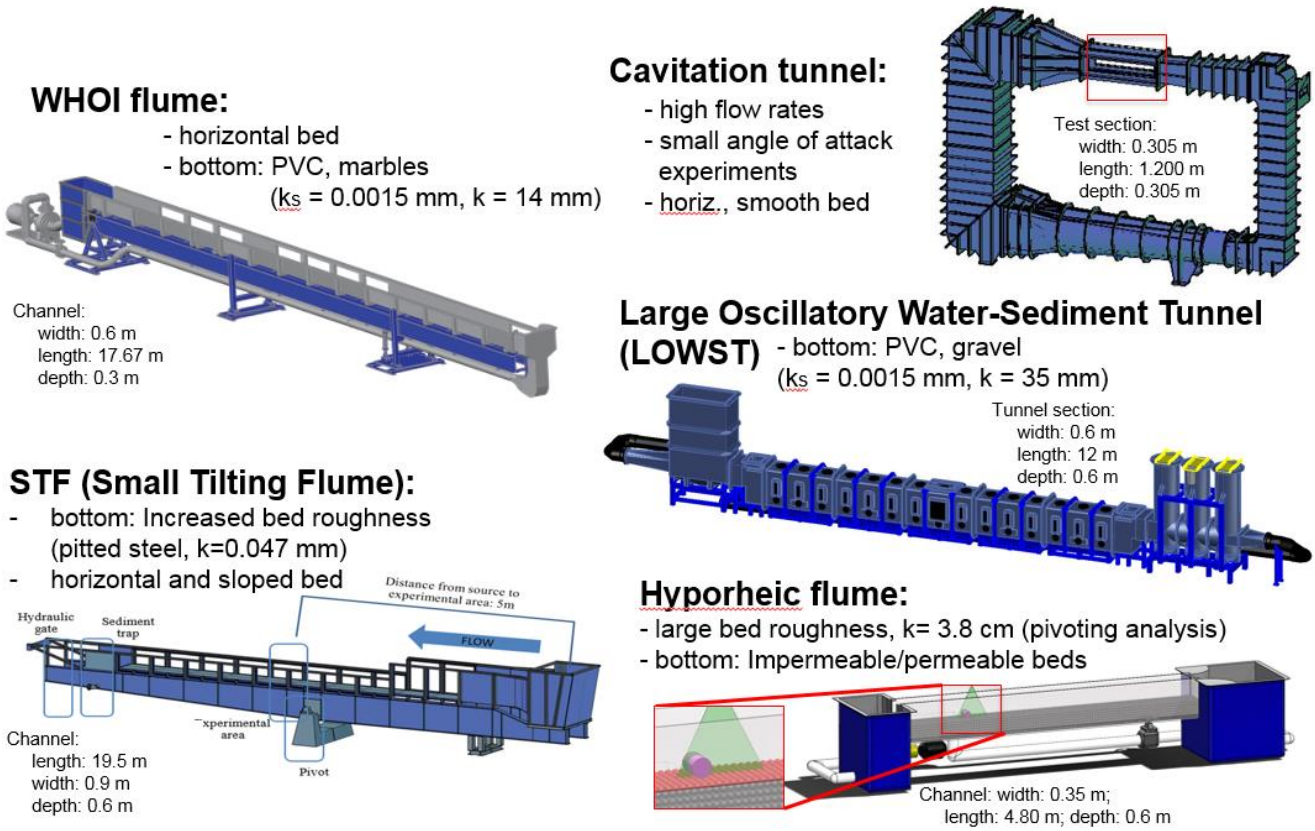

Figure 5: Overview of initiation of motion facilities (refer to Appendix A for additional facility details)

Below is an overview matrix of all initiation of motion experiments conducted across the various experimental facilities:

Table 2: An overview of the initiation of motion experiments conducted on a fixed bed.

Substrate	Facility	Projectile or Finless mortar			Projectile with cartridge [shell] or Mortar			IMU cylinder	Idealized	
		20 mm	25 mm	81 mm	20 mm	25 mm	81 mm	81.5 mm	Cylinder	Sphere
PVC	WHOI	17	20	14	20	37	34	-	-	-
	CT	2	2	3	1	-	-	-	-	-
steel	STF	21	24	26	-	-	-	-	-	-
marble (1.4 cm)	WHOI	20	-	-	5	-	-	-	-	-
gravel (3.5 cm)	LOWST	-	-	-	1	3	2	8	-	-
plastic spheres (3.81 cm)	IHFF	-	-	-	-	-	-	-	40	20

4.2.1 Procedure for Unidirectional Flow Experiments

Experiments were conducted on each munition at a range of angular offsets measured 0 degrees (projectile pointing upstream) to 180 degree (projectile pointing downstream). At the start of each trial, the munition was positioned in the facility at the angle under investigation (See schematic in Figure 6).

For unidirectional experiments, placement was done in the presence of a developed, low velocity flow to prevent premature onset of motion due to pressure waves perturbing the munition as the pump accelerated from rest. For each trial, the angled munition was subjected to progressively faster flow velocities until motion was observed. At each increment the flow in the test section was allowed to stabilize before the pump was accelerated for the next tested flow rate. The average acceleration increment was 0.5 L/s for flows below 10 L/s and 1 L/s for flows above.

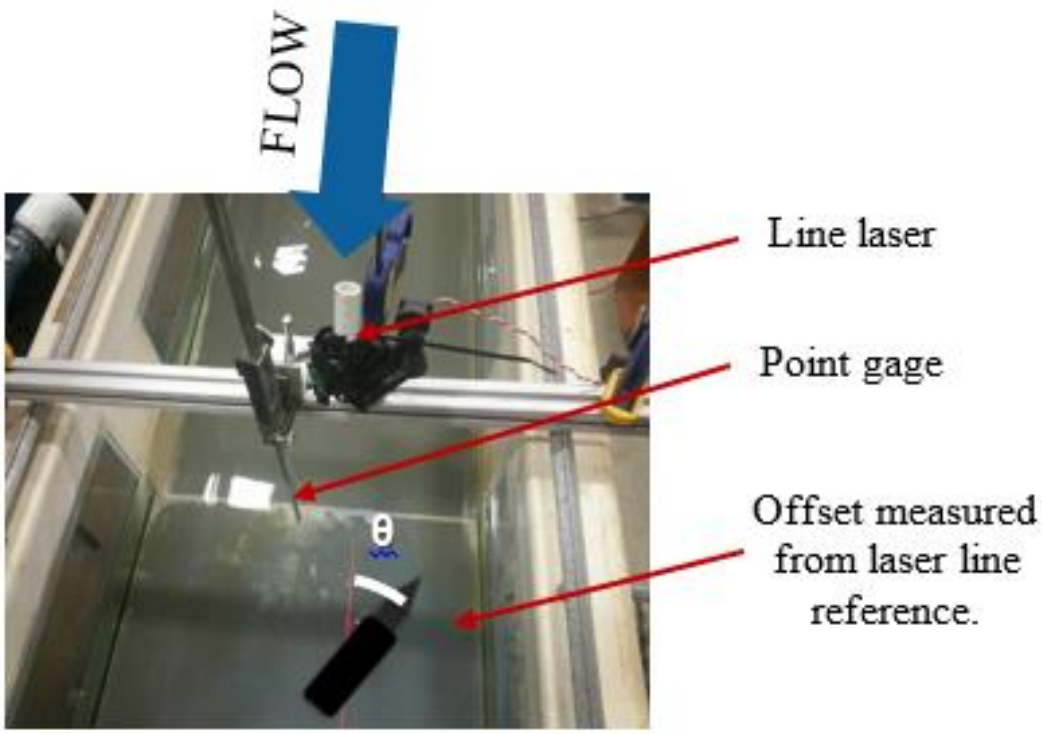

Figure 6: Zoom in on the apparatus in the WHOI flume: an aluminum beam spanning the flume supported a point gauge and line laser. A video camera was mounted above to record trials. Munition offset was calculated as the angular distance of the rotational axis of symmetry from the stream-wise direction, In the case of 0 degree the munition projectile was pointed upstream.

Note on Motion Criteria:

Due to the geometry of the munitions and the interest in the initiation of motion directly preceding transport phenomena, the onset of motion criteria was chosen to be any movement by the munition whose displacement exceeded half a munition length. This removed as candidates motion in the form of rocking in place, yaw-oscillations and short lateral oscillations. When motion occurred (Figure 7) during a period of equilibrium the nominal discharge and water surface elevation were recorded. When motion occurred in transition from one flow-rate increment to the next, the nominal discharge and water surface elevation were recorded at the onset of motion and averaged with those of the preceding increment.

Additional flow measurements were conducted to examine the pivoting model described above and to explore the impact of permeable versus impermeable beds (Wu et al., 2017) This data set is included in the analysis presented in the Results and Discussion section.

4.2.2 Procedure for Oscillatory Flow Experiments

Experiments under oscillatory flow conditions progressed both period and amplitude. A period was fixed and the amplitude increased in intervals of 0.01 m/s until motion was elicited or tunnel limitations were reached. For each interval the pistons were slowed, until the flow reached quiescence, then the following period-U max pair was tested. It takes approximately 15 seconds for the pistons to reach peak velocity when accelerated from rest.

Specifically, for the initiation of motion on a smooth PVC bottom, the effect of the wave period and munition orientation on the threshold near bottom maximum orbital velocities was tested for 20 mm cartridge and 81 mm mortar. A range of wave periods (2, 4, 6, 8, 10 sec) was covered. The munitions were tested in two different orientations: perpendicular or aligned with the flow direction. Four trials were conducted for the 20 mm cartridge aligned with the flow. Eleven trials were done for the 81 mm mortar placed perpendicular to the oscillatory flows covering a range of wave period from 2 to 12 seconds). Four trials were conducted for the 81 mm mortar aligned with the flow.

The threshold maximum orbital velocity was tested for the IMU cylinder for 10 second wave period on a gravel bed. In this trial, we achieved to synchronize the IMU embedded in the cylinder monitoring the motion of the cylinder with the Particle Image Velocimetry (PIV) with phase-locking.

5. Results and Discussion

5.1 Unidirectional Flows

Several different types of motion were observed in the initiation of motion experiments depending on the type of munition tested and its orientation to the flow, as depicted in Figure 7 and Figure 9. For cartridges at nonzero angle offsets, motion followed the path of a rolling cone. This is because the cartridge weight is distributed over two edges with different diameters: one edge on the munition head, and another on the casing (these contact points are denoted as orange points on the top image of Figure 7). Warheads roll in a linear motion because their weight bearing surface has a uniform diameter (contact points are denoted with orange lines in the bottom image of Figure 7). Note that all munitions that have bearing surfaces that are non-uniform in diameter (e.g., cartridges) will initiate motion and reorient to the flow direction (top image of Figure 7). Then, for these cartridge-type munition to move again, velocity must exceed the threshold for the 0 degree angle of attack. Thus, for all munitions that have bearing surfaces that are non-uniform in diameter, it can be argued that only the threshold for the 0 degree angle of attack is of importance for migration of the munition. Otherwise, for munitions that have bearing surfaces that are uniform in diameter (e.g., cylinders, warhead, 81 mm mortars) the initiation of motion threshold velocities for various angles of attack are all important for predicting motion of the munitions.

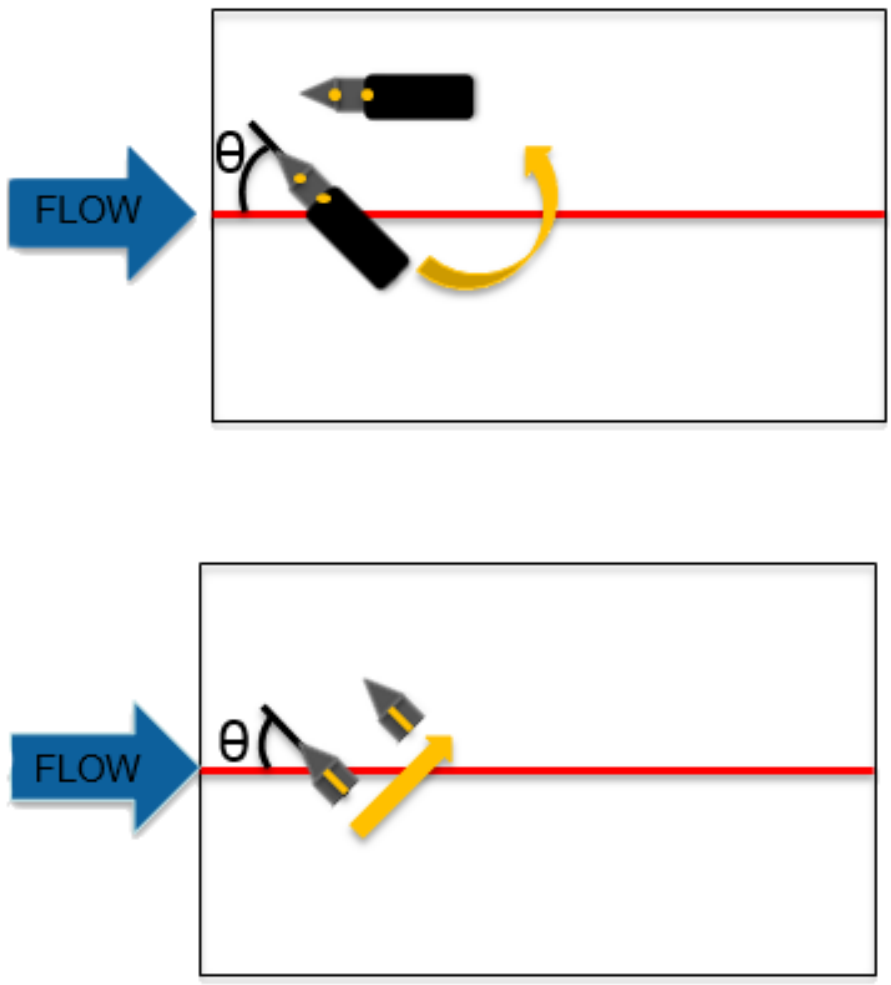

Figure 7: Schematic of initial motion behavior for cartridges (top image) and warheads (bottom image). Cartridges rolled on two weight-bearing points in a conical motion. Warheads rolled linearly on a cylindrical weight bearing surface (weight-bearing contacts indicated by orange points or lines).

The results of initiation of motion experiments performed in the WHOI flume show a clear relationship between the angle to flow, and the mean flow velocity required to move the munition (see Figure 8). As the cartridge and warheads approach an angle of 0°, less of the munition's surface is exposed to the flow. Thus, as this projected area of the munition decreases, the velocity necessary to initiate transport increases. Also, it was observed that the fins of the 81 mm mortar enhanced rolling resistance as compared to the 81 mm finless mortar (see Figure 8). Motion could not be achieved for any munition or warhead in the WHOI flume when placed parallel to the streamwise direction ($\theta = 0°$), prompting experiments to be moved into the STF.

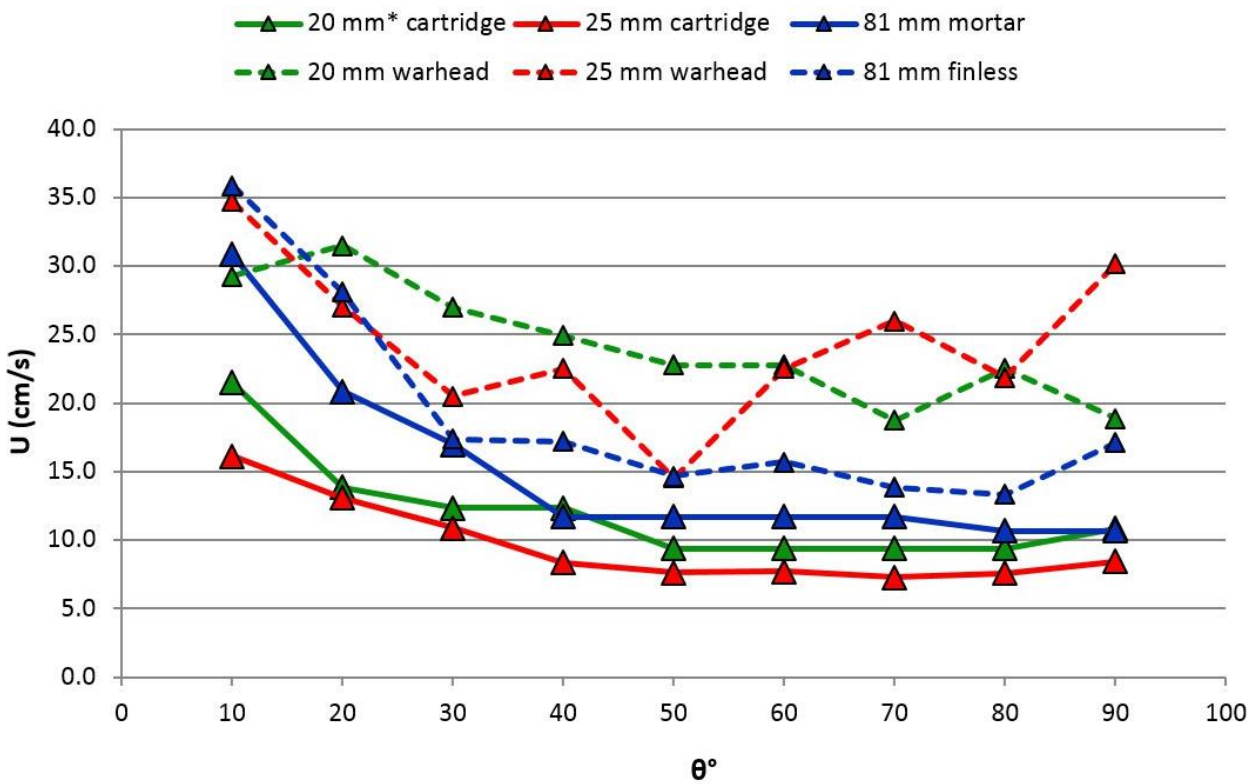

Figure 8: Initiation of motion for munitions and warheads on a horizontal PVC bottom. Note the * denotes that the NRL surrogate used.

Initiation of motion of the munition when placed in line with the streamwise direction (θ = 0°) could not be achieved in the WHOI flume. The width of the flume was not reduced by encroachment in the WHOI flume because the flume walls were not deep enough to accept the resulting increased water depth. Therefore, experiments were continued in the STF, which is both deeper than the WHOI and can produce a slightly more powerful flow.

During θ = 0° trials in the STF, it was found that none of the munitions could be moved on a horizontal bed (slope=0.04°, taken as a horizontal bed) on the flume's original rough steel. A smooth PVC patch (material similar to the WHOI flume bottom) was installed. This also failed to yield transport when placed at θ = 0°, even at the highest flow velocity available to the STF (maximum flow velocity of 0.91 m/s). However, rocking movements were observed when high flow rates were applied to munitions placed at θ = 0° on both the steel bottom and PVC patch.

At this point, a mild slope was applied to the STF (slope of 0.4°). With this slope, the 20 mm and 25 mm cartridges in θ = 0° trials achieved stochastic downstream transport on the PVC patch during high flow rates, with initiation of motion becoming more likely as flow was increased. The observed stochastic transport of the 20 mm and 25 mm munitions occurred in three ways:

1) The munition rocks in the violent flow, moving a small distance downstream with each rock (< 1 mm), see top image in Figure 9.

2) The munition suddenly slips downstream a short distance before coming to an abrupt stop (see middle graphic in Figure 9).

3) The munition slips downstream a short distance, but becomes slightly misaligned with the flow and rolls downstream on an angle (refer to bottom image in Figure 9).

As flow rate increased, motions described in observations 2) and 3) became significantly more likely to occur.

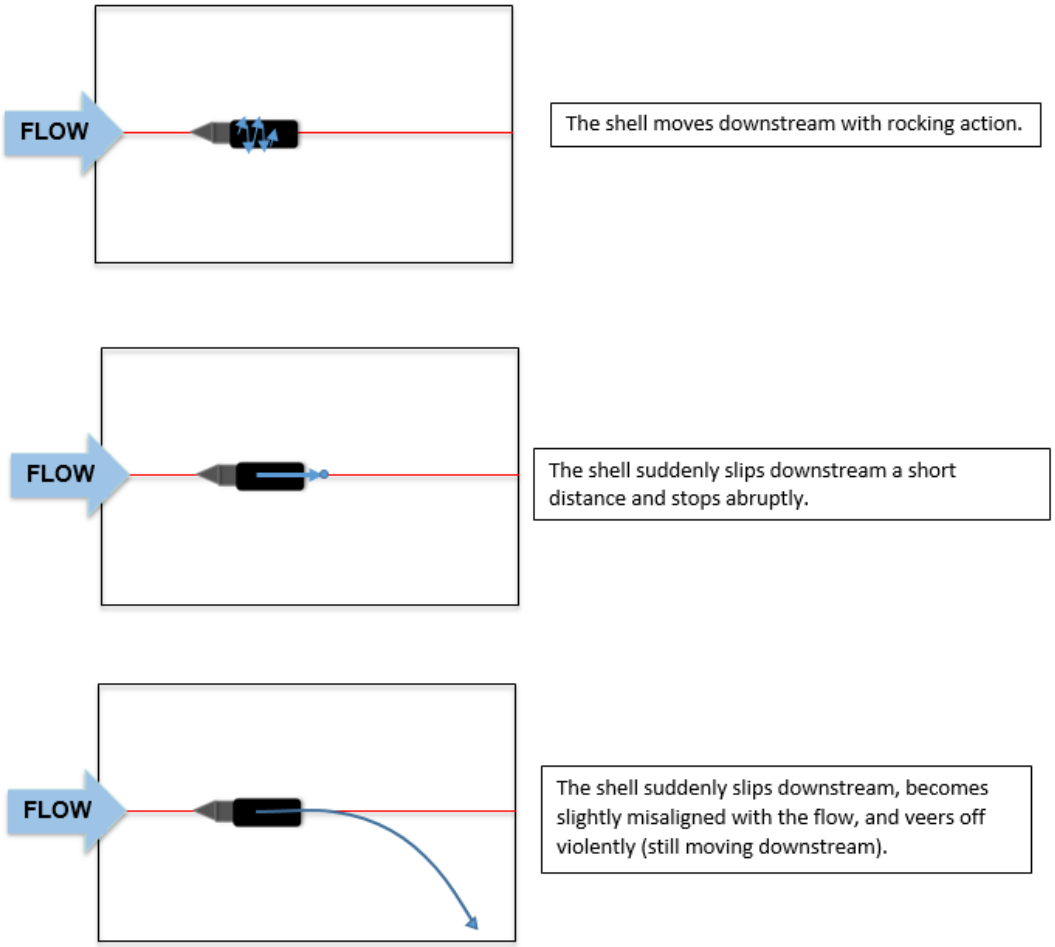

Figure 9: Overview of observed transport behaviors over PVC patch in STF (observations 1, 2, and 3 are listed from top to bottom).

From the above it becomes clear that angle of attack and the corresponding projected area plays an important sole on the definition of critical conditions for the incipient motion of the munitions. To confirm the effect of the angle of attack numerical modeling was conducted to numerically estimate the drag force of the flow on a 25 mm munition for various angles of attack. The results suggest that for a given flow velocity the drag force may vary up to nine times compared to the 0-degree angle of attack which is the angle of attack that corresponds to the

minimum streamwise drag force. Another, outcome from this set of simulations is that the effect of viscous/friction related drag forces, which comes from the friction between the water and the munition, are significantly smaller than this of the pressure drag which is associated to the flow separation and wake behind the munition.

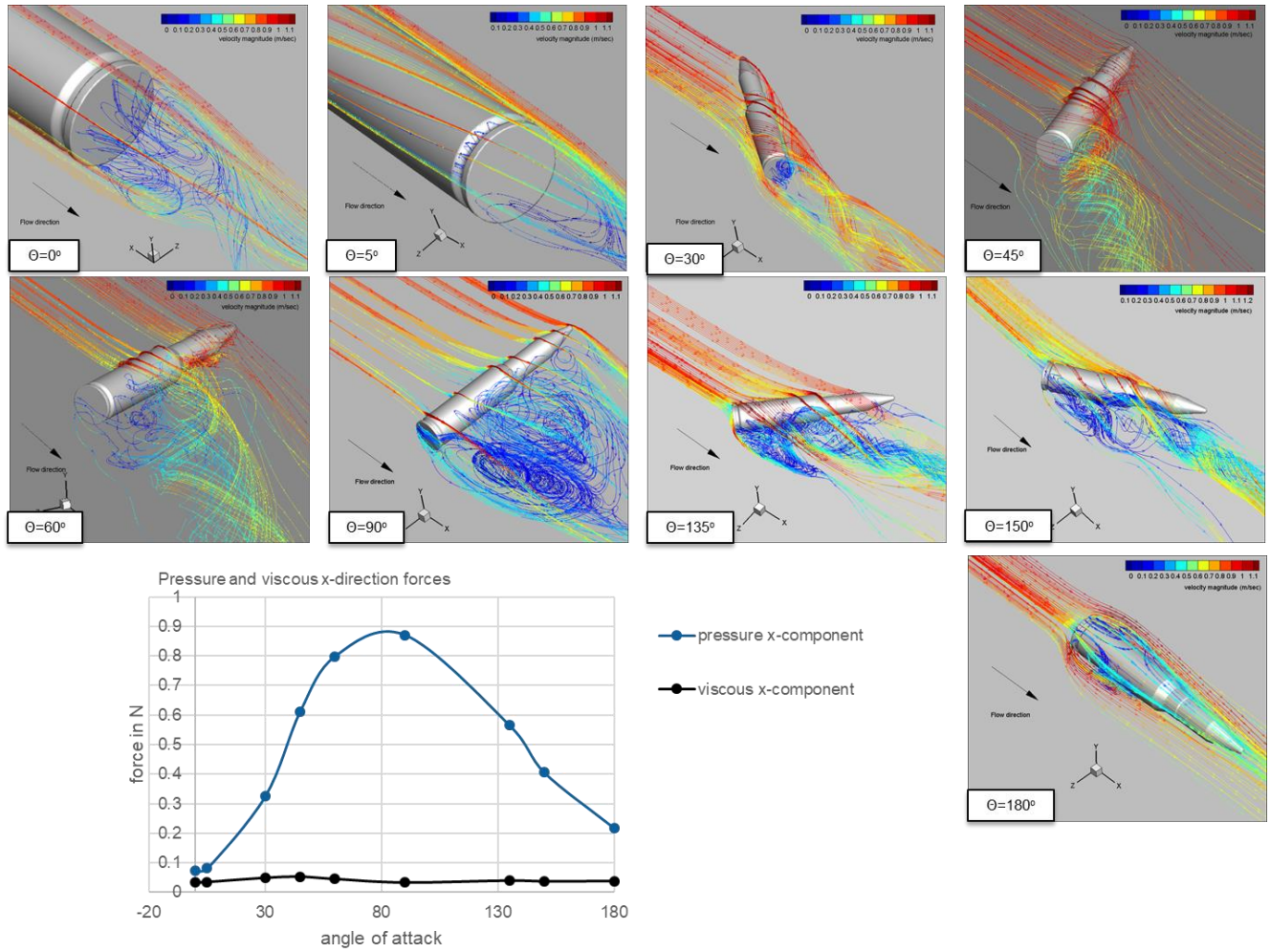

Figure 10: Effect of angle of attack on the streamwise drag forces from accompanying CFD modeling

Offset cartridge trials were conducted in the STF on both the horizontal and mildly sloped beds with rough steel bottoms (see Figure 11). The results of shell offset trials on steel bottom in the STF with and without slopes are very similar to each other. We expect that the local roughness of the steel bed around the munition is enough that the munitions are held in place by individual bumps and divots in the steel. The steel provided enough traction for the cartridges to be set reliably, and yielded a similar relationship between angle and motion-inducing flow velocity to the results found in the WHOI flume on smoother PVC bottom. Due to the increased roughness between steel and PVC, trials on steel required greater flows as can be seen in Figure 12.

Figure 13 depicts current experimental data (previously plotted in Figure 8, Figure 11, and Figure 12) to prior data compiled by Friedrichs (2013). It can be seen that current data regarding surrogate munitions is within the range of scatter of the prior data for spheres, cylinders, and natural sediment. Also, the current data provide a plausible reason for the spread in the data for each diameter; the initiation of motion velocity threshold is highly dependent on the angle of attack of the munition.

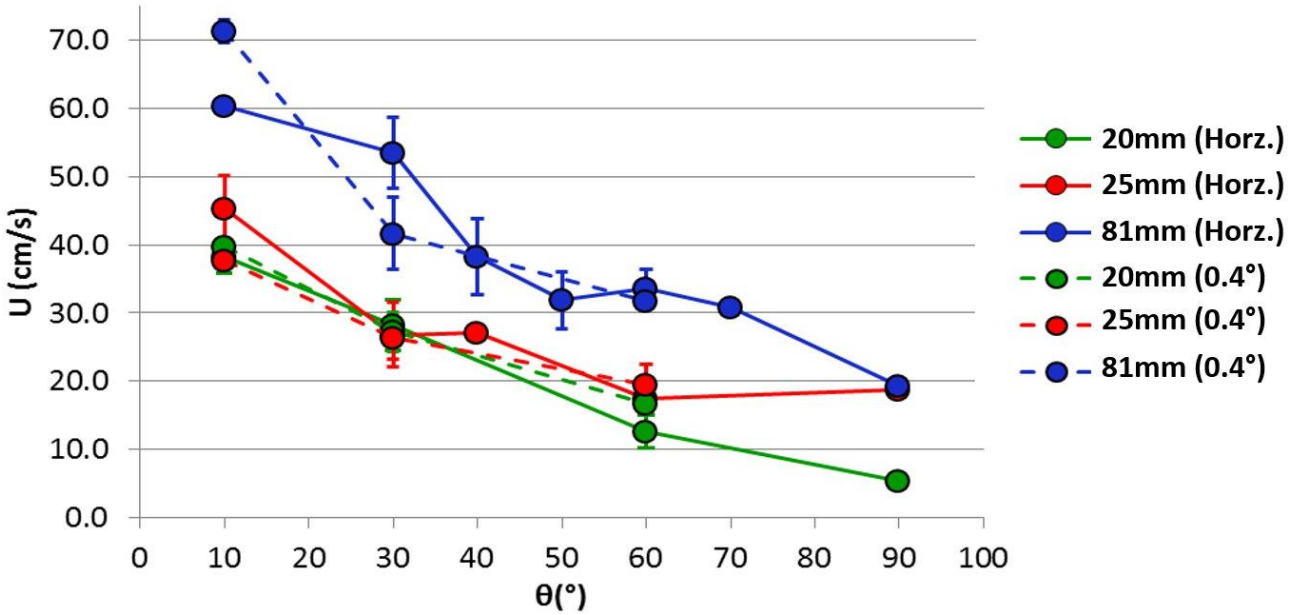

Figure 11: Effect of steel bed slope on cartridge offset trials. Two flume slopes are a mild slope of 0.4° and horizontal slope (Horz.) (slope of 0.04°, taken as horizontal).

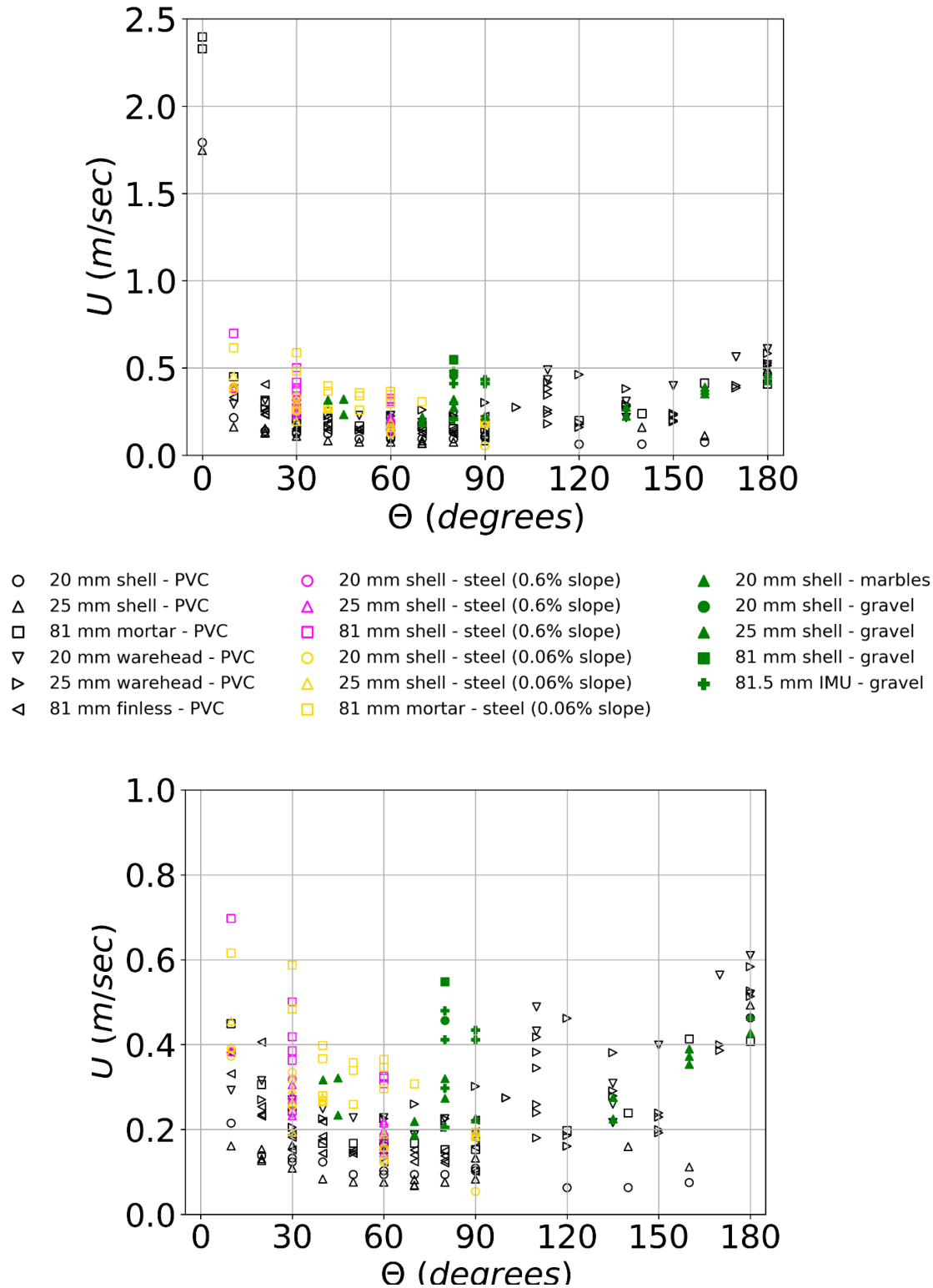

Figure 12: (top) Effect of horizontal bottom rough on cartridge initiation of motion. WHOI flume was used for PVC bottom and STF was used for the steel bed. (bottom) same plot excluding 0 degree angle of attack data

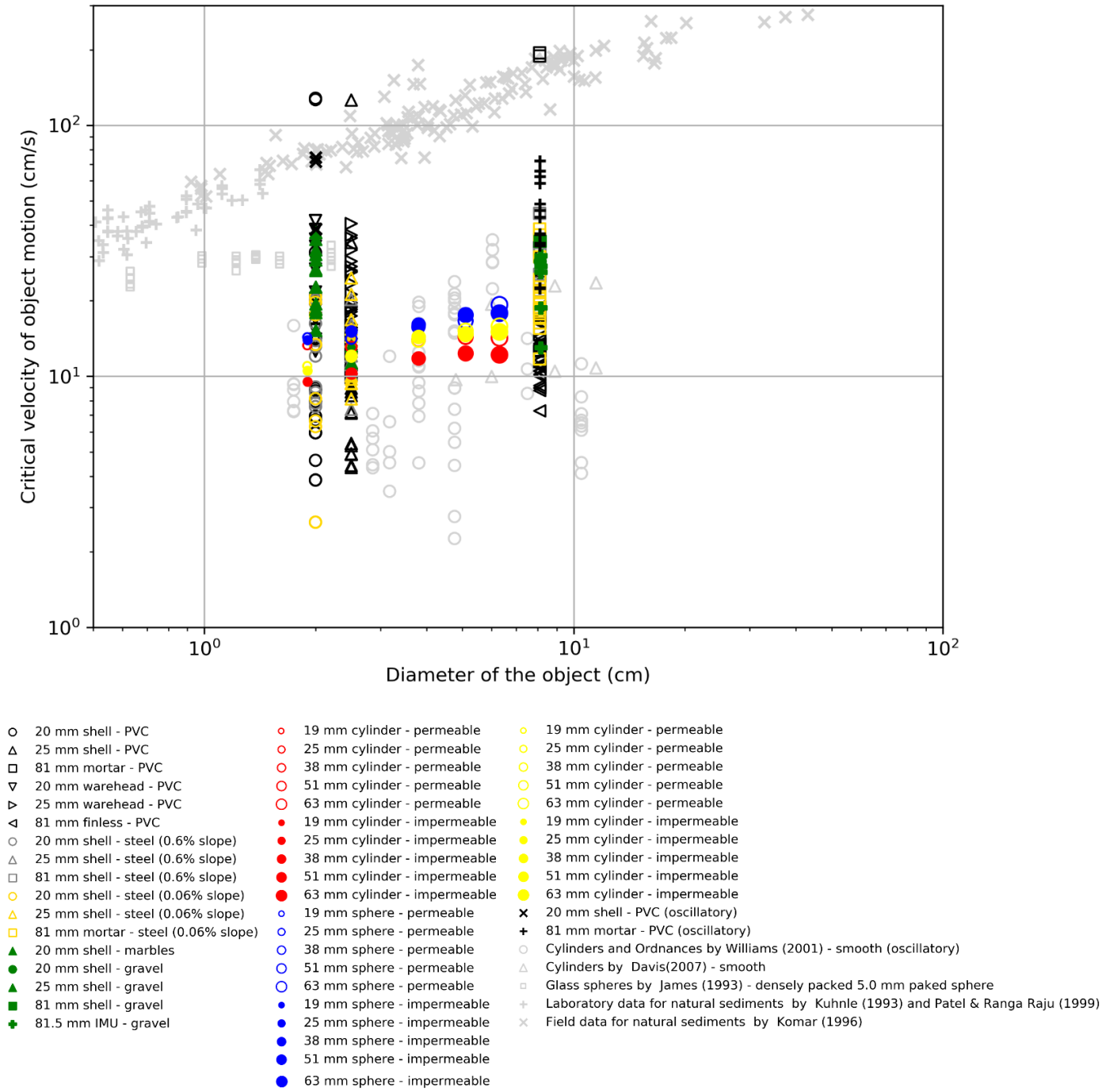

Figure 13: Comparison of the current initiation of motion experiments (from Figure 8, Figure 11, and Figure 12) to data compiled by Friedrichs (2013). Light gray symbols (bottom right of legend) are data compiled from Friedrichs (2013), references to each data set are included. All remaining symbols (black, dark gray, yellow, green, red, and blue) are from current experiments. Each legend entry for current experiments denotes munition type and substrate type. All flows are unidirectional unless denoted with "oscillatory" in the legend entry for oscillatory flows conditions. All experimental data listed in Appendix C is included in this figure.

The results from the canonical case (spheres and cylinders) is presented in Figure 14 and compared with James (1990). The plot shows good agreement for the spheres and cylinder set 2 (constant and smaller *L/D*) with the results from James (1990), which is a set of experiment of initiation of motion of a sphere on a bed composed of uniform size spheres, to examine the inverse relationship between the Shields parameter and the *D/k* value.

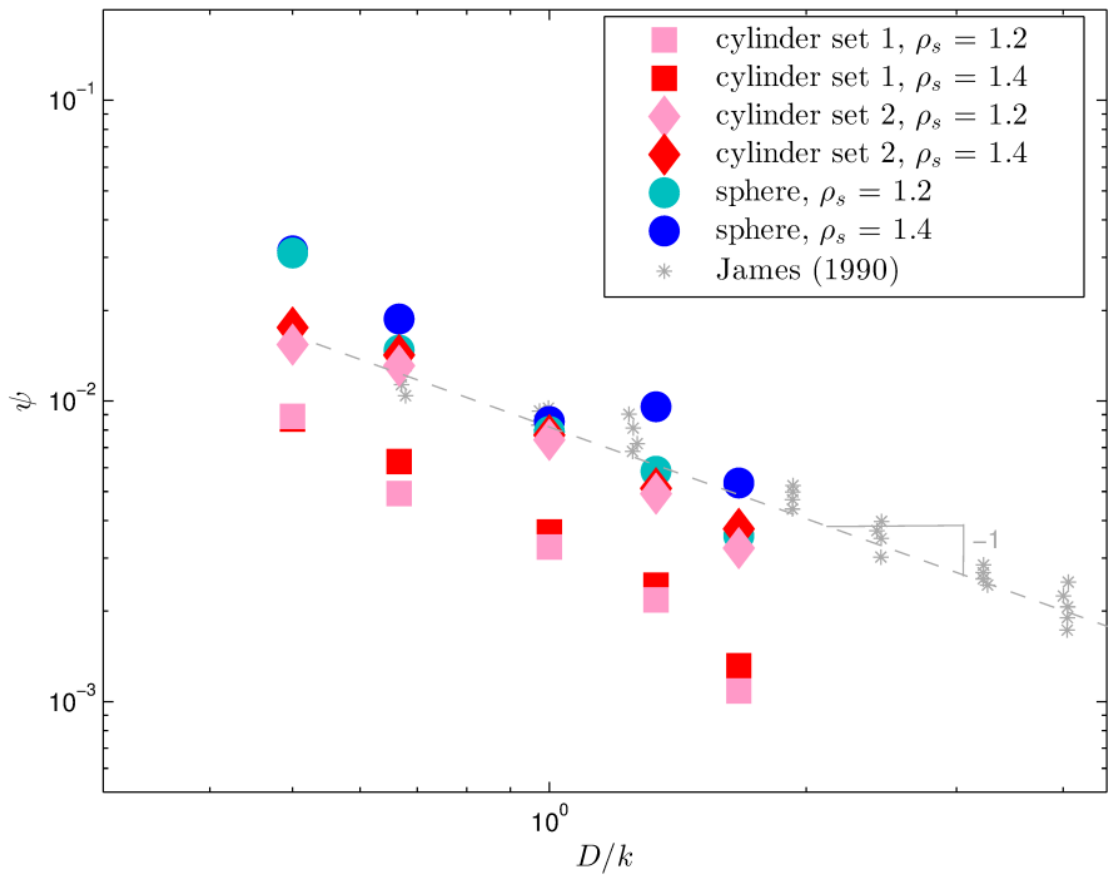

Figure 14: The Shields parameter plotted against the ratio of the particle size to bed roughness size and compared with the results obtained by James (1990). The dashed line with a minus one slope is superimposed for comparison.

5.2 Oscillatory Flows

The mechanisms for motion were observed for munitions on hard substrates under oscillatory flows includes pivoting (and realigning), rocking, and rolling. The motion type depends on the type and orientation of the munition. The munition would roll sideward when placed perpendicular to the flow direction and 180 degree pivoting was observed for munitions placed aligned with the flow.

Figure 15 illustrates the effect of the wave period on the maximum orbital velocity required to initiate the motion of the munition. The plot shows that for shorter wave periods, the threshold maximum orbital velocity increases with the wave period and reach a saturation at longer wave periods, in our case, 6 seconds. The result suggested that the impact of acceleration reduces for wave periods larger than about 6 seconds. This effect was observed regardless of the munition orientation (perpendicular or aligned with the flow direction).

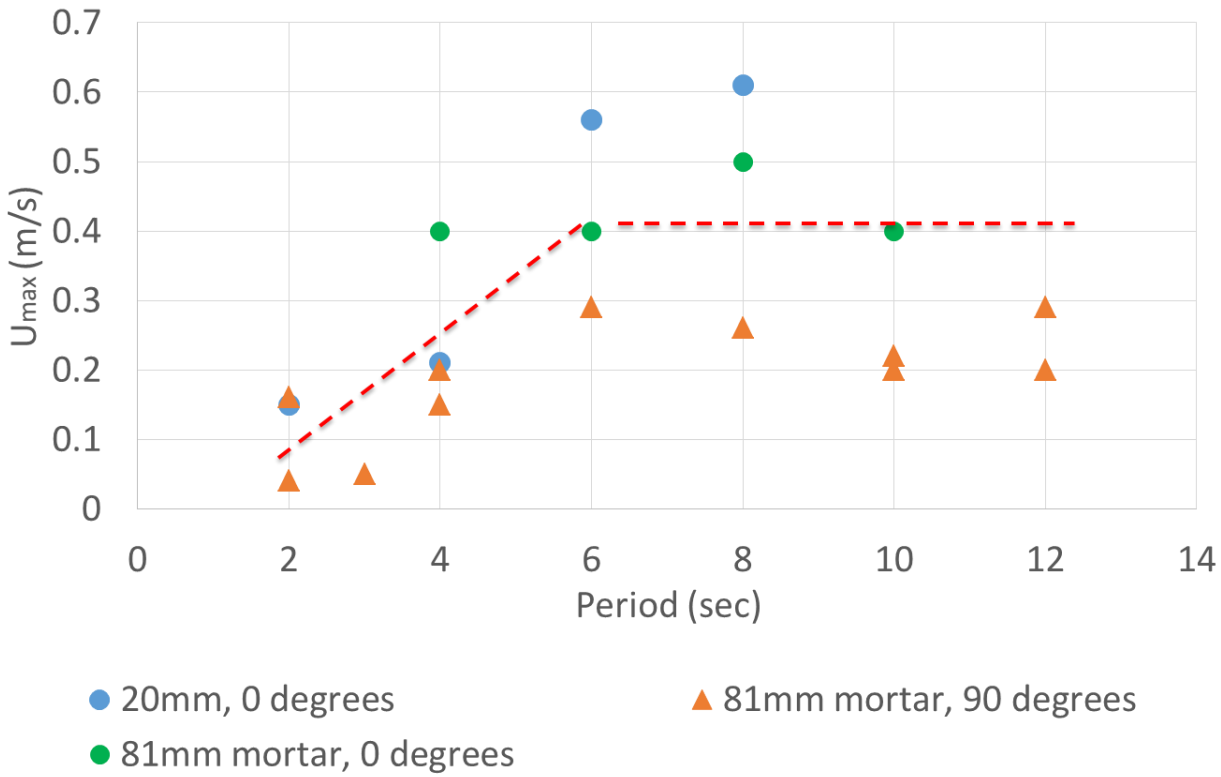

Figure 15: The threshold for initiation of motion at different flow periods shows that the impact of acceleration reduces at about T = 6 sec

5.3 Unified Scaling

A scaling analysis was carried out for the estimation of an empirical curve for the evaluation of the critical flow conditions required for the initiation of motion of the examined munitions. The important flow munition characteristics used in our analysis are shown in Table 5 and Table 6 in Appendix C.

Initially, the stability criterion, originally proposed by Isbash (1936) was tested with the initiation of motion conditions observed in the laboratory. The original Isbash model was developed for stones having a volume and specific weight equal to those of a sphere. Hence, the corresponding equivalent spherical diameter can be calculated using the following formula:

$$D_{Isbash} = \left(\frac{6W}{\pi \gamma_s} \right)^{1/3} \qquad \text{Equation 10}$$

where W is the UXO's weight, γ_s is the specific weight of munitions. The corresponding mobility parameter is as following

$$U_{cr\,Isbash} = C\sqrt{2g' D_{Isbash}}\ , \qquad \text{Equation 11}$$

where U_{cr} is the critical velocity at the level of the munition (at $y=D$) and g' is the reduced gravity and C is a constant which takes a value of 0.86 for highly turbulent flow and 1.2 for low turbulence flows.

Using the experimental observation from the experiments presented in Section 4.2, we can compute the ratio

$$C = \frac{U_{cr\,Isbash}}{\sqrt{2g' D_{Isbash}}} = \Phi_{Isbash}\ . \qquad \text{Equation 12}$$

A plot of Φ_{Isbash} can be found in Figure 16. It can be seen that there is a significant scatter in the plot which may be attributed to the effect of the geometric characteristics of the munition, effect of the different projected area for different angles of attack and the bed-UXO contact area.

To include the effect of the geometric characteristics of the munition, and aiming to decrease the scatter of the observed data, we introduced a new length scale ℓ for analysis of the results which takes into consideration the area of the munitions which is perpendicular to the flow (projected area) as well as the total volume of the munition. A characteristic example that illustrates the importance for the parameter ℓ is shown in Figure 17 b) and c) where the difference between a case of a plate and a cylinder is shown. The estimation of parameter ℓ for the aforementioned examples is shown below:

<u>Plate:</u>

$V_o = HDt$

$A_p = HD$

$\psi = V_o / A_p = t$

<u>Cylinder:</u>

$V_o = \pi HD^2 / 4$

$A_p = HD$

$\psi = V_o / A_p = \pi D / 4$

$$\ell = A_p / \psi = A_p^{\,2} / V_o\ , \qquad \text{Equation 13}$$

where H is the width of the plate or cylinder, V_o is the volume of the obstacle, A_p is the projected area (computed via CAD model for each munition), t is the thickness of the plate, D is the diameter of the cylinder, ψ is the ratio between the volume and the projected area of the obstacle.

Table 3: Flow and munition variables.

Flow Characteristics:	Munition Variables:
U: time-averaged cross section averaged velocity	V_o: munition volume
U_{cr}: velocity at the level of the munition D	D: munition diameter
ν: viscosity	ρ_s: munition density
ρ: water density	g': modified gravity
k_s: roughness height	A_p: projected area
δ: boundary layer thickness	
η: Kolmogorov scale (~viscous layer)	

In Figure 18, a modified version of Figure 16 for which the dimensionless length D_{Isbash}/ℓ. It is clear the introduction and use of the length scale ℓ, which includes the effect of the projected area, helped in reducing the scatter in the plot, suggesting that C is also affected by the geometric characteristics of the UXOs. This geometry effect was not included in the original work of Isbash (1936).

Also, to be able to include the roughness effect and to compare results from cases of different bed roughness as well as cases of flat bed, a unified hydrodynamic roughness approach (Gioia and Chakraborty, 2006) was adopted. According to this approach, we define the following unified hydrodynamic roughness:

$$s = \underbrace{\beta\eta}_{\text{viscous scale}} + \underbrace{k_s}_{\text{roughness scale}} \qquad \text{Equation 14}$$

where $\eta = \delta \mathrm{Re}^{-3/4}$ a Kolmogorov scale, $\mathrm{Re} = \frac{U\delta}{\nu}$, δ is a characteristic hydraulic length (e.g. water depth or half the channel height), β is a constant and k_s the roughness height (typically calculated as 2.5×k where k is the height of the bed grains).

For the case of oscillatory flows instead of the viscous scale η an alternative formula introducing the Stokes length has been used:

$$s = \underbrace{\delta_b}_{\text{viscous or Stokes length}} + \underbrace{k_s}_{\text{roughness scale}} \qquad \text{Equation 15}$$

where the Stokes length δ_b can be calculated:

$$\delta_b \sim \begin{cases} \beta\delta\,\mathrm{Re}^{-3/4} & \text{for unidirectional flows} \\ \beta\sqrt{\dfrac{\nu T}{\pi}} & \text{for oscillatory flows} \end{cases} \qquad \text{Equation 16}$$

where β is a constant (here we assumed β=0.01). Using the two length scales above we can define a dimensionless ratio, $\ell/(c\eta+k)$.

In Figure 19, the Φ_{Isbash} mobility parameter versus the dimensionless ratio ℓ/s is plotted. Is can be seen that the data scatter is further reduced. Another important output of this plot is that the data form two distinct regimes: a) low roughness regime (in which the oscillatory data are also included) and b) high roughness regime. The coefficients R^2 are calculated both for the low and high roughness regions (R^2=0.352 and R^2=0.415 respectively) as well as the total R2 coefficient (R^2=0.364).

Thus, the mobility parameter may be multiplied with a correction factor which will include the ratio between water depth and roughness ratio $(H_c/k_s)^{\gamma}$, where γ is an exponent estimated using best fit; in the current data set chosen to be equal to -½.

Thus, the new mobility parameter, including the relative roughness, can be written as

$$\Phi_{Isbash} = \left(\frac{H_c}{k_s}\right)^{\gamma} \frac{U_{cr\,Isbash}}{\sqrt{2g'D_{Isbash}}} \qquad \text{Equation 17}$$

In Figure 20, the Isbash mobility parameter multiplied with the $(H_c/k_s)^{-1/2}$ is plotted. It is clear that the data collapsed in a single curve that can be used for the prediction of the initiation of motion of UXOs. An empirical equation is produced using the above data and a best fit algorithm (Python) according to which Φ_{Isbash} can be predicted as a function of ℓ/s as

$$\Phi_{Isbash} = \left(\frac{H_c}{k_s}\right)^{-1/2} \frac{U_{cr\,Isbash}}{\sqrt{2g'D_{Isbash}}} = 0.138\left(\frac{\ell}{s}\right)^{-0.619} \qquad \text{Equation 18}$$

The corresponding coefficient R^2 of the regression is 0.929.

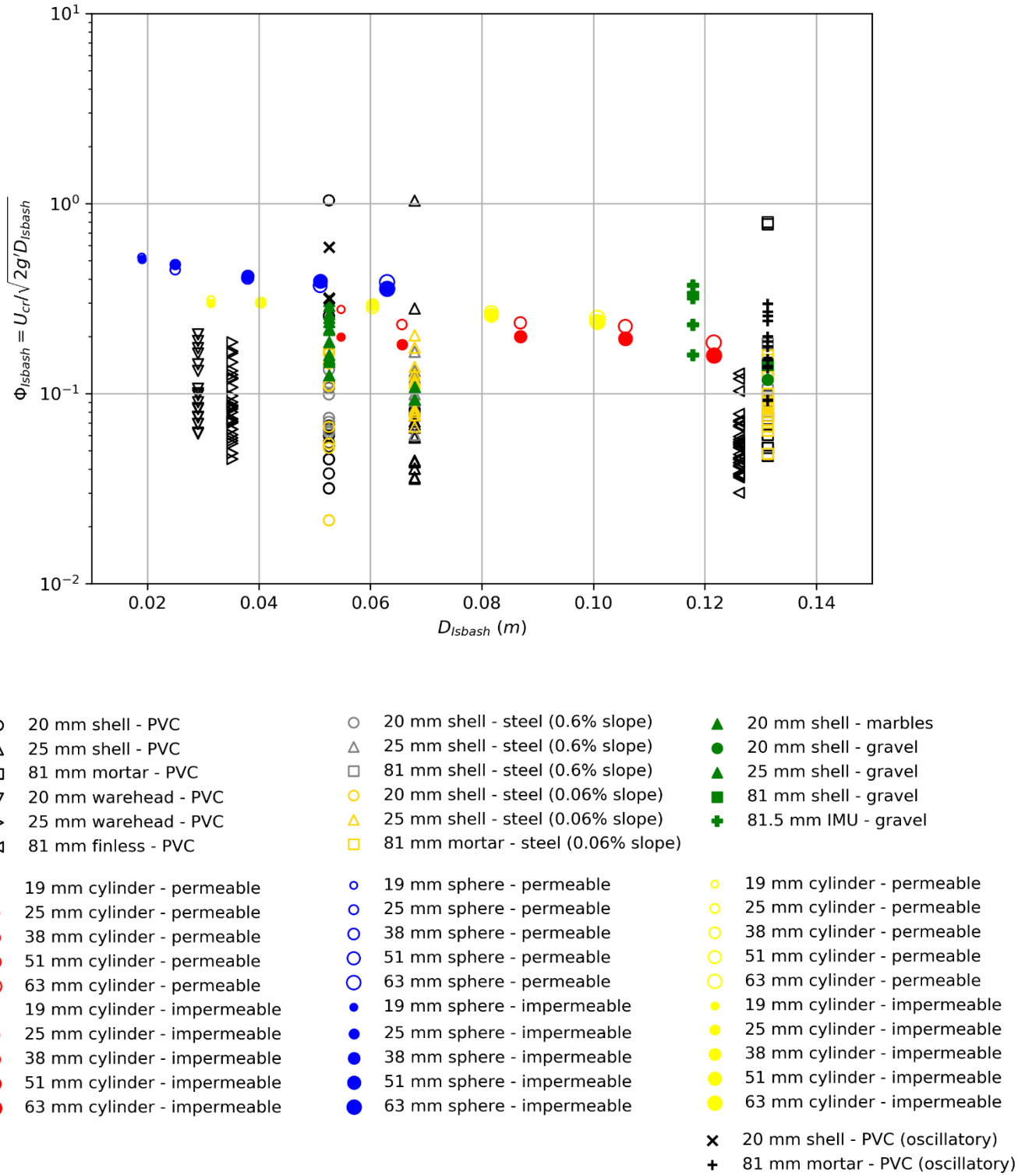

Figure 16: Isbash analysis plot (R^2=0.056)

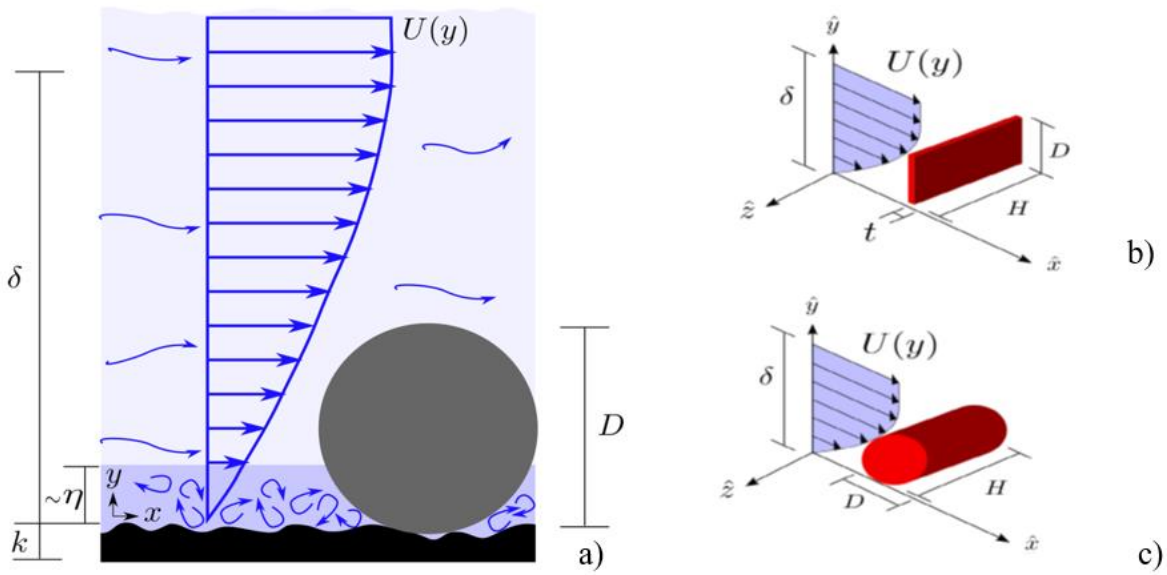

Figure 17: a) Schematic of flow around munition, b) flow around a plate (right-top), and c) flow around a cylinder

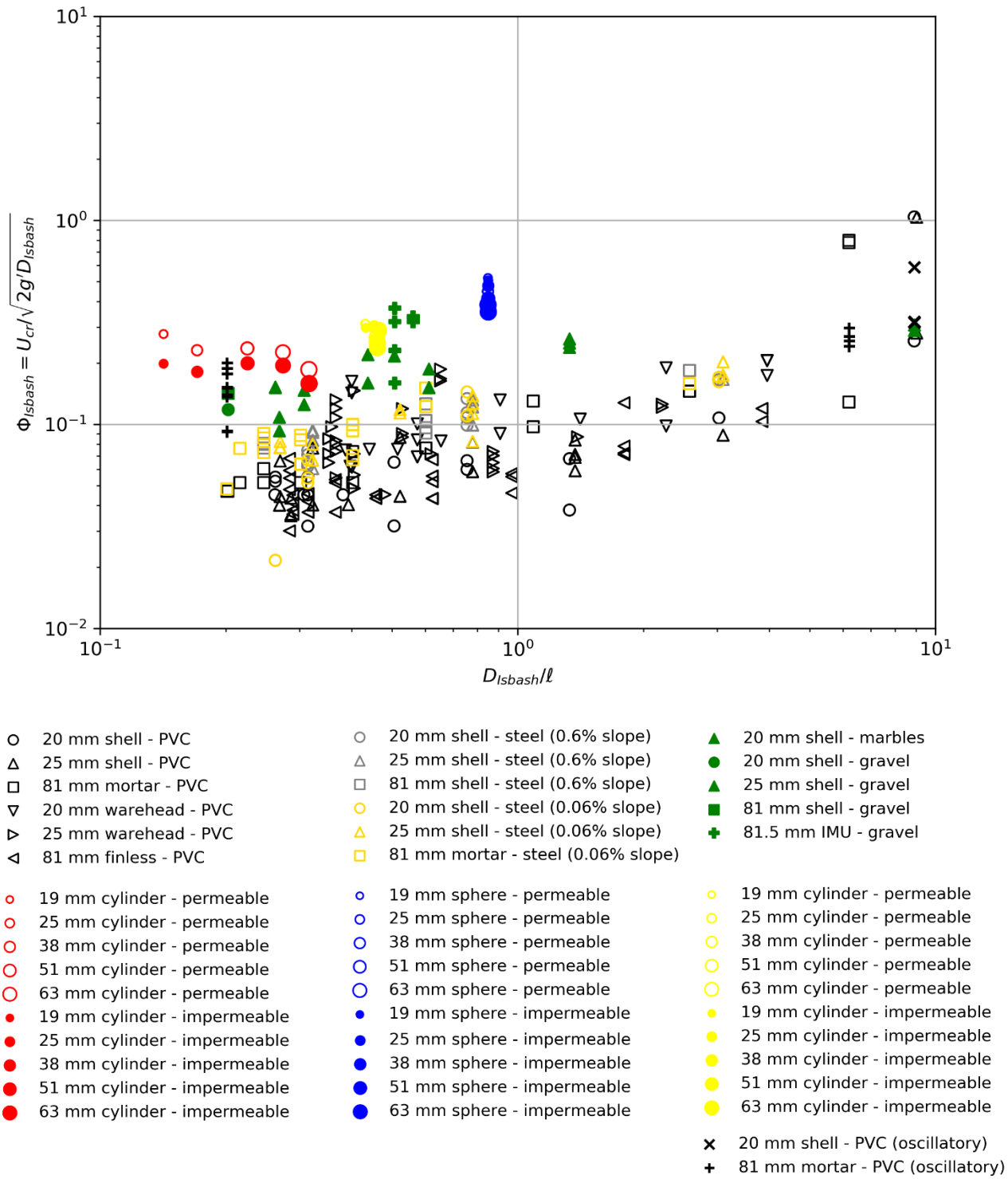

Figure 18: Isbash analysis plot (Φ_{Isbash} vs D_{Isbash}/l) (R^2=0.228)

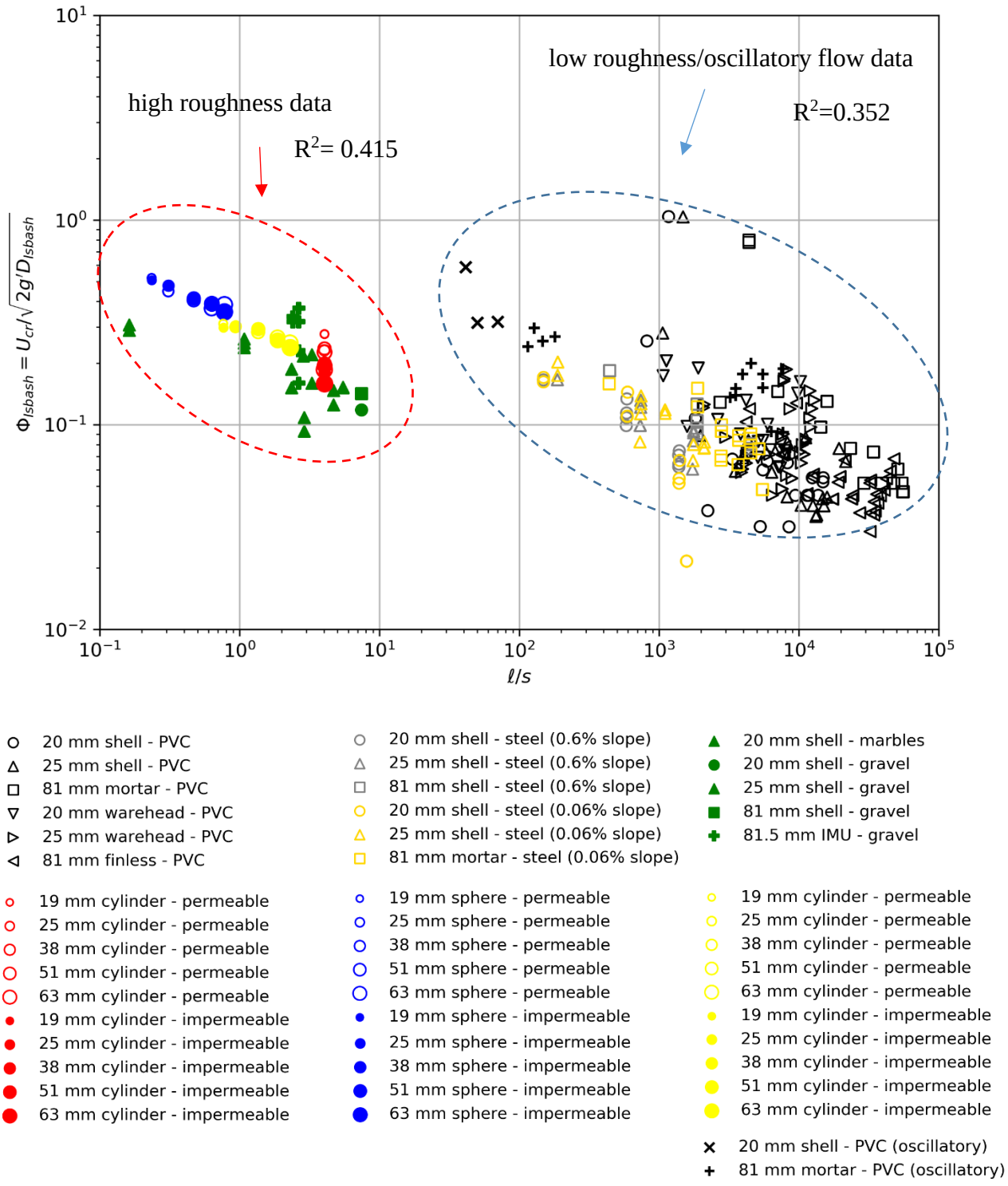

Figure 19: Isbash analysis plot (Φ_{Isbash} vs l/s) (total R^2=0.364)

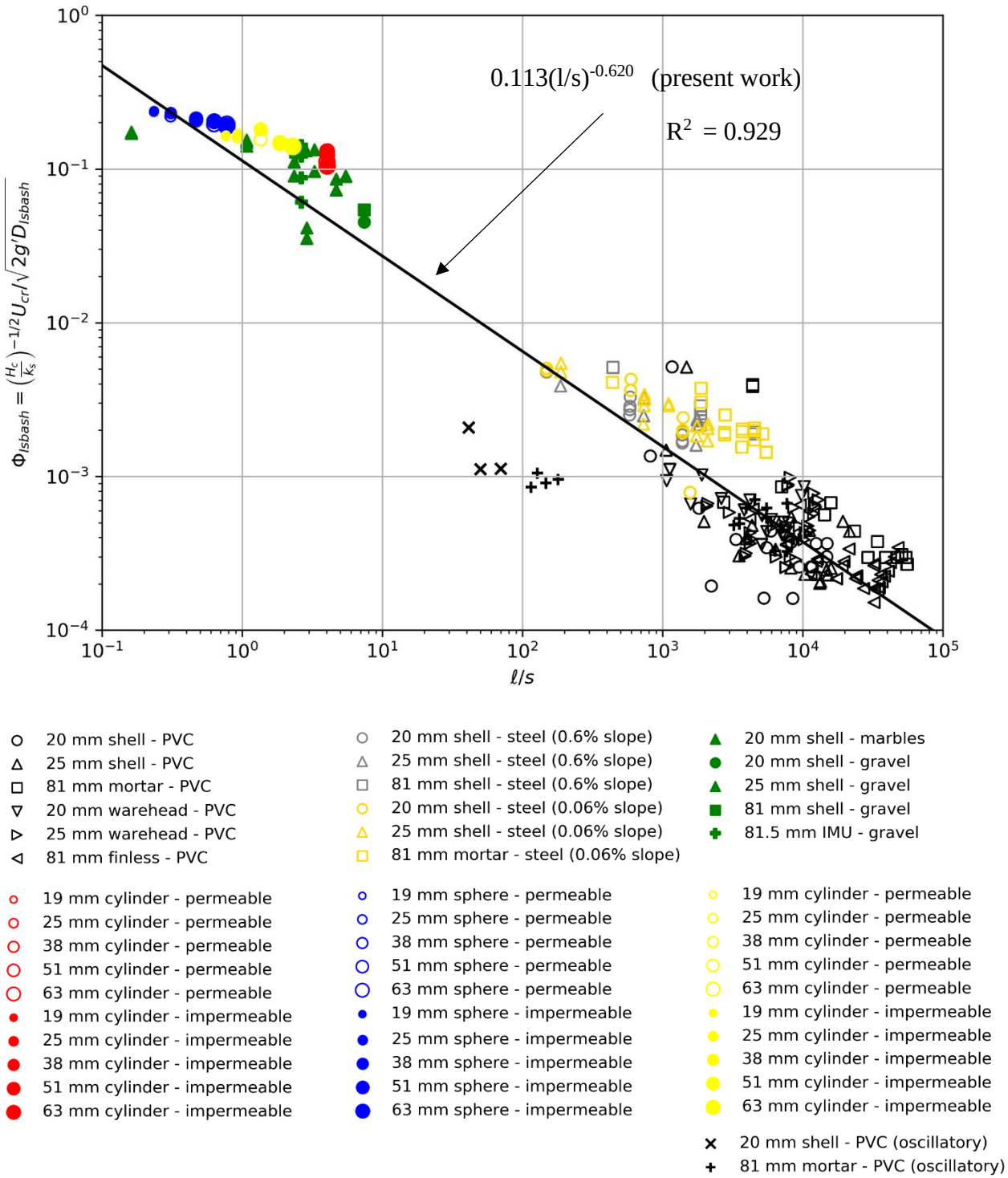

Figure 20: Modified Isbash analysis plot (Φ_{Isbash} vs *l/s*) (R^2=0.929)

We can now define a dimensionless critical velocity Φ_1 (mobility parameter) based on the length scale ℓ, to plot the experimental observations in a non-dimensional/ global form. Parameter Φ_1 can be defined as

$$\Phi_1 = \frac{U_{cr}}{\sqrt{g'\ell}} \qquad \text{Equation 19}$$

For the case of oscillatory flow, a correction factor f_I derived using Morison' equation (refer to Appendix D) is used to include the effect of acceleration/inertia,

$$f_I = \left(\frac{F_D + F_I}{F_D}\right)^{1/2} \approx \left(1 + 4\pi\left(C_I/C_D\right)/\left(KC\right)\right)^{1/2} \qquad \text{Equation 20}$$

where *KC* is the Keulegan-Carpenter based on length scale V_0/A_p ($KC = UT/(V/A_p)$), where *U* is the velocity of oscillation and *T* is the period to oscillation), C_I/C_D is the ratio of inertia vs drag force coefficients. Note the power 1/2 is required due to the fact that Φ_1 parameter used for U_{cr} instead of U_{cr}^2.Typically, $C_I/C_D \approx 2$ for $KC <\sim 30$. Also, for steady state ($KC \rightarrow \infty$), $f_I \rightarrow 1.0$.

Rennie et al. (2017) used a similar equation for the acceleration/inertia effects $f_I' \approx \left(1 + 16\pi^2\left(C_I/C_D\right)^2/\left(KC\right)^2\right)^{1/2}$. However, in their analysis they also did not include the effect of the angle of attack since all the examined munitions were placed perpendicular to the mean flow direction. In their work they developed a relationship between the mobility parameter $\Phi = f_I' \frac{U_{cr}^2}{g'D}$ (where D here is the nominal diameter of the examined UXOs) and the dimensionless ratio D/k_s. In Figure 21, a plot of the present work's experimental observations is presented using the same approach with Rennie et al. (2017). Once again, there is a significant scatter in the data which is associated with the different angles of attack. In the plot the slope of -0.71 is also plotted define by Rennie et al. (2017).

Thus, the mobility parameter Φ_1 can be calculated as

$$\Phi_1 = f_I \frac{U_{cr}}{\sqrt{g'\ell}} \qquad \text{Equation 21}$$

In Figure 22, the experimental observations for the initiation of motion ($\Phi_1 = f_I \frac{U_{cr}}{\sqrt{g'\ell}}$) are plotted versus the dimensionless length scale ℓ/s. A scatter is still observed. From Figure 22, it is also shown that data scatter can be categorized in two distinct regions: a. the low roughness

bed region (please note that oscillatory data are also included in the low roughness bed case) and b. the high roughness region. The coefficients R^2 are calculated both for the low and high roughness regions (R^2=0.444 and R^2=0.767 respectively) as well as the total R2 coefficient (R^2=0.268). Thus, the mobility parameter may be multiplied with a correction factor which will include the ratio between water depth and roughness ratio $\left(H_c/k_s\right)^{\gamma}$, where γ is an exponent estimated using best fit; in the current data set chosen to be equal to ½. Thus, the mobility parameter can be written as

$$\Phi_2 = f_I \left(\frac{H_c}{k_s}\right)^{-1/2} \frac{U_{cr}}{\sqrt{g'\ell}} \qquad \text{Equation 22}$$

In Figure 23, the data for the mobility parameter Φ_2 is plotted versus the ℓ/s ratio. It is shown that better agreement between the mobility parameter and the ℓ/s ratio both for the unidirectional and oscillatory data. The small scatter observed may be attributed to the over prediction of acceleration effect using f_I which for low KC values (i.e., 0.1) can take values of ~10 (refer to Appendix D). Using best fit the following equation was found,

$$\Phi_2 = f_I \left(\frac{H_c}{k_s}\right)^{-1/2} \frac{U_{cr}}{\sqrt{g'\ell}} = 0.1709\left(\frac{\ell}{s}\right)^{-0.6311} \qquad \text{Equation 23}$$

The corresponding coefficient R^2 of the regression is 0.933.

In Figure 24, the data from the present study is plotted together with the oscillatory data from the previous work by Williams (2001).

In Figure 25, a similar mobility ($\Phi_3 = \left(\frac{H_c}{k_s}\right)^{-1/2} \frac{U_{cr}}{\sqrt{g'\ell}}$) parameter is plotted for which the acceleration effects are neglected ($f_I = 1.0$). The corresponding equation that can be found using best fit is,

$$\Phi_3 = \left(\frac{H_c}{k_s}\right)^{-1/2} \frac{U_{cr}}{\sqrt{g'\ell}} = 0.1679\left(\frac{\ell}{s}\right)^{-0.6314}. \qquad \text{Equation 24}$$

The corresponding coefficient R^2 of the regression is 0.929.

Finally, in Figure 26, mobility parameter Φ_2 is plotted versus the D/k_s ratio. Once again, a larger scatter is observed in the data suggesting that it is important to take into consideration the angle of attack and the corresponding projected area.

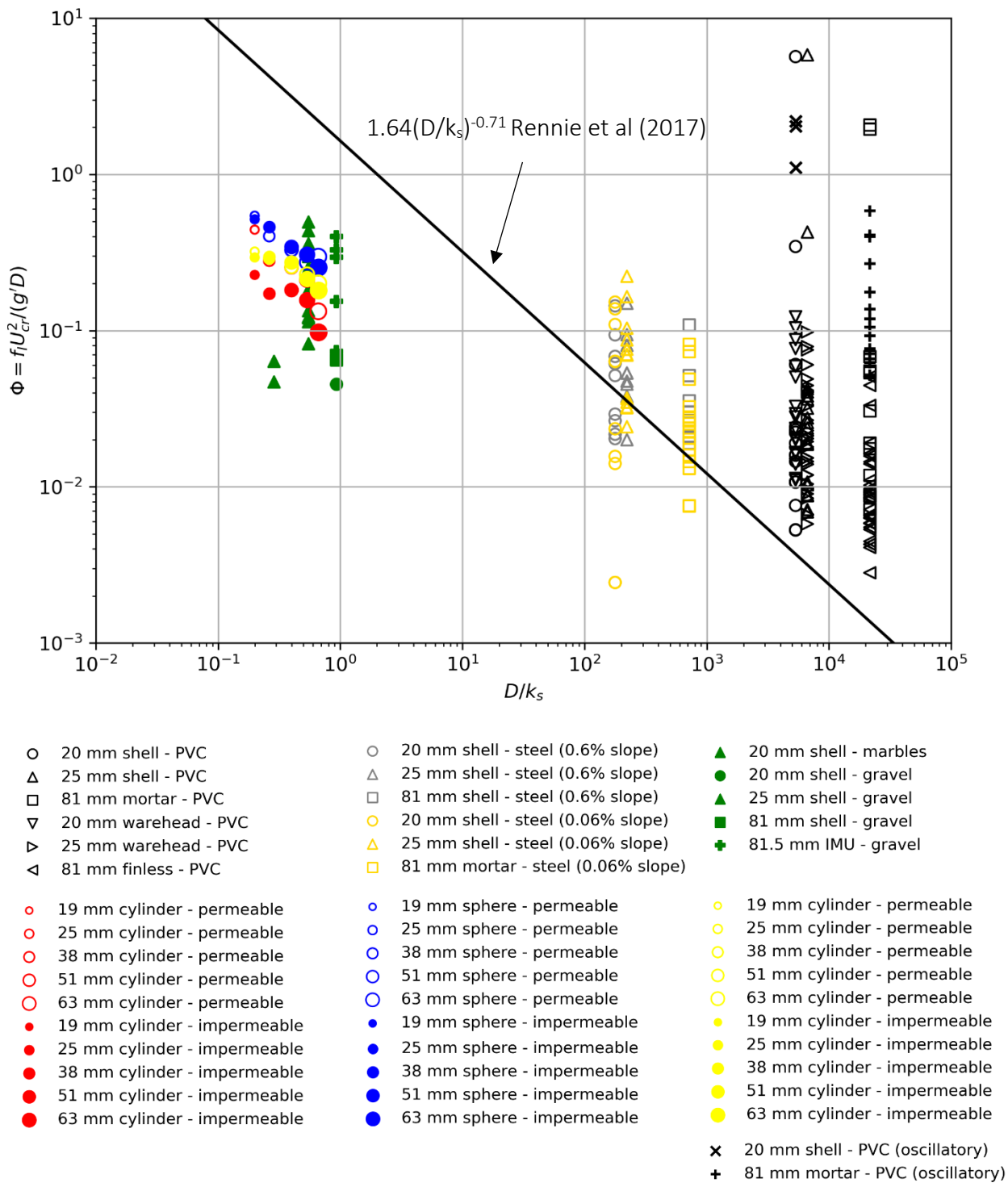

Figure 21: Experimental observation using Rennie et al. (2017) scaling (R^2=0.242)

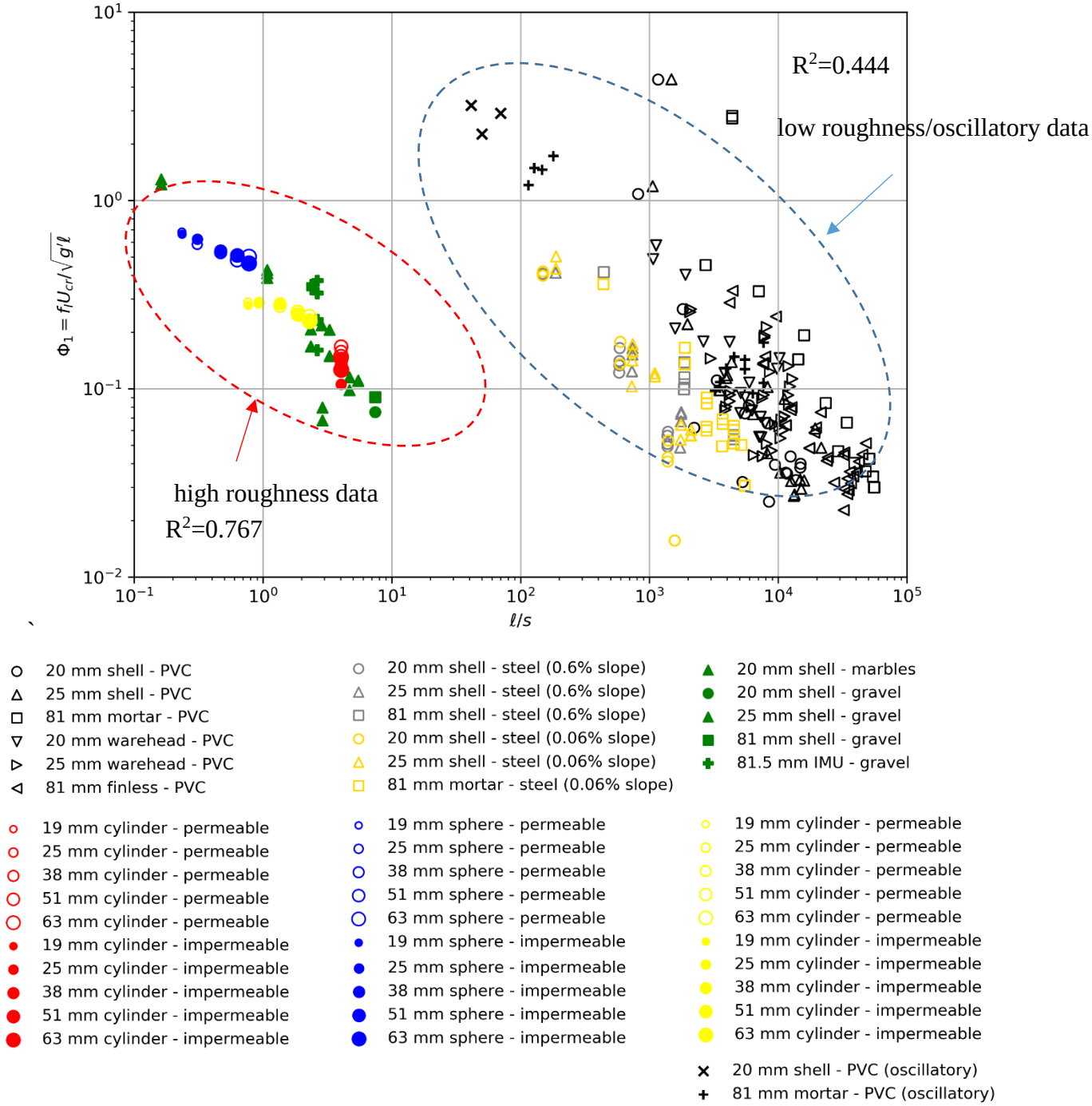

Figure 22: Experimental observation of critical flow velocity for the initiation of motion of different munitions (total R^2=0.268)

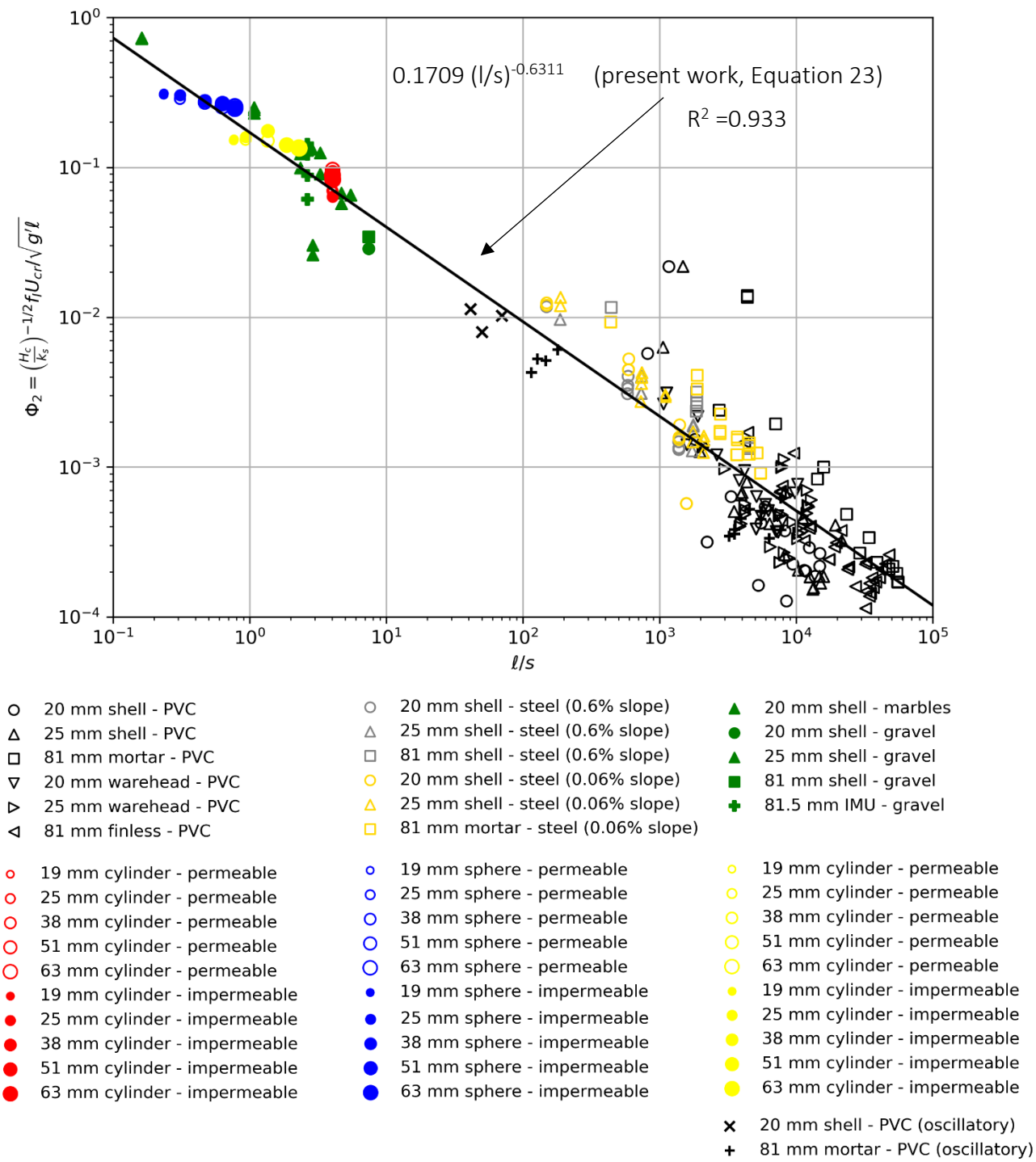

Figure 23: Modified mobility parameter Φ_2 which includes acceleration effects (f_I) versus l/s (R^2=0.933)

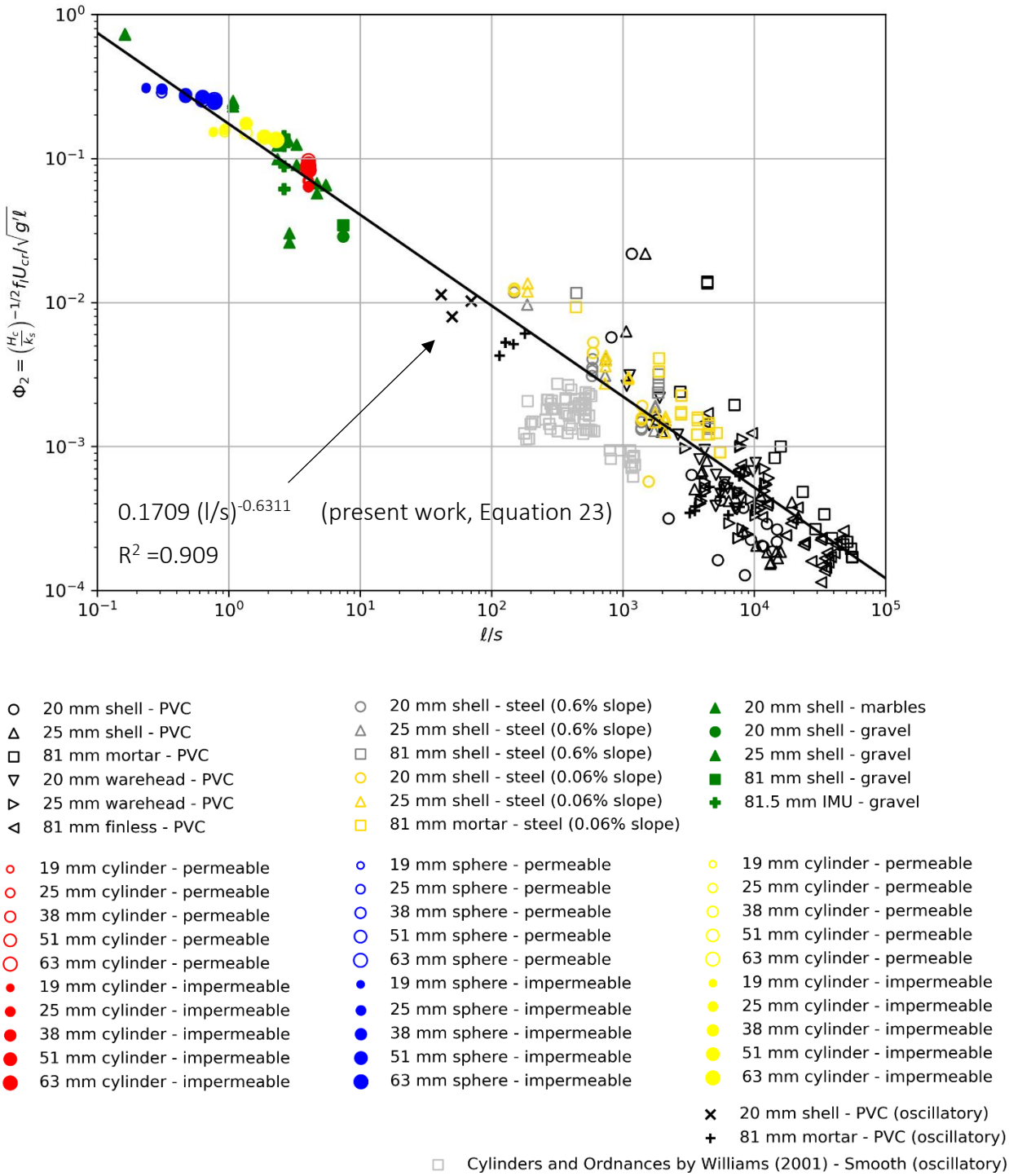

Figure 24: Modified mobility parameter Φ_2 versus *l/s* with additional oscillatory data from Williams (2001).

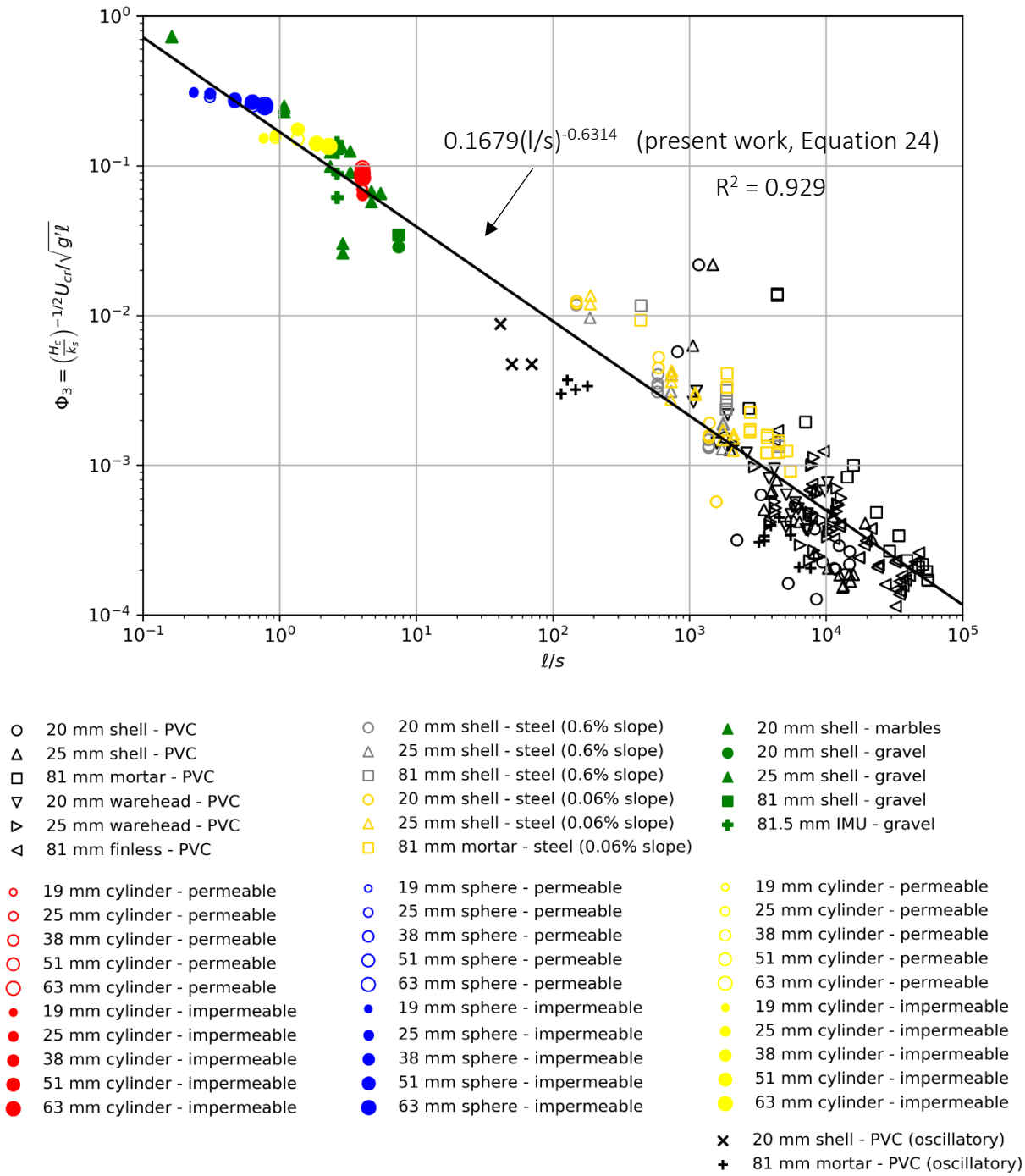

Figure 25: Modified mobility parameter Φ_3 which neglects acceleration effects ($f_I = 1$) versus l/s (R^2=0.929)

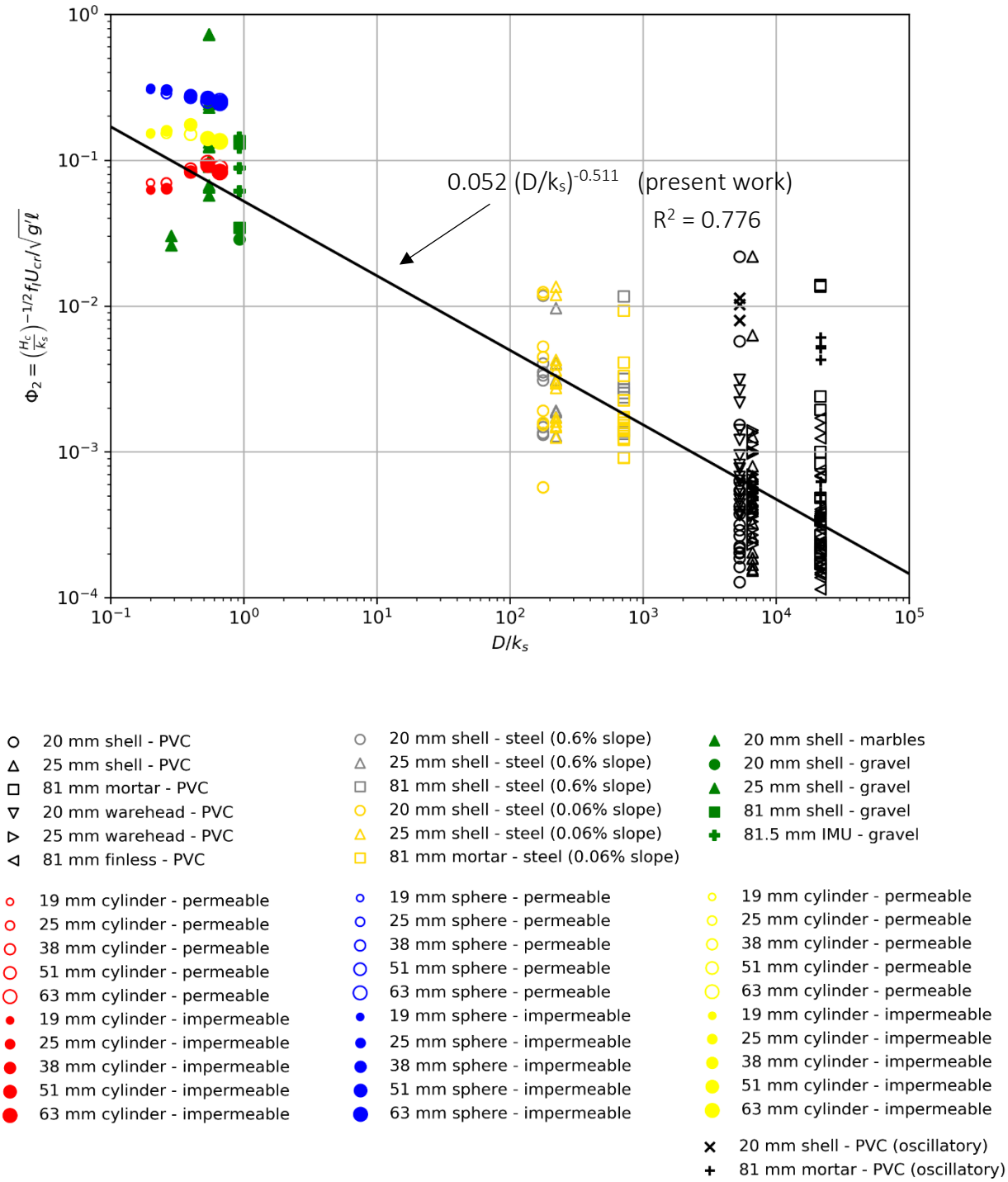

Figure 26: Modified mobility parameter Φ_2 versus D/k_s (R^2=0.776)

6. Conclusions

Initiation of Motion Findings on Hard Substrates

Under unidirectional flows over a hard substrate, all experiments show a strong dependence on attack angle (θ) on the mean flow velocity required to initiate motion. Furthermore, there is a pronounced transition between the 0° angle of attack and the rest of the angles. Once motion is initiated, cartridges initially placed at angles other than 0°, always realign to the 0° angle of attack orientation. The velocity threshold for initiation of motion at 0° is significantly higher than the rest of the angles. We expect that cartridges positioned on a hard substrate will initially move at lower velocities, align with the flow direction (i.e., 0° angle of attack), and remain in position until flow velocities exceed the higher velocity threshold for 0° angle of attack. For most munitions tested at a non-zero angle of attack, the relationship is most pronounced between 10°to 40° as well as 140° to 170°, as seen in Figure 8. Furthermore, PIV measurements and CFD modeling results (presented in Appendix E and F) provide detailed insight regarding the flow structure and separation zone that are highly altered with different angles of attack. The separation zone behind UXOs changes significantly the total force that munitions experience (Figure 10).

The contact geometry of the munitions on the hard substrate plays a key role regarding the initial munitions motion. The type of motion exhibited munitions with uniform and non-uniform bearing surfaces was distinct. Munitions with non-uniform bearing surfaces (e.g., cartridges) rolled at two points of contact as seen in Figure 7. The radius of the cartridge at the point of contact closer to the munition tip was smaller than the point of contact toward the middle of the cartridge. The cartridge contact geometry caused the munition to reorient as it rolled. Specifically, the munition would roll along an arc path, eventually coming to a stop at an orientation aligned with the flow direction regardless of its initial attack of attack. Conversely, munitions with uniform bearing surfaces (e.g., warheads and 81 mm mortars) retained the same (or similar) angle of attack after initiation of motion regardless of initial orientation. Since the warheads contact geometry is a line due to constant diameter along the contact length, warheads rolled in a linear path. Accounting for munition realignment with flow, 0° angle of attack velocity thresholds for initiation of motion are of primary importance for munitions with non-uniform bearing surfaces whereas the entire range of angle of attack velocity thresholds are important for munitions with uniform bearing surfaces. Thus, for munitions with non-uniform bearing surfaces on a hard substrate, the 0° angle of attack velocity thresholds for initiation of motion should be used regardless of initial munition orientation to the flow.

Regarding 0° angle of attack velocity thresholds, high velocity tests were conducted using the cavitation tunnel. Munitions tested with attack angle of 0° exhibited types of motion and transport (Figure 9) which were not observed in any offset trial (i.e., 10° to 180°). Trials with a 0° angle of attack frequently vibrated or rocked, inching back slowly with each tiny oscillation. This results in significantly higher critical velocity values for initiation of motion of UXOs for the 0° angle of attack. In general, the greater the

projected area of the munition exposed to the oncoming flow, the lower the flow velocity required to initiate motion.

In oscillatory flows, cartridges similarly realigned with the flow direction; however, since the flow direction alternated 180 degrees over the wave period, the cartridges constantly followed an arc path. In addition, initiation of motion under oscillatory flows has a dependence on wave period and near bed maximum orbital velocity as plotted in Figure 15. Results show that maximum near bed velocity required to initiate motion increases with the wave period, eventually reaching a saturation threshold at longer wave periods (~6 seconds). The effect was observed regardless of the initial orientation of the munition.

Also, initiation of motion is affected by bottom roughness. The characteristic length of the munition relative to the bottom roughness elements plays an important role. Small values of the relative roughness height parameter (ℓ/s) denote that the munition is significantly impacted by the bed roughness whereas large relative roughness values minimize the impact of roughness on the munitions. In general, for a given munition, the greater the relative roughness the lower velocities required to move the munition.

Furthermore, canonical (e.g., spheres and cylinders) experiments highlight the effect of munition shape on mobility. For large length to diameter values (i.e., large *L/D*), a higher Shields parameter is required to initiate motion of a sphere than for a cylinder with identical diameters. As the *L/D* value decreases, the cylinder approaches spherical geometry, and the threshold Shields parameter become similar.

Unified Scaling

A unified oscillatory/unidirectional scaling and a set of unified equations is proposed for the prediction of the critical flow conditions for the initiation of motion of UXOs on hard substrates when scour/burial is not pronounced. The proposed equations (Equation 18, Equation 23, and Equation 24) take into consideration the geometrical characteristics of the UXOs, angle of attack of the munition with respect to the flow, and roughness height of the bed. In addition, the acceleration/inertia effect for the case of oscillatory flows is taken into account. Both unidirectional and oscillatory initiation of motion flow conditions collapse into a single dimensionless equation highlighting the importance and practical applicability of the research work conducted under this project. To facilitate practical use of the report results a Python script in a Jupyter Notebook (refer to Appendix G and supplemental material) was developed using Equation 23 and data from Figure 24.

Literature Cited

Bayram, A., Larson, M., 2000. Analysis of scour around a group of vertical piles in the field. *J. Waterway, Port, Coastal, Ocean Eng.*, ASCE, 126(4), 215-220.

Bennett, R. H., 2000. Mine burial prediction workshop report and recommendations. Prepared for ONR, by Seaprobe, Inc. USA.

Butman, C. A., Chapman, R. J., 1989. The 17-meter flume at the coastal research laboratory. part 1. Description and user's manual. *Tech. rep.*, Woods Hole Oceanographic Research Center.

Carling, P. A., Kelsey, A., and Glaister, M. S. (1992). Effect of bed roughness, particle shape, and orientation on initial motion criteria. In: *Dynamics of Gravel-Bed Rivers*, P. Billi, R. D. Hey, C. R. Thorne, and P. Tacconi, eds., John Wiley and Sons, Chichester, United Kingdom, 23–37.

Calantoni, J., 2014. Informal Workshop on Burial and Mobility Modeling of Munitions in the Underwater Environment. Tech. rep. (available: http://www.dtic.mil/get-tr-doc/pdf?AD=ADA627132, accessed 11/8/2017).

Cataño-Lopera, Y. A., and Garcia, M. H. 2006. Burial of short cylinders induced by scour under combined waves and currents. *J. Waterway, Port, Coastal, Ocean Eng.*, ASCE, 132 (6), 439–449.

Cataño-Lopera, Y., García, M. H., 2007. Geometry of Scour Hole around, and Influence of the Angle of Attack on the Burial of Short Cylinders under Combined Flows. *Ocean Engineering*, 34, pp. 856-869.

Cataño-Lopera Y. A., Landry B., Abad J. D., García M. H. 2013. Experimental and numerical study of the flow structure around two partially buried objects on a deformed bed. *Journal of Hydraulic Engineering.* 139 (3), 269–283.

Cataño-Lopera Y. A., Landry B., García M. H. 2017. Unstable flow structure around partially buried objects on a simulated river bed. *Journal of Hydroinformatics*, 19 (1) 31-46.

Cokgor, S. 2002. Hydrodynamic forces on a partly buried cylinder exposed to combined waves and current. *Ocean Engineering*, 29(7), 753-768.

Coleman, N. L. 1967. A theoretical and experimental study of drag and lift forces acting on a sphere resting on a hypothetical stream bed. Proceedings of the Twelfth Congress, International Association for Hydraulic Research, Fort Collins Colorado, 185–192.

Demir, S., Garcia, M.H., 2007. Experimental Studies on Burial of Finite-Length Cylinders under Oscillatory Flow. *J. Waterway, Port, Coastal, Ocean Eng.*, ASCE, 133, No. 2, 117-124.

Edwards, M. H., Shjegstad, S. M., Wilkens, R., King, J. C., Carton, G., Bala, D., Bingham, B., Bissonnette, M. C., Briggs, C., Bruso, N. S., Camilli, R., Cremer, M., Davis, R. B., DeCarlo, E. H., DuVal, C., Fornari, D. J., Kaneakua-Pia, I., Kelley, C. D., Koide, S., Mah, C. L., Kerby, T., Kurras, G. J., Rognstad, M. R., Sheild, L., Silva, J., Wellington, B., Woerkom, M. V., 2016. The Hawaii undersea Military Munitions Assessment. Deep Sea Research Part II: Topical Studies in

Oceanography 128, 4 – 13, Chemical Munitions Dumped at Sea. (URL http://www.sciencedirect.com/science/article/pii/S0967064516300844, accessed 11/8/2017).

Fenton, J., Abbot, J. E. 1977. Initial Movement of Grains on a Stream Bed: The Effect of Relative Protrusions, Proceeding of the Royal Society of London, Series A-352, 523–537.

Friedrichs, C.T., 2013. Simple Parameterized Models for Predicting Mobility, Burial and Re-Exposure of Underwater Munitions, MR-2224, In-Progress Review Meeting for the Munitions Response Program Area 12 Feb 2013. URL http://www.vims.edu/~cfried/presentations/2013/ Friedrichs_Feb2013_SERDP.ppt, (Also webinar presentation "Concepts and Forces Important in Burial, Initiation of Motion, and Continued Motion of Underwater Munitions" slide 20, URL https://www.serdp-estcp.org/Tools-and-Training/Webinar-Series/05-07-2015), accessed 4/24/2018.

Friedrichs, C. T., Rennie, S. E., Brandt, A. 2016. Self-burial of objects on sandy beds by scour: A synthesis of observations, In: Scour and Erosion, Harris, Whitehouse and Moxon (Eds), ISBN 978-1-138-02979.

Garcia, M. H. (Ed.). 2008. Sedimentation engineering: processes, measurements, modeling, and practice. Manual of engineering Practice No 110, American Society of Civil Engineers, Reston, Virginia.

Gioia, G., Chakraborty, P., 2006. Turbulent Friction in Rough Pipes and the Energy Spectrum of the Phenomenological Theory, *Phys. Rev. Lett.*, American Physical Society, 96(4), pp 044502-1-4.

Ikeda, S. 1982. Incipient Motion of Sand Particles on Side Slopes, *Journal of the Hydraulics Division*, ASCE, 108 (1), 95–114.

Isbash, S. V., 1936. Construction of dams by depositing rock in running water, Transactions, Second Congress on Large Dams, Washington, D.C. USA.

Iwagaki, Y. 1956. Fundamental study on critical tractive force. Proceedings, Japan Society of Civil Engineering, 41, 1–21.

James, C. S. 1990. Prediction of entrainment conditions for nonuniform, noncohesive sediments. *Journal of Hydraulic Research*, *28*(1), 25-41.

Jenkins, S., D'Spain, G., Wasyl, J., 2012. Vortex lattice UXO mobility model for reef-type range environments. Tech. rep., DTIC Document.

Jonsson, I. G. 1980. A new approach to oscillatory rough turbulent boundary layers. *Ocean Engineering*, *7*(1), 109-152.

Kirchner, J. W., Dietrich, W. E., Iseya, F., and Ikeda, H. 1990. The variability of critical shear stress, friction angle, and grain protrusion in water- worked sediments. *Sedimentology*, ***37*** (4), 647-672.

Komar, P. D. 1996. Entrainment of sediments from deposits of mixed grain sized and densities" in "Advances in fluvial dynamics and stratigraphy, edited by Carling P.A and Dawson M.R., pp 127-182, Wiley, New York.

Komar, P. D., Li, Z. 1988. Applications of grain-pivoting and sliding analyses to selective entrainment of gravel and to flow-competence evaluations, *Sedimentology*, **35**, 681-695.

Komar, P. D., Li, Z. 1986. Pivoting analyses of the selective entrainment of sediments by shape and size with application to gravel threshold. *Sedimentology*, ***33*** (3), 425-436.

Komar, P.D., Wang, C. 1984. Processes of selective grain transport and the formation of placers on beaches, *Journal of Geology*, 92, 637-655.

Li, Z., Komar, P. D. 1986. Laboratory measurements of pivoting angles for applications to selective entrainment of gravel in a current. *Sedimentology*, *33*(3), 413-423.

Li, Z and Komar, P.D. 1992. Longshore grain sorting and beach placer formation adjacent to the Columbia River, *Journal of Sedimentary Petrology*, 62, 429-441.

Miller, R. L., Byrne, R. J. 1966. The Angle of repose for a single grain on a fixed rough bed. *Sedimentology*, 6, 303–314.

Möller, N., 2014. Effects of boundary roughness on turbulence in uniform open channel flow. MS thesis. University of Illinois at Urbana-Champaign.

Niell, C. R. 1967. Mean-velocity criterion for scour of coarse uniform bed material, International Association of Hydraulic Research, 12th congress, 3, 46-55.

Neill, C. R. 1968. Note on Initial Movement of Coarse Uniform Material. *Journal of Hydraulic Research*, IAHR, 6(2), 157–184.

Neill, C. R., Yalin. M. S. 1969. Qualitative definition of beginning of bed movement. *Journal of the Hydraulics Division*, ASCE, 95 (1), 585–587.

Niño, Y., Lopez, F., Garcia, M. 2003. Threshold for particle entrainment into suspension. *Sedimentology*, 50 (2), 247-263.

Raffel, M., Willert, C., Wereley, S., Kompenhans, J. 1998. Particle Image Velocimetry. Berlin.

Rennie S. E., Brandt A., 2015. Underwater Munitions Expert System to Predict Mobility and Burial. SERDP Project MR-2227. Interim Report. (available: http://www.dtic.mil/get-tr-doc/pdf?AD=AD1000200, accessed 11/08/2017).

Rennie S. E., Brandt A., Friedrichs C.T. 2017. Initiation of motion and scour burial of objects uderwater. *Ocean Engineering*, 131, 282-294.

Richardson, M. D., Traykovski, P., 2002. Real-time observations of mine burial at the Martha's Vineyard Coastal Observatory, Proc. 5th Int. Symp. Technol. Mine Problem.

Rubey, W.W. 1938. The force required to move particles on a stream bed, Geological Survey Professional Paper, 189-E, 121-141.

Sarpkaya, T. 2010. Wave Forces on Offshore Structures. Cambridge University Press.

SERDP, 2010. Munitions in the Underwater Environment: State of the Science and Knowledge Gaps, white paper. June.

Shields, A. 1936. Anwendung der Ahnlichkeitsmechanik und der Turbulenzforschung auf die Geschiebebewegung. Mitt. Preuss. Vers. Anst. Wasserb. Schiffb 26, 26 pp. (translated by W. P. Ott and J. C. van Uchelen, U.S. Department of Agriculture, Soil Conservation Service Coop Laboratory, California Institute of Technology).

Sumer, B. M., Fredøse, J. 2001. Scour around pile in combined waves and current. *Journal of Hydraulic Engineering*, ASCE, 127(5), 2001, 403-411.

Sumer, B. M., Fredøse, J. 2006. Hydrodynamics around Cylindrical Structures. World Scientific.

Traykovski, P., Austin, T., 2017. Continuous monitoring of mobility, burial and re-exposure of underwater munitions in energetic near-shore environments. Tech. rep., DTIC Document

Traykovski, P., Richardson, M. D., Mayer, L. A., Irish, J. D., 2007. Mine burial experiments at the Martha's Vineyard Coastal Observatory. *IEEE Journal of Oceanic Engineering*, 32 (1), 150–166.

Voropayev, S. I., Roney, J., Fernando, H.J.S., G.B., Boyer, D.L., Houston, W.N., 1998. The motion of large bottom particles (cobbles) in a wave-induced oscillatory flow. *Coastal Engineering*, 34, 197-219.

Voropayev, S. I., Cense, A. W., McEachern, G. B., Boyer, D. L., Fernando, H. J. S., 1999. Dynamics of sand ripples and burial/scouring of cobbles in oscillatory flow. *Applied Ocean Research*, 21 (5), 249-261.

Voropayev, S. I., Testik, F. Y., Fernando, H. S. J., Boyer, D. L., 2003. Burial and scour around short cylinder under progressive shoaling waves. *Coastal Engineering*, 30, 1647-1667.

Wu, H. Zuniga Zamalloa, C. C., Landy B. J., García, M. H., 2017. Experimental comparison of initiation of motion for submerged objects resting on fixed permeable and impermeable beds. (manuscript in preparation).

White, C. M. 1940. The equilibrium of grains on the bed of a stream, Proceedings of the Royal Society of London, Series A. 174, 332-338.

Wiberg, P. L., Smith, J. D. 1987. Calculations of the critical shear stress for motion of uniform and heterogeneous sediments. *Water Resources Research*, 23 (8), 1471-1480.

Wilkens, R. H., Richardson, M. D., 2007. Mine Burial Prediction: A Short History and Introduction. *IEEE Journal of Oceanic Engineering*, 32 (1), 3-9.

Yalin, M. S. 1972. Mechanics of sediment transport. Pergamon Press, 2nd Ed, New York.

Yalin, M. S., Karahan, E. 1979. Inception of sediment transport. *Journal of Hydraulic Engineering*, ASCE, 105 (HY11), 1433–1443.

Appendix A: Experimental Facilitates

Description of WHOI Flume:

The WHOI flume is a 17.3 m long, 0.6 m wide, and 0.3 m deep fiberglass flume with Plexiglas windows (see Figure 27). The flume has a smooth polyvinyl chloride (PVC) false bottom. Hydraulic pistons allow for adjustment of the bed slope, with the fulcrum located near the downstream end of the flume. A small tank at the downstream end of the flume acts as a reservoir and establishes tail-water conditions. Water is recirculated in the flume via an inverter-controlled variable speed pump that withdraws water from the tail-water tank and pumps it to the upstream end of the flume. Upon re-entering the flume, the flow first passes through a spherical array to dampen water-surface oscillations and reduce turbulence and then passes through a cylindrical array flow straightener to help transition the flow to a more uniform distribution. A McCrometer Ultra Mag® Flow meter (accuracy of ±0.5% of actual flow) located in the center section of the recirculation pipe allows the flow rate to be read off a digital display. A point gauge, line laser, and video camera were mounted over the experimental section via portable aluminum frame spanning the width of the flume (refer to Figure 6).

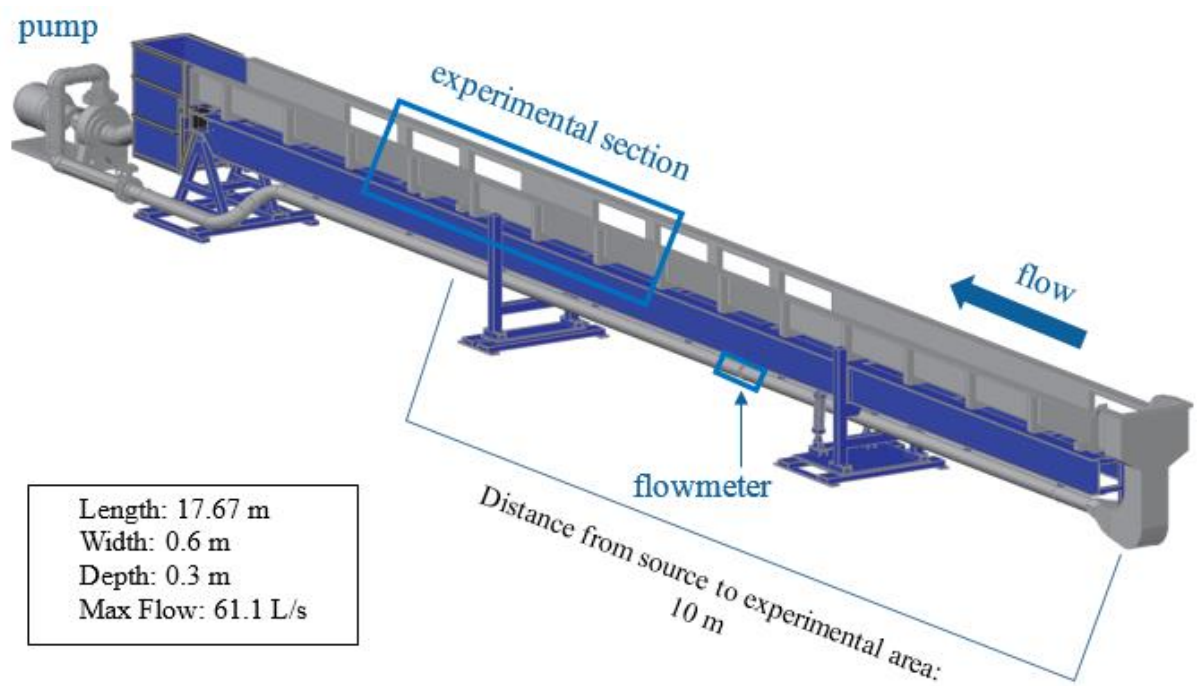

Figure 27: WHOI flume used for unidirectional flow initiation of motion experiments.

Description of the STF:

The STF is an elevated flume that is 19.5 m long, 0.9 m wide, and 0.6 m deep with Plexiglas windows and a painted, rough steel bottom (refer to Figure 28, Figure 29, and Figure 30). Based on flow velocity profiles using a Nortek Vectrino and a log-law fit of the data, the roughness, ks, is roughly 0.047 mm. The flume was temporarily narrowed to 0.55 m wide with cinder blocks and a plastic waterproof covering for these experiments (see Figure 29). A sediment trap at the tail of the flume allows for the collection of any transported material (e.g., munitions) before it gets to the recirculation system. Two screw jacks positioned on either side of a central fulcrum can be used to vary the flume's slope between 0% and 10%. Water is supplied to the flume from the laboratory head tank, and water depth in the flume is controlled by raising or lowering a hydraulic gate at the downstream end of the flume. Flow is controlled by opening and closing the supply valve and is measured with an Ultra Mag ® flowmeter (accuracy of ±0.5% of actual flow). An aluminum frame spanning the width of the flume allowed for a point gauge, line laser, and video camera to be mounted for use in the initiation of motion experiments (refer to Figure 29).

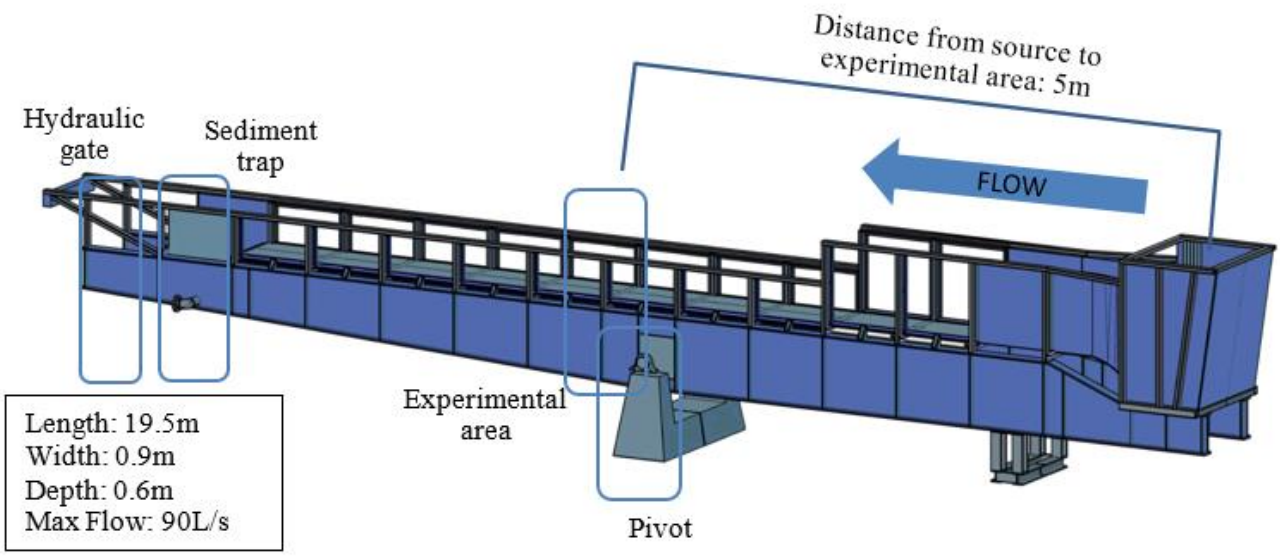

Figure 28: The Small Tilting Flume (STF) was used to continue unidirectional flow initiation of motion experiments from the WHOI.

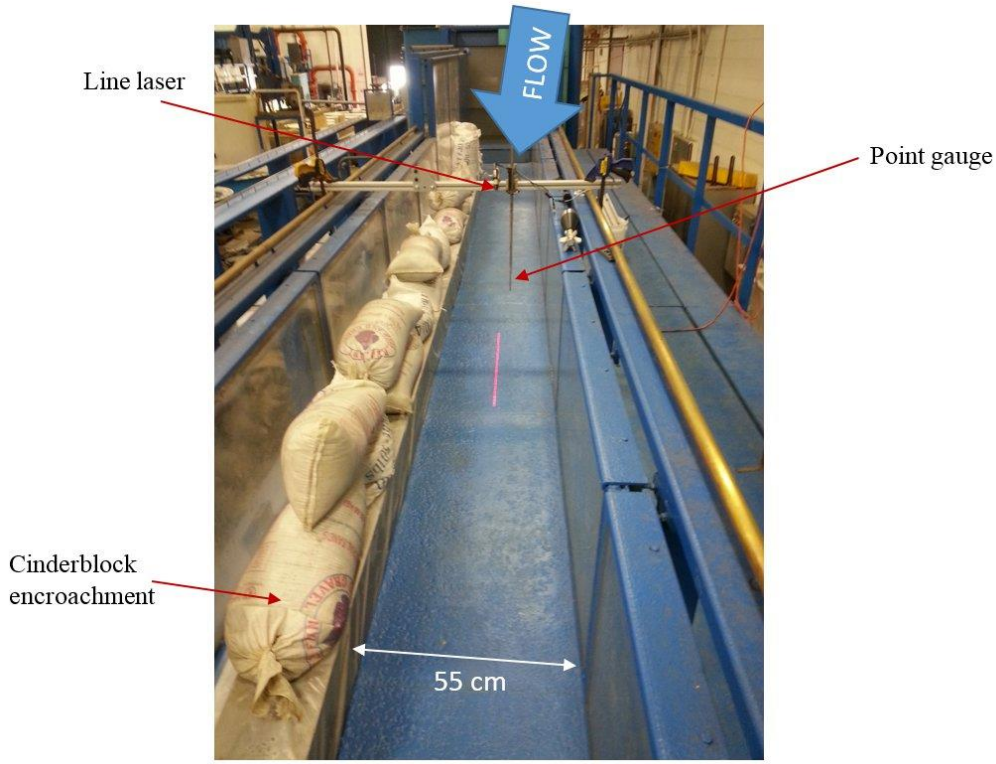

Figure 29: Overview of aluminum frame spanning the width of the Small Tilting Flume (STF) with attached point gauge and line laser. Experiments located 5 m from the upstream of the flume.

Figure 30: The STF bed is made of rough (pitted), painted steel.

Description of Cavitation Tunnel (CT):

The Cavitation Tunnel (CT) provides unidirectional flow with a flow velocity as high as 9 m/s, which cannot be achieved in the other flume. With its ability of high flow rates, the Cavitation Tunnel was used to test the threshold for initiation of motion of the munitions at small angle of attack. The 1.2 m long test section of the Cavitation Tunnel is 0.305 m in width and height. A PVC bed was installed in the tunnel.

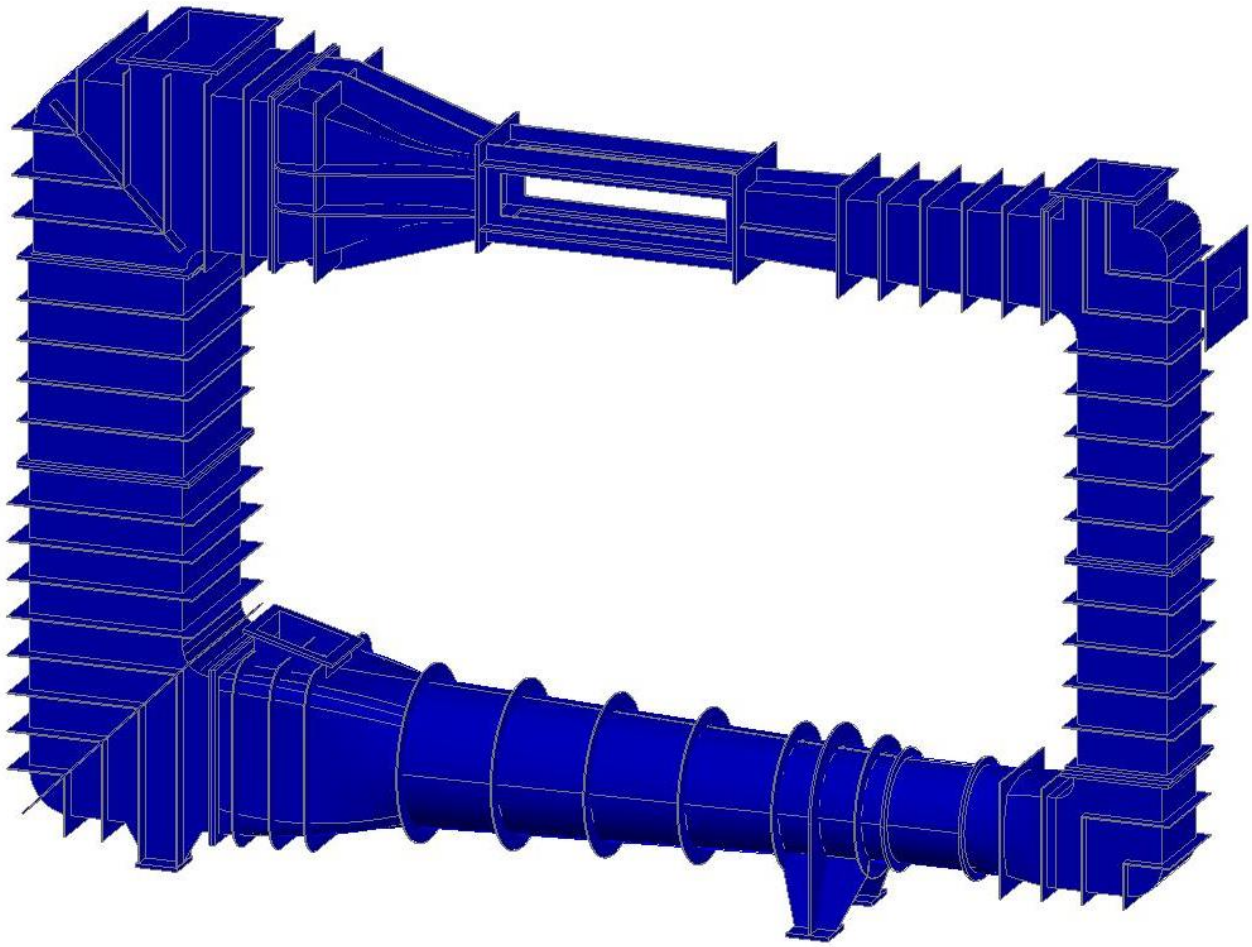

Figure 31: The Cavitation Tunnel used for unidirectional high flow rates to test the threshold for initiation of motion of munitions at small angle of attack.

Description of the Illinois Hyporheic Flow Facility:

The Illinois Hyporheic Flow Facility (IHFF) is a recirculating open-channel water flume that houses a fixed packed bed as shown in Figure 32. The fixed packed bed consists of uniform size plastic spheres that have a diameter of 0.04 m and are arranged in a cubic packing. The test region in the flume is 4.8 m long and has a 0° slope. The rectangular cross section in the test region is 0.35 m wide and 0.3 m high. The munition is fixed on a non-porous sheet that is 0.4 m long and 0.26 m wide and placed above the permeable bed during the experiments. The munition is aligned with the flow ($\theta = 0$). A transparent visor was placed at the water surface to prevent the surface waves from interfering with the laser sheet.

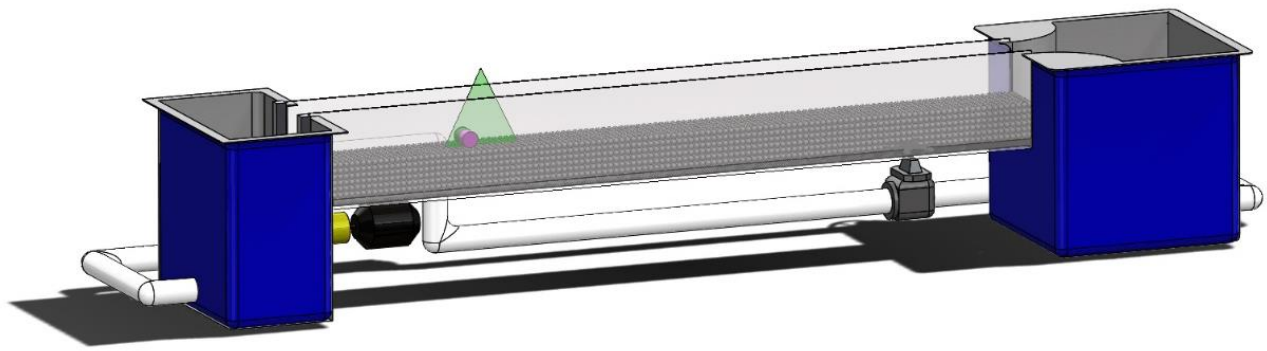

Figure 32: Sketch of the Illinois Hyporheic Flow Facility

Description of Large Oscillatory Sediment Water Tunnel (LOWST):

The oscillatory flow experiments were conducted in the Large Oscillatory Water-Sediment Tunnel (LOWST) (Figure 33), which is a U-shaped pipe that is 12 m long, 0.8 m wide, and 0.6 m high in the interior of the test section with a hard PVC substrate. Three pistons on one side of the U-shaped tunnel drive the flow while the other end of the tunnel is a free well. In addition to the pistons that generate oscillatory flows, the LOWST is also equipped with two pumps that can superimpose an unidirectional flow for up to 0.5 m/s.

In addition to the PVC substrate condition, some tests were also performed on a gravel bed. The roughness of the gravel bed was estimated to be 35 mm. The PVC bed was covered with gravels for 2.5 m upstream and downstream of the test section.

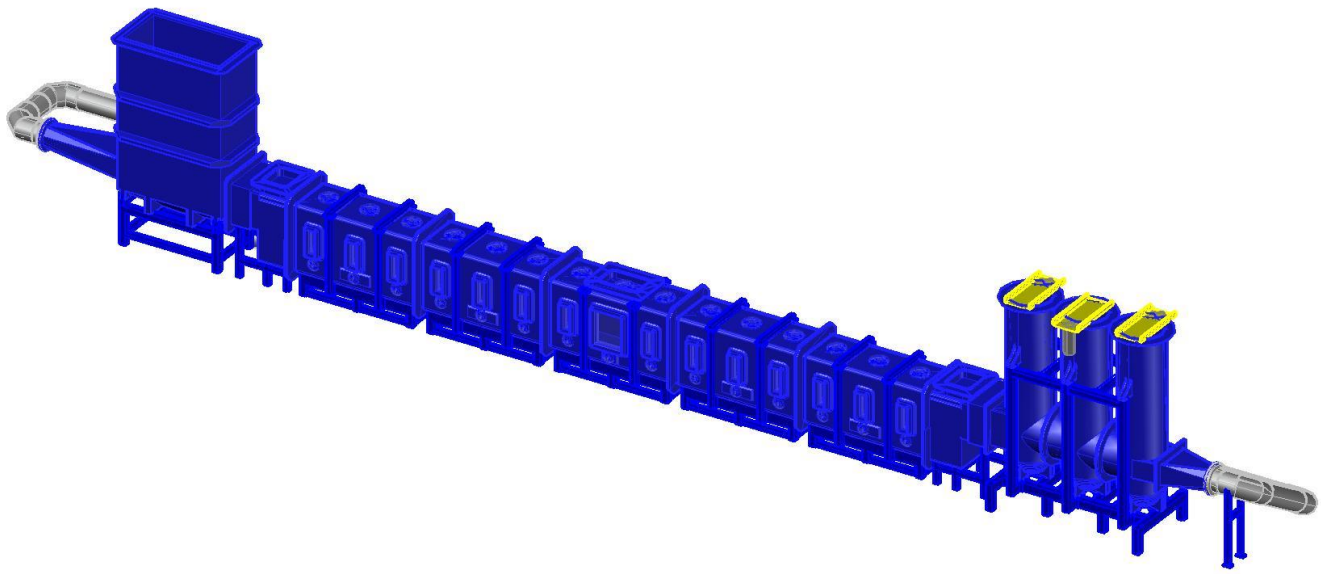

Figure 33: Large Oscillatory Sediment Water Tunnel (LOWST) used for initiation of motion experiments in oscillatory flows.

Description of the Small Oscillatory Tunnel:

The Small Oscillatory Tunnel (SOT) is a U-shaped tube that has a length of 3.9 m, a height of 0.25 m, and a width of 0.20 m in the testing section and is shown in Figure 34. A piston located at one end of the U-tube is used to drive the flow toward the opposite end of the tunnel, which is open to the air. Gravity and/or negative pressure at the face of the piston cause the flow to change direction on the reverse stroke, setting up an oscillatory flow condition. Table 8 lists the operating conditions that were run in this set of experiments. The period ranged from 2 to 5 seconds, while the half stroke of the piston is between 0.02 m and 0.1 m.

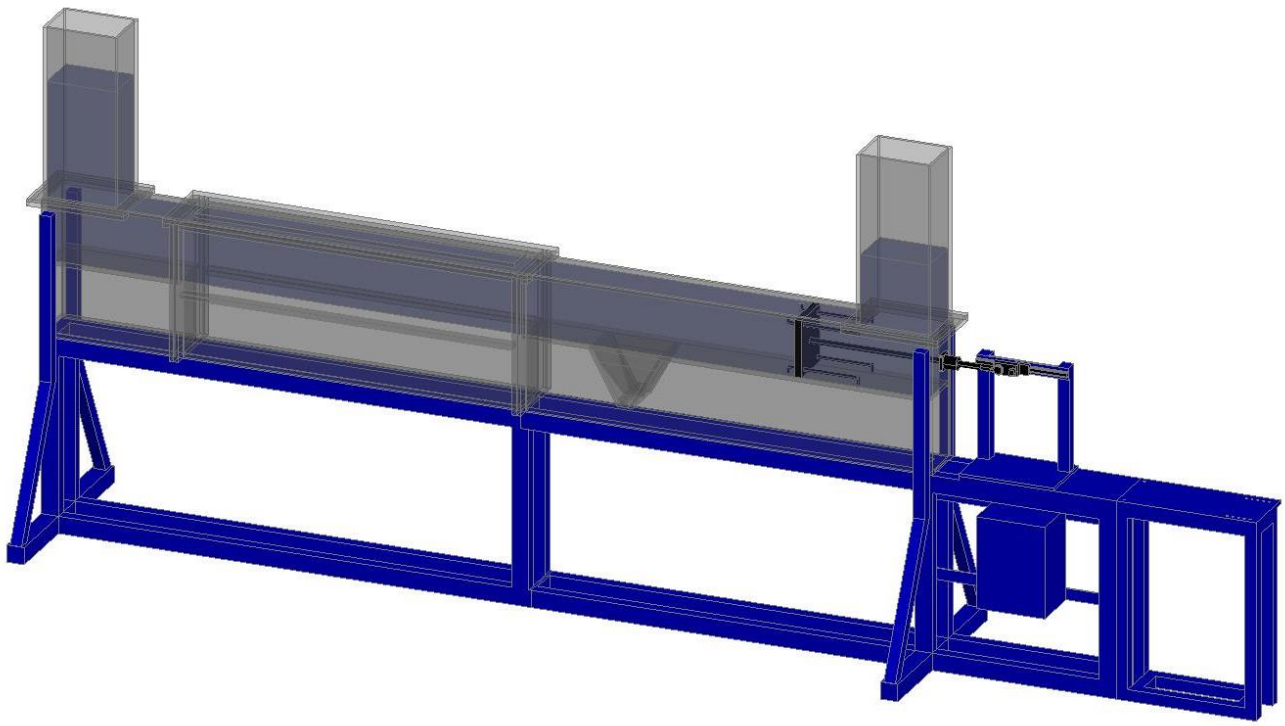

Figure 34: Sketch of the Small Oscillatory Tunnel, side view.

Appendix B: Additional Details for Angle of Attack Experiments

Initiation of Motion Trials in Unidirectional Flows

Substrate	Flume (and slope)	Surrogate Munition Shape	Surrogate Munition Type	Manufacturer	Trials per Angle										Trial Subtotals
					0°	10°	20°	30°	40°	50°	60°	70°	80°	90°	
PVC	WHOI Flume (horiz. bed)	Cartridge	25-mm	NRL	*	1	1	1	1	1	1	1	1	1	10
				UIUC	0	0	0	1	0	0	1	0	0	1	3
			35-mm	NRL	-	-	-	1	-	-	1	-	-	1	10
				UIUC	*	1	3	1	1	1	1	3	1	1	14
			81-mm	NRL	-	-	-	-	-	-	-	-	-	-	10
				UIUC	*	1	1	1	1	1	1	1	1	1	10
		Warhead	25-mm	NRL	*	1	1	1	1	1	1	1	1	1	10
				UIUC	0	0	0	0	0	0	0	0	0	0	0
			35-mm	NRL	-	-	-	-	-	-	-	-	-	-	10
				UIUC	*	1	1	1	1	1	1	1	3	1	12
			81-mm (no fin)	NRL	-	-	-	-	-	-	-	-	-	-	10
				UIUC	0	3	4	3	5	4	3	3	4	5	34
Painted Pitted Steel	STF (Slope=0.4°)	Cartridge	25-mm	UIUC	*	2	0	4	0	0	4	0	0	0	11
			35-mm	UIUC	*	2	0	4	0	0	4	0	0	0	11
			81-mm	UIUC	*	2	0	4	0	0	3	0	0	0	10
		Warhead	25-mm	UIUC	*	0	0	*	0	0	*	0	0	*	4
			35-mm	UIUC	*	0	0	*	0	0	*	0	0	*	4
			81-mm (no fin)	UIUC	*	0	0	*	0	0	*	0	0	*	4
Painted Pitted Steel	STF (horiz. bed)	Cartridge	25-mm	UIUC	*	3	0	3	0	0	3	0	0	2	12
			35-mm	UIUC	*	3	0	4	2	0	2	0	0	3	15
			81-mm	UIUC	*	2	0	2	4	3	3	1	0	2	18
		Warhead	25-mm	UIUC	*	0	0	*	0	0	*	0	0	*	4
			35-mm	UIUC	*	0	0	*	0	0	*	0	0	*	4
			81-mm	UIUC	*	0	0	*	0	0	*	0	0	*	4
														Total Trials:	234

#	Data available: number represents trials performed
0	Trial not performed at this time
*	Motion could not be achieved on this surface under specified conditions
-	NRL Munitions no longer available at Ven Te Chow Lab

Table 4: Unidirectional flow experimental initiation of motion matrix illustrating the various trials for each experimental condition.

Appendix C: Table of Experimental Results

Table 5: Unidirectional Experimental Data. First column (#): the number of experiment, second column: the flume used for the experiment, third column: the nominal diameter of the examined munition or object, fourth column: the angle of attack, fifth column: the slope of the flume, sixth column: the projected area of the munition of object, seventh column (ρ_m): the munition density, eighth column (ν): the kinematic viscosity of water, ninth column (ρ_w); the water density, tenth column (H_c): the characteristic depth of the flow (water depth for open channel flows and half the channel height for channel flows), eleventh column (U): critical velocity for initiation of motion, twelfth column (T): the period of the flow for the case of oscillatory flows.

#	Flume	Nominal Size and Type	θ [degree]	Slope %	Projected area [m^2]	ρ_m [kg/m^3]	ν [m^2/sec]	ρ_w [kg/m^3]	H_c [m]	U [m/s]	T [sec]
1	CT	20 mm shell	0	0	0.00067	2432.20	1.02E-06	998.23	0.15	1.81	-
2	CT	20 mm shell	0	0	0.00067	2432.20	1.02E-06	998.23	0.15	1.79	-
3	WHOI	20 mm shell	10	0	0.001148	2683.53	9.95E-07	998.02	0.11	0.21	-
4	WHOI	20 mm shell	20	0	0.001734	2683.53	9.95E-07	998.02	0.11	0.14	-
5	WHOI	20 mm shell	30	0	0.002299	2683.53	9.95E-07	998.02	0.11	0.12	-
6	WHOI	20 mm shell	30	0	0.002299	2683.53	1.03E-06	998.34	0.08	0.13	-
7	WHOI	20 mm shell	40	0	0.002812	2432.20	9.95E-07	998.02	0.11	0.12	-
8	WHOI	20 mm shell	50	0	0.003237	2683.53	9.95E-07	998.02	0.12	0.09	-
9	WHOI	20 mm shell	60	0	0.003566	2683.53	9.95E-07	998.02	0.12	0.09	-
10	WHOI	20 mm shell	60	0	0.003566	2432.20	1.03E-06	998.34	0.09	0.1	-
11	WHOI	20 mm shell	70	0	0.003605	2683.53	9.95E-07	998.02	0.12	0.09	-
12	WHOI	20 mm shell	80	0	0.003905	2683.53	9.95E-07	998.02	0.12	0.09	-
13	WHOI	20 mm shell	90	0	0.003901	2683.53	9.95E-07	998.02	0.12	0.11	-
14	WHOI	20 mm shell	90	0	0.003901	2432.20	1.03E-06	998.34	0.09	0.1	-

Table 5 continued…

#	Flume	Nominal Size and Type	θ [degree]	Slope %	Projected area [m^2]	ρ_m [kg/m^3]	ν [m^2/sec]	ρ_w [kg/m^3]	H_c [m]	U [m/s]	T [sec]
15	WHOI	20 mm shell	120	0	0.003566	2432.20	1.03E-06	998.34	0.15	0.06	-
16	WHOI	20 mm shell	140	0	0.002812	2432.20	1.03E-06	998.34	0.15	0.06	-
17	WHOI	20 mm shell	160	0	0.001734	2432.20	1.03E-06	998.34	0.14	0.07	-
18	WHOI	20 mm shell	180	0	0.00067	2432.20	1.02E-06	998.25	0.13	0.46	-
19	CAV	25 mm shell	0	0	0.001112	2106.33	1.02E-06	998.23	0.15	1.7	-
20	CAV	25 mm shell	0	0	0.001112	2106.33	1.02E-06	998.23	0.15	1.75	-
21	WHOI	25 mm shell	10	0	0.001897	2106.33	1.02E-06	998.23	0.11	0.16	-
22	WHOI	25 mm shell	20	0	0.002852	2106.33	1.02E-06	998.23	0.11	0.13	-
23	WHOI	25 mm shell	20	0	0.002852	2106.33	1.02E-06	998.23	0.11	0.15	-
24	WHOI	25 mm shell	20	0	0.002852	2106.33	1.02E-06	998.23	0.11	0.13	-
25	WHOI	25 mm shell	30	0	0.003783	2106.33	1.02E-06	998.23	0.11	0.11	-
26	WHOI	25 mm shell	30	0	0.003783	2374.73	1.02E-06	998.25	0.08	0.16	-
27	WHOI	25 mm shell	40	0	0.004621	2106.33	1.02E-06	998.23	0.11	0.08	-
28	WHOI	25 mm shell	50	0	0.005328	2106.33	1.02E-06	998.23	0.11	0.08	-
29	WHOI	25 mm shell	60	0	0.005879	2106.33	1.02E-06	998.23	0.12	0.08	-
30	WHOI	25 mm shell	60	0	0.005879	2374.73	1.02E-06	998.25	0.08	0.15	-

Table 5 continued…

#	Flume	Nominal Size and Type	θ [degree]	Slope %	Projected area [m^2]	ρ_m [kg/m^3]	ν [m^2/sec]	ρ_w [kg/m^3]	H_c [m]	U [m/s]	T [sec]
31	WHOI	25 mm shell	70	0	0.006242	2106.33	1.02E-06	998.23	0.12	0.07	-
32	WHOI	25 mm shell	70	0	0.006242	2106.33	1.02E-06	998.23	0.12	0.08	-
33	WHOI	25 mm shell	70	0	0.006242	2106.33	1.02E-06	998.23	0.12	0.07	-
34	WHOI	25 mm shell	80	0	0.006441	2106.33	1.02E-06	998.23	0.12	0.08	-
35	WHOI	25 mm shell	90	0	0.006431	2106.33	1.02E-06	998.23	0.12	0.08	-
36	WHOI	25 mm shell	90	0	0.006431	2374.73	1.02E-06	998.25	0.08	0.13	-
37	WHOI	25 mm shell	140	0	0.004621	2106.33	1.04E-06	998.38	0.14	0.16	-
38	WHOI	25 mm shell	160	0	0.002852	2106.33	1.04E-06	998.38	0.14	0.11	-
39	WHOI	25 mm shell	180	0	0.001112	2106.33	1.04E-06	998.38	0.13	0.49	-
40	CT	81 mm mortar	0	0	0.005002	3293.63	1.02E-06	998.23	0.15	2.4	-
41	CT	81 mm mortar	0	0	0.005002	3293.63	1.02E-06	998.23	0.15	2.33	-
42	CT	81 mm mortar	0	0	0.005002	3293.63	1.02E-06	998.23	0.15	2.4	-
43	WHOI	81 mm mortar	10	0	0.007768	3293.63	1.07E-06	998.62	0.11	0.45	-
44	WHOI	81 mm mortar	20	0	0.011942	3293.63	1.07E-06	998.62	0.11	0.31	-
45	WHOI	81 mm mortar	30	0	0.016071	3293.63	1.07E-06	998.62	0.11	0.24	-
46	WHOI	81 mm mortar	40	0	0.019658	3293.63	1.07E-06	998.62	0.11	0.17	-
47	WHOI	81 mm mortar	50	0	0.022684	3293.63	1.07E-06	998.62	0.11	0.17	-

Table 5 continued…

#	Flume	Nominal Size and Type	θ [degree]	Slope %	Projected area [m^2]	ρ_m [kg/m^3]	ν [m^2/sec]	ρ_w [kg/m^3]	H_c [m]	U [m/s]	T [sec]
48	WHOI	81 mm mortar	60	0	0.025103	3293.63	1.07E-06	998.62	0.11	0.17	-
49	WHOI	81 mm mortar	70	0	0.0268	3293.63	1.07E-06	998.62	0.11	0.17	-
50	WHOI	81 mm mortar	80	0	0.027723	3293.63	1.07E-06	998.62	0.11	0.15	-
51	WHOI	81 mm mortar	90	0	0.027781	3293.63	1.07E-06	998.62	0.11	0.15	-
52	WHOI	81 mm mortar	120	0	0.025103	3293.63	1.02E-06	998.23	0.14	0.2	-
53	WHOI	81 mm mortar	140	0	0.019658	3293.63	1.02E-06	998.23	0.14	0.24	-
54	WHOI	81 mm mortar	160	0	0.011942	3293.63	1.02E-06	998.23	0.14	0.41	-
55	WHOI	81 mm mortar	180	0	0.005002	3293.63	1.07E-06	998.64	0.14	0.41	-
56	CT	20 mm projectile	0	0	0.000308	8219.20	1.02E-06	998.23	0.15	2.35	
57	WHOI	20 mm projectile	10	0	0.000407	8296.75	1.02E-06	998.25	0.08	0.29	-
58	WHOI	20 mm projectile	20	0	0.000516	8296.75	1.02E-06	998.25	0.08	0.32	-
59	WHOI	20 mm projectile	30	0	0.000643	8296.75	1.02E-06	998.25	0.08	0.27	-
60	WHOI	20 mm projectile	40	0	0.000757	8296.75	1.02E-06	998.25	0.08	0.25	-
61	WHOI	20 mm projectile	50	0	0.000853	8296.75	1.02E-06	998.25	0.08	0.23	-
62	WHOI	20 mm projectile	60	0	0.000922	8296.75	1.02E-06	998.25	0.08	0.23	-
63	WHOI	20 mm projectile	70	0	0.000968	8296.75	1.02E-06	998.25	0.08	0.19	-

Table 5 continued…

#	Flume	Nominal Size and Type	θ [degree]	Slope %	Projected area [m^2]	ρ_m [kg/m^3]	ν [m^2/sec]	ρ_w [kg/m^3]	H_c [m]	U [m/s]	T [sec]
64	WHOI	20 mm projectile	80	0	0.000985	8296.75	1.13E-06	999.02	0.09	0.23	-
65	WHOI	20 mm projectile	90	0	0.000972	8296.75	1.13E-06	999.02	0.08	0.19	-
66	WHOI	20 mm projectile	110	0	0.000968	8219.20	1.02E-06	998.23	0.14	0.43	-
67	WHOI	20 mm projectile	110	0	0.000968	8219.20	1.02E-06	998.23	0.13	0.49	-
68	WHOI	20 mm projectile	135	0	0.000808	8219.20	1.02E-06	998.23	0.14	0.22	-
69	WHOI	20 mm projectile	135	0	0.000808	8219.20	1.02E-06	998.23	0.14	0.22	-
70	WHOI	20 mm projectile	135	0	0.000808	8219.20	1.02E-06	998.23	0.14	0.26	-
71	WHOI	20 mm projectile	135	0	0.000808	8219.20	1.02E-06	998.23	0.14	0.31	-
72	WHOI	20 mm projectile	150	0	0.000643	8219.20	1.03E-06	998.32	0.13	0.4	-
73	WHOI	20 mm projectile	170	0	0.000407	8219.20	1.03E-06	998.32	0.13	0.56	-
74	WHOI	20 mm projectile	180	0	0.000308	8219.20	1.01E-06	998.15	0.13	0.52	-
75	WHOI	20 mm projectile	180	0	0.000308	8219.20	1.01E-06	998.15	0.13	0.61	-
76	WHOI	20 mm projectile	180	0	0.000308	8219.20	1.01E-06	998.15	0.13	0.61	-
77	WHOI	25 mm projectile	10	0	0.000604	7845.87	1.05E-06	998.47	0.08	0.35	-
78	WHOI	25 mm projectile	20	0	0.000763	7845.87	1.05E-06	998.47	0.08	0.27	-
79	WHOI	25 mm projectile	30	0	0.000962	7845.87	1.05E-06	998.47	0.09	0.21	-

Table 5 continued…

#	Flume	Nominal Size and Type	θ [degree]	Slope %	Projected area [m^2]	ρ_m [kg/m^3]	ν [m^2/sec]	ρ_w [kg/m^3]	H_c [m]	U [m/s]	T [sec]
80	WHOI	25 mm projectile	40	0	0.001142	7845.87	1.05E-06	998.47	0.09	0.23	-
81	WHOI	25 mm projectile	50	0	0.001296	7845.87	1.05E-06	998.47	0.09	0.15	-
82	WHOI	25 mm projectile	60	0	0.001411	7845.87	1.05E-06	998.47	0.09	0.23	-
83	WHOI	25 mm projectile	70	0	0.001484	7845.87	1.05E-06	998.47	0.09	0.26	-
84	WHOI	25 mm projectile	80	0	0.001514	7845.87	1.05E-06	998.47	0.09	0.21	-
85	WHOI	25 mm projectile	80	0	0.001514	7845.87	1.05E-06	998.47	0.09	0.23	-
86	WHOI	25 mm projectile	80	0	0.001514	7845.87	1.05E-06	998.47	0.09	0.23	-
87	WHOI	25 mm projectile	90	0	0.001501	7845.87	1.05E-06	998.47	0.08	0.3	-
88	WHOI	25 mm projectile	100	0	0.001514	7845.87	1.02E-06	998.27	0.14	0.27	-
89	WHOI	25 mm projectile	100	0	0.001514	7845.87	1.02E-06	998.27	0.14	0.27	-
90	WHOI	25 mm projectile	110	0	0.001484	7845.87	0.000001	998.11	0.14	0.26	-
91	WHOI	25 mm projectile	110	0	0.001484	7845.87	0.000001	998.11	0.14	0.24	-
92	WHOI	25 mm projectile	110	0	0.001484	7845.87	0.000001	998.11	0.14	0.18	-
93	WHOI	25 mm projectile	110	0	0.001484	7845.87	0.000001	998.11	0.13	0.34	-
94	WHOI	25 mm projectile	110	0	0.001484	7845.87	1.00E-06	998.11	0.13	0.42	-
95	WHOI	25 mm projectile	110	0	0.001484	7845.87	1.02E-06	998.23	0.14	0.38	-
96	WHOI	25 mm projectile	120	0	0.001411	7845.87	1.02E-06	998.23	0.13	0.19	-

Table 5 continued…

#	Flume	Nominal Size and Type	θ [degree]	Slope %	Projected area [m^2]	ρ_m [kg/m^3]	ν [m^2/sec]	ρ_w [kg/m^3]	H_c [m]	U [m/s]	T [sec]
97	WHOI	25 mm projectile	120	0	0.001411	7845.87	1.02E-06	998.23	0.14	0.16	-
98	WHOI	25 mm projectile	120	0	0.001411	7845.87	1.02E-06	998.23	0.13	0.46	-
99	WHOI	25 mm projectile	120	0	0.001411	7845.87	1.02E-06	998.23	0.13	0.16	-
100	WHOI	25 mm projectile	135	0	0.001235	7845.87	9.95E-07	998.02	0.14	0.29	-
101	WHOI	25 mm projectile	135	0	0.001235	7845.87	9.95E-07	998.02	0.14	0.38	-
102	WHOI	25 mm projectile	135	0	0.001235	7845.87	1.03E-06	998.32	0.13	0.28	-
103	WHOI	25 mm projectile	150	0	0.000962	7845.87	9.95E-07	998.02	0.14	0.20	-
104	WHOI	25 mm projectile	150	0	0.000962	7845.87	9.95E-07	998.02	0.14	0.19	-
105	WHOI	25 mm projectile	150	0	0.000962	7845.87	9.95E-07	998.02	0.14	0.23	-
106	WHOI	25 mm projectile	150	0	0.000962	7845.87	9.95E-07	998.02	0.14	0.23	-
107	WHOI	25 mm projectile	150	0	0.000962	7845.87	1.02E-06	998.23	0.13	0.24	-
108	WHOI	25 mm projectile	170	0	0.000604	7845.87	9.95E-07	998.02	0.13	0.40	-
109	WHOI	25 mm projectile	170	0	0.000604	7845.87	9.95E-07	998.02	0.13	0.39	-
110	WHOI	25 mm projectile	180	0	0.001112	7845.87	9.95E-07	998.02	0.13	0.53	-
111	WHOI	25 mm projectile	180	0	0.001112	7845.87	9.95E-07	998.02	0.13	0.51	-
112	WHOI	25 mm projectile	180	0	0.001112	7845.87	9.95E-07	998.02	0.13	0.58	-
113	WHOI	81 mm finless	10	0	0.005870	3362.49	8.85E-07	996.79	0.14	0.36	-

Table 5 continued…

#	Flume	Nominal Size and Type	θ [degree]	Slope %	Projected area [m^2]	ρ_m [kg/m^3]	ν [m^2/sec]	ρ_w [kg/m^3]	H_c [m]	U [m/s]	T [sec]
114	WHOI	81 mm finless	10	0	0.00587	3362.49	8.85E-07	996.79	0.14	0.33	-
115	WHOI	81 mm finless	10	0	0.00587	3362.49	8.85E-07	996.79	0.14	0.38	-
116	WHOI	81 mm finless	20	0	0.008587	3362.49	9.05E-07	997.05	0.15	0.23	-
117	WHOI	81 mm finless	20	0	0.008587	3362.49	9.05E-07	997.05	0.14	0.41	-
118	WHOI	81 mm finless	20	0	0.008587	3362.49	9.05E-07	997.05	0.15	0.24	-
119	WHOI	81 mm finless	20	0	0.008587	3362.49	9.05E-07	997.05	0.15	0.25	-
120	WHOI	81 mm finless	30	0	0.011703	3362.49	9.30E-07	997.35	0.15	0.19	-
121	WHOI	81 mm finless	30	0	0.011703	3362.49	9.30E-07	997.35	0.15	0.18	-
122	WHOI	81 mm finless	30	0	0.011703	3362.49	9.30E-07	997.35	0.15	0.15	-
123	WHOI	81 mm finless	40	0	0.014568	3362.49	9.05E-07	997.05	0.15	0.18	-
124	WHOI	81 mm finless	40	0	0.014568	3362.49	9.05E-07	997.05	0.15	0.14	-
125	WHOI	81 mm finless	40	0	0.014568	3362.49	9.05E-07	997.05	0.15	0.22	-
126	WHOI	81 mm finless	40	0	0.014568	3362.49	9.05E-07	997.05	0.15	0.14	-
127	WHOI	81 mm finless	40	0	0.014568	3362.49	9.05E-07	997.05	0.15	0.17	-
128	WHOI	81 mm finless	50	0	0.017019	3362.49	9.05E-07	997.05	0.15	0.14	-
129	WHOI	81 mm finless	50	0	0.017019	3362.49	9.05E-07	997.05	0.15	0.14	-

Table 5 continued…

#	Flume	Nominal Size and Type	θ [degree]	Slope %	Projected area [m^2]	ρ_m [kg/m^3]	ν [m^2/sec]	ρ_w [kg/m^3]	H_c [m]	U [m/s]	T [sec]
130	WHOI	81 mm finless	50	0	0.017019	3362.49	9.05E-07	997.05	0.15	0.15	-
131	WHOI	81 mm finless	50	0	0.017019	3362.49	9.05E-07	997.05	0.15	0.15	-
132	WHOI	81 mm finless	60	0	0.019032	3362.49	9.30E-07	997.35	0.15	0.17	-
133	WHOI	81 mm finless	60	0	0.019032	3362.49	9.30E-07	997.35	0.15	0.12	-
134	WHOI	81 mm finless	60	0	0.019032	3362.49	9.30E-07	997.35	0.15	0.18	-
135	WHOI	81 mm finless	70	0	0.020516	3362.49	8.85E-07	996.79	0.15	0.12	--
136	WHOI	81 mm finless	70	0	0.020516	3362.49	8.85E-07	996.79	0.15	0.14	--
137	WHOI	81 mm finless	70	0	0.020516	3362.49	8.85E-07	996.79	0.15	0.15	--
138	WHOI	81 mm finless	80	0	0.021394	3362.49	9.05E-07	997.05	0.15	0.12	--
139	WHOI	81 mm finless	80	0	0.021394	3362.49	9.05E-07	997.05	0.15	0.13	--
140	WHOI	81 mm finless	80	0	0.021394	3362.49	9.05E-07	997.05	0.15	0.15	--
141	WHOI	81 mm finless	80	0	0.021394	3362.49	9.05E-07	997.05	0.15	0.14	--
142	WHOI	81 mm finless	90	0	0.021594	3362.49	9.30E-07	997.35	0.15	0.18	--
143	WHOI	81 mm finless	90	0	0.021594	3362.49	8.85E-07	996.79	0.15	0.16	--

Table 5 continued…

#	Flume	Nominal Size and Type	θ [degree]	Slope %	Projected area [m^2]	ρ_m [kg/m^3]	ν [m^2/sec]	ρ_w [kg/m^3]	H_c [m]	U [m/s]	T [sec]
144	WHOI	81 mm finless	90	0	0.021594	3362.49	8.85E-07	996.79	0.15	0.22	--
145	WHOI	81 mm finless	90	0	0.021594	3362.49	8.85E-07	996.79	0.15	0.10	--
146	WHOI	81 mm finless	90	0	0.021594	3362.49	8.85E-07	996.79	0.15	0.19	--
147	STF	20 mm shell	10	0.6	0.001148	2432.20	9.85E-07	997.93	0.14	0.41	--
148	STF	20 mm shell	10	0.6	0.001148	2432.20	9.85E-07	997.93	0.14	0.38	--
149	STF	20 mm shell	30	0.6	0.002299	2432.20	1.16E-06	999.17	0.18	0.27	--
150	STF	20 mm shell	30	0.6	0.002299	2432.20	1.16E-06	999.17	0.18	0.26	--
151	STF	20 mm shell	30	0.6	0.002299	2432.20	1.16E-06	999.17	0.19	0.32	-
152	STF	20 mm shell	30	0.6	0.002299	2432.20	1.16E-06	999.17	0.18	0.24	-
153	STF	20 mm shell	60	0.6	0.003566	2432.20	1.16E-06	999.17	0.16	0.17	-
154	STF	20 mm shell	60	0.6	0.003566	2432.20	1.01E-06	998.13	0.16	0.15	-
155	STF	20 mm shell	60	0.6	0.003566	2432.20	1.01E-06	998.13	0.16	0.16	-
156	STF	20 mm shell	60	0.6	0.003566	2432.20	1.01E-06	998.13	0.16	0.18	-
157	STF	25 mm shell	10	0.6	0.001897	2106.33	9.85E-07	997.93	0.2	0.37	-

Table 5 continued…

#	Flume	Nominal Size and Type	θ [degree]	Slope %	Projected area [m^2]	ρ_m [kg/m^3]	ν [m^2/sec]	ρ_w [kg/m^3]	H_c [m]	U [m/s]	T [sec]
158	STF	25 mm shell	10	0.6	0.001897	2106.33	9.85E-07	997.93	0.21	0.38	-
159	STF	25 mm shell	30	0.6	0.003783	2106.33	1.02E-06	998.23	0.16	0.28	-
160	STF	25 mm shell	30	0.6	0.003783	2106.33	1.02E-06	998.23	0.18	0.23	-
161	STF	25 mm shell	30	0.6	0.003783	2106.33	1.02E-06	998.23	0.18	0.23	-
162	STF	25 mm shell	30	0.6	0.003783	2106.33	1.02E-06	998.23	0.19	0.31	-
163	STF	25 mm shell	60	0.6	0.005879	2106.33	1.02E-06	998.23	0.17	0.22	-
164	STF	25 mm shell	60	0.6	0.005879	2106.33	1.02E-06	998.23	0.17	0.2	-
165	STF	25 mm shell	60	0.6	0.005879	2106.33	1.02E-06	998.23	0.16	0.15	-
166	STF	25 mm shell	60	0.6	0.005879	2106.33	1.02E-06	998.23	0.17	0.22	-
167	STF	81 mm mortar	10	0.6	0.007768	3293.63	9.85E-07	997.93	0.16	0.73	-
168	STF	81 mm mortar	10	0.6	0.007768	3293.63	9.85E-07	997.93	0.14	0.7	-
169	STF	81 mm mortar	30	0.6	0.016071	3293.63	1.01E-06	998.13	0.2	0.39	-
170	STF	81 mm mortar	30	0.6	0.016071	3293.63	1.01E-06	998.13	0.22	0.5	-
171	STF	81 mm mortar	30	0.6	0.016071	3293.63	1.01E-06	998.13	0.21	0.42	-
172	STF	81 mm mortar	30	0.6	0.016071	3293.63	1.01E-06	998.13	0.2	0.36	-

Table 5 continued…

#	Flume	Nominal Size and Type	θ [degree]	Slope %	Projected area [m^2]	ρ_m [kg/m^3]	ν [m^2/sec]	ρ_w [kg/m^3]	H_c [m]	U [m/s]	T [sec]
173	STF	81 mm mortar	60	0.6	0.025103	3293.63	1.01E-06	998.13	0.19	0.32	-
174	STF	81 mm mortar	60	0.6	0.025103	3293.63	1.01E-06	998.13	0.19	0.32	-
175	STF	81 mm mortar	60	0.6	0.025103	3293.63	1.01E-06	998.13	0.19	0.31	-
176	STF	20 mm shell	10	0.06	0.001148	2432.20	9.58E-07	997.66	0.12	0.33	-
177	STF	20 mm shell	10	0.06	0.001148	2432.20	9.36E-07	997.42	0.13	0.39	-
178	STF	20 mm shell	10	0.06	0.001148	2432.20	9.36E-07	997.42	0.12	0.37	-
179	STF	20 mm shell	30	0.06	0.002299	2432.20	9.36E-07	997.42	0.1	0.26	-
180	STF	20 mm shell	30	0.06	0.002299	2432.20	9.36E-07	997.42	0.1	0.25	-
181	STF	20 mm shell	30	0.06	0.002299	2432.20	9.45E-07	997.52	0.13	0.33	-
182	STF	20 mm shell	60	0.06	0.003566	2432.20	9.36E-07	997.42	0.08	0.13	-
183	STF	20 mm shell	60	0.06	0.003566	2432.20	9.36E-07	997.42	0.09	0.16	-
184	STF	20 mm shell	60	0.06	0.003566	2432.20	9.36E-07	997.42	0.08	0.12	-
185	STF	20 mm shell	90	0.06	0.003901	2432.20	9.36E-07	997.42	0.08	0.05	-
186	STF	20 mm shell	90	0.06	0.003901	2432.20	9.36E-07	997.42	0.08	0.05	-
187	STF	25 mm shell	10	0.06	0.001897	2106.33	9.58E-07	997.66	0.18	0.51	-

Table 5 continued…

#	Flume	Nominal Size and Type	θ [degree]	Slope %	Projected area [m^2]	ρ_m [kg/m^3]	ν [m^2/sec]	ρ_w [kg/m^3]	H_c [m]	U [m/s]	T [sec]
188	STF	25 mm shell	10	0.06	0.001897	2106.33	9.58E-07	997.66	0.16	0.45	-
189	STF	25 mm shell	10	0.06	0.001897	2106.33	9.38E-07	997.45	0.15	0.39	-
190	STF	25 mm shell	30	0.06	0.003783	2106.33	9.67E-07	997.75	0.17	0.26	-
191	STF	25 mm shell	30	0.06	0.003783	2106.33	9.67E-07	997.75	0.16	0.19	-
192	STF	25 mm shell	30	0.06	0.003783	2106.33	9.38E-07	997.45	0.18	0.32	-
193	STF	25 mm shell	30	0.06	0.003783	2106.33	9.38E-07	997.45	0.18	0.29	-
194	STF	25 mm shell	40	0.06	0.004621	2106.33	9.45E-07	997.52	0.18	0.28	-
195	STF	25 mm shell	40	0.06	0.004621	2106.33	9.45E-07	997.52	0.17	0.27	-
196	STF	25 mm shell	60	0.06	0.005879	2106.33	9.67E-07	997.75	0.16	0.19	-
197	STF	25 mm shell	60	0.06	0.005879	2106.33	9.67E-07	997.75	0.15	0.16	-
198	STF	25 mm shell	90	0.06	0.006431	2106.33	9.67E-07	997.75	0.23	0.19	-
199	STF	25 mm shell	90	0.06	0.006431	2106.33	9.67E-07	997.75	0.16	0.19	-
200	STF	25 mm shell	90	0.06	0.006431	2106.33	9.67E-07	997.75	0.16	0.18	-
201	STF	81 mm mortar	10	0.06	0.007768	3293.63	9.58E-07	997.66	0.17	0.59	-

Table 5 continued…

#	Flume	Nominal Size and Type	θ [degree]	Slope %	Projected area [m^2]	ρ_m [kg/m^3]	ν [m^2/sec]	ρ_w [kg/m^3]	H_c [m]	U [m/s]	T [sec]
202	STF	81 mm mortar	10	0.06	0.007768	3293.63	9.58E-07	997.66	0.17	0.62	-
203	STF	81 mm mortar	30	0.06	0.016071	3293.63	9.58E-07	997.66	0.18	0.59	-
204	STF	81 mm mortar	30	0.06	0.016071	3293.63	9.58E-07	997.66	0.18	0.48	-
205	STF	81 mm mortar	40	0.06	0.019658	3293.63	9.45E-07	997.52	0.15	0.28	-
206	STF	81 mm mortar	40	0.06	0.019658	3293.63	9.45E-07	997.52	0.15	0.27	-
207	STF	81 mm mortar	40	0.06	0.019658	3293.63	9.45E-07	997.52	0.15	0.37	-
208	STF	81 mm mortar	40	0.06	0.019658	3293.63	9.45E-07	997.52	0.18	0.4	-
209	STF	81 mm mortar	50	0.06	0.022684	3293.63	9.45E-07	997.52	0.19	0.26	-
210	STF	81 mm mortar	50	0.06	0.022684	3293.63	9.45E-07	997.52	0.21	0.34	-
211	STF	81 mm mortar	50	0.06	0.022684	3293.63	9.45E-07	997.52	0.21	0.36	-
212	STF	81 mm mortar	60	0.06	0.025103	3293.63	9.58E-07	997.66	0.21	0.36	-
213	STF	81 mm mortar	60	0.06	0.025103	3293.63	9.58E-07	997.66	0.2	0.3	-
214	STF	81 mm mortar	60	0.06	0.025103	3293.63	9.58E-07	997.66	0.21	0.35	-
215	STF	81 mm mortar	70	0.06	0.0268	3293.63	9.38E-07	997.45	0.18	0.31	-
216	STF	81 mm mortar	90	0.06	0.027781	3293.63	9.58E-07	997.66	0.13	0.19	-

Table 5 continued…

#	Flume	Nominal Size and Type	θ [degree]	Slope %	Projected area [m^2]	ρ_m [kg/m^3]	ν [m^2/sec]	ρ_w [kg/m^3]	H_c [m]	U [m/s]	T [sec]
217	STF	91 mm mortar	90	0.06	0.027781	3293.63	9.58E-07	997.66	0.13	0.19	-
218	WHOI	20 mm shell	20	0	0.001734	2432.20	1.02E-06	998.23	0.66	0.1	-
219	WHOI	20 mm shell	40	0	0.002812	2432.20	1.02E-06	998.23	0.1	0.32	-
220	WHOI	20 mm shell	45	0	0.003024	2432.20	1.02E-06	998.23	0.1	0.23	-
221	WHOI	20 mm shell	45	0	0.003024	2432.20	1.02E-06	998.23	0.1	0.32	-
222	WHOI	20 mm shell	70	0	0.003605	2432.20	1.02E-06	998.23	0.11	0.19	-
223	WHOI	20 mm shell	70	0	0.003605	2432.20	1.02E-06	998.23	0.11	0.22	-
224	WHOI	20 mm shell	90	0	0.003901	2432.20	1.02E-06	998.23	0.1	0.22	-
225	WHOI	20 mm shell	90	0	0.003901	2432.20	1.02E-06	998.23	0.1	0.23	-
226	WHOI	20 mm shell	135	0	0.002555	2432.20	1.02E-06	998.23	0.1	0.28	-
227	WHOI	20 mm shell	135	0	0.002555	2432.20	1.02E-06	998.23	0.1	0.23	-
228	WHOI	20 mm shell	160	0	0.001734	2432.20	1.02E-06	998.23	0.1	0.35	-
229	WHOI	20 mm shell	160	0	0.001734	2432.20	1.02E-06	998.23	0.11	0.39	-
230	WHOI	20 mm shell	160	0	0.001734	2432.20	1.02E-06	998.23	0.1	0.37	-
231	WHOI	20 mm shell	180	0	0.00067	2432.20	1.02E-06	998.23	0.11	0.47	-
232	WHOI	20 mm shell	180	0	0.00067	2432.20	1.02E-06	998.23	0.1	0.43	-

Table 5 continued…

#	Flume	Nominal Size and Type	θ [degree]	Slope %	Projected area [m^2]	ρ_m [kg/m^3]	ν [m^2/sec]	ρ_w [kg/m^3]	H_c [m]	U [m/s]	T [sec]
233	LOWST - np[3]	20 mm shell	80	0	0.006448	2106.33	1.02E-06	998.23	0.6	0.55	-
234	LOWST - np	20 mm shell	80	0	0.006448	2106.33	1.02E-06	998.23	0.6	0.27	-
235	LOWST - np	20 mm shell	80	0	0.006448	2106.33	1.02E-06	998.23	0.6	0.32	-
236	LOWST - np	20 mm shell	60	0	0.000985	2432.20	1.02E-06	998.23	0.6	0.48	-
237	LOWST - np	81 mm mortar	80	0	0.027723	3293.63	1.02E-06	998.23	0.6	0.46	-
238	LOWST - np	81 mm mortar	80	0	0.027723	3293.63	1.02E-06	998.23	0.6	0.55	-
239	LOWST - np	IMU cylinder	80	0	0.0141	1284.15	1.02E-06	998.23	0.6	0.4	-
240	LOWST - np	IMU cylinder	80	0	0.0141	1284.15	1.02E-06	998.23	0.6	0.3	-
241	LOWST - np	IMU cylinder	80	0	0.0141	1284.15	1.02E-06	998.23	0.6	0.21	-
242	LOWST - np	IMU cylinder	80	0	0.0141	1284.15	1.02E-06	998.23	0.6	0.41	-
243	LOWST - np	IMU cylinder	80	0	0.0141	1284.15	1.02E-06	998.23	0.6	0.48	-
244	LOWST - np	IMU cylinder	90	0	0.0134	1284.15	1.02E-06	998.23	0.6	0.41	-
245	LOWST - np	IMU cylinder	90	0	0.0134	1284.15	1.02E-06	998.23	0.6	0.43	-
246	LOWST - np	IMU cylinder	90	0	0.0134	1284.15	1.02E-06	998.23	0.6	0.43	-

[3] np: non pressurized flow conditions.

Table 5 continued…

#	Flume	Nominal Size and Type	θ [degree]	Slope %	Projected area [m^2]	ρ_m [kg/m^3]	ν [m^2/sec]	ρ_w [kg/m^3]	H_c [m]	U [m/s]	T [sec]
247	IHFF	63 mm cylinder	90	0	0.019152	1472.60	1.02E-06	998.23	0.09	0.31	-
248	IHFF	63 mm cylinder	90	0	0.019026	1244.09	1.02E-06	998.23	0.09	0.21	-
249	IHFF	51 mm cylinder	90	0	0.015453	1424.94	1.02E-06	998.23	0.09	0.34	-
250	IHFF	51 mm cylinder	90	0	0.015453	1192.46	1.02E-06	998.23	0.09	0.23	-
251	IHFF	38 mm cylinder	90	0	0.011514	1436.40	1.02E-06	998.23	0.09	0.38	-
252	IHFF	38 mm cylinder	90	0	0.011514	1202.67	1.02E-06	998.23	0.09	0.25	-
253	IHFF	25 mm cylinder	90	0	0.007575	1475.11	1.02E-06	998.23	0.09	0.42	-
254	IHFF	25 mm cylinder	90	0	0.00755	1247.27	1.02E-06	998.23	0.09	0.29	-
255	IHFF	19 mm cylinder	90	0	0.005738	1448.16	1.02E-06	998.23	0.09	0.47	-

Table 5 continued…

#	Flume	Nominal Size and Type	θ [degree]	Slope %	Projected area [m^2]	ρ_m [kg/m^3]	ν [m^2/sec]	ρ_w [kg/m^3]	H_c [m]	U [m/s]	T [sec]
256	IHFF	19 mm cylinder	90	0	0.005757	1211.74	1.02E-06	998.23	0.08	0.35	-
257	IHFF	63 mm cylinder	90	0	0.019152	1472.60	1.02E-06	998.23	0.08	0.25	-
258	IHFF	63 mm cylinder	90	0	0.019026	1244.09	1.02E-06	998.23	0.08	0.17	-
259	IHFF	51 mm cylinder	90	0	0.015453	1424.94	1.02E-06	998.23	0.08	0.27	-
260	IHFF	51 mm cylinder	90	0	0.015453	1192.46	1.02E-06	998.23	0.08	0.19	-
261	IHFF	38 mm cylinder	90	0	0.011514	1436.40	1.02E-06	998.23	0.08	0.3	-
262	IHFF	38 mm cylinder	90	0	0.011514	1202.67	1.02E-06	998.23	0.08	0.2	-
263	IHFF	25 mm cylinder	90	0	0.007575	1475.11	1.02E-06	998.23	0.08	0.33	-
264	IHFF	25 mm cylinder	90	0	0.00755	1247.27	1.02E-06	998.23	0.08	0.22	-
265	IHFF	19 mm cylinder	90	0	0.005738	1448.16	1.02E-06	998.23	0.08	0.34	-
266	IHFF	19 mm cylinder	90	0	0.005757	1211.74	1.02E-06	998.23	0.08	0.23	-
267	IHFF	63 mm sphere	-	0	0.003117	1400.00	1.02E-06	998.23	0.09	0.43	-
268	IHFF	63 mm sphere	-	0	0.003117	1200.00	1.02E-06	998.23	0.09	0.3	-
269	IHFF	51 mm sphere	-	0	0.002043	1400.00	1.02E-06	998.23	0.09	0.43	-
270	IHFF	51 mm sphere	-	0	0.002043	1200.00	1.02E-06	998.23	0.09	0.28	-

Table 5 continued…

#	Flume	Nominal Size and Type	θ [degree]	Slope %	Projected area [m^2]	ρ_m [kg/m^3]	ν [m^2/sec]	ρ_w [kg/m^3]	H_c [m]	U [m/s]	T [sec]
271	IHFF	38 mm sphere	-	0	0.001134	1400.00	1.02E-06	998.23	0.09	0.42	-
272	IHFF	38 mm sphere	-	0	0.001134	1200.00	1.02E-06	998.23	0.09	0.3	-
273	IHFF	25 mm sphere	-	0	0.000491	1400.00	1.02E-06	998.23	0.09	0.44	-
274	IHFF	25 mm sphere	-	0	0.000491	1200.00	1.02E-06	998.23	0.09	0.32	-
275	IHFF	19 mm sphere	-	0	0.000284	1400.00	1.02E-06	998.23	0.09	0.56	-
276	IHFF	19 mm sphere	-	0	0.000284	1200.00	1.02E-06	998.23	0.09	0.39	-
277	IHFF	63 mm sphere	-	0	0.003117	1400.00	1.02E-06	998.23	0.08	0.42	-
278	IHFF	63 mm sphere	-	0	0.003117	1200.00	1.02E-06	998.23	0.08	0.28	-
279	IHFF	51 mm sphere	-	0	0.002043	1400.00	1.02E-06	998.23	0.08	0.45	-
280	IHFF	51 mm sphere	-	0	0.002043	1200.00	1.02E-06	998.23	0.08	0.29	-
281	IHFF	38 mm sphere	-	0	0.001134	1400.00	1.02E-06	998.23	0.08	0.45	-
282	IHFF	38 mm sphere	-	0	0.001134	1200.00	1.02E-06	998.23	0.08	0.3	-
283	IHFF	25 mm sphere	-	0	0.000491	1400.00	1.02E-06	998.23	0.07	0.54	-
284	IHFF	25 mm sphere	-	0	0.000491	1200.00	1.02E-06	998.23	0.08	0.35	-
285	IHFF	19 mm sphere	-	0	0.000284	1400.00	1.02E-06	998.23	0.08	0.56	-
286	IHFF	19 mm sphere	-	0	0.000284	1200.00	1.02E-06	998.23	0.07	0.37	-

Table 5 continued…

#	Flume	Nominal Size and Type	θ [degree]	Slope %	Projected area [m^2]	ρ_m [kg/m^3]	ν [m^2/sec]	ρ_w [kg/m^3]	H_c [m]	U [m/s]	T [sec]
287	IHFF	63 mm cylinder	90	0	0.010801	1400.00	1.02E-06	998.23	0.09	0.36	-
288	IHFF	63 mm cylinder	90	0	0.010801	1200.00	1.02E-06	998.23	0.09	0.24	-
289	IHFF	51 mm cylinder	90	0	0.007125	1400.00	1.02E-06	998.23	0.09	0.37	-
290	IHFF	51 mm cylinder	90	0	0.007125	1200.00	1.02E-06	998.23	0.09	0.25	-
291	IHFF	38 mm cylinder	90	0	0.003861	1400.00	1.02E-06	998.23	0.09	0.38	-
292	IHFF	38 m mcylinder	90	0	0.003861	1200.00	1.02E-06	998.23	0.09	0.25	-
293	IHFF	25 mm cylinder	90	0	0.001746	1400.00	1.02E-06	998.23	0.09	0.39	-
294	IHFF	25 mm cylinder	90	0	0.001746	1200.00	1.02E-06	998.23	0.09	0.26	-
295	IHFF	19 mm cylinder	90	0	0.001086	1400.00	1.02E-06	998.23	0.09	0.41	-
296	IHFF	19 mm cylinder	90	0	0.001086	1200.00	1.02E-06	998.23	0.09	0.28	-
297	IHFF	63 mm cylinder	90	0	0.010801	1400.00	1.02E-06	998.23	0.08	0.33	-
298	IHFF	63 mm cylinder	90	0	0.010801	1200.00	1.02E-06	998.23	0.08	0.22	-
299	IHFF	51 mm cylinder	90	0	0.007125	1400.00	1.02E-06	998.23	0.08	0.35	-
300	IHFF	51 mm cylinder	90	0	0.007125	1200.00	1.02E-06	998.23	0.08	0.24	-

Table 5 continued…

#	Flume	Nominal Size and Type	θ [degree]	Slope %	Projected area [m^2]	ρ_m [kg/m^3]	ν [m^2/sec]	ρ_w [kg/m^3]	H_c [m]	U [m/s]	T [sec]
301	IHFF	38 mm cylinder	90	0	0.003861	1400.00	1.02E-06	998.23	0.08	0.36	-
302	IHFF	38 mm cylinder	90	0	0.003861	1200.00	1.02E-06	998.23	0.08	0.25	-
303	IHFF	25 mm cylinder	90	0	0.001746	1400.00	1.02E-06	998.23	0.07	0.39	-
304	IHFF	25 mm cylinder	90	0	0.001746	1200.00	1.02E-06	998.23	0.07	0.26	-
305	IHFF	19 mm cylinder	90	0	0.001086	1400.00	1.02E-06	998.23	0.07	0.38	-
306	IHFF	19 mm cylinder	90	0	0.001086	1200.00	1.02E-06	998.23	0.07	0.26	-

Table 6: Oscillatory Experimental Data. First column (#): the number of experiment, second column: the flume used for the experiment, third column: the nominal diameter of the examined munition or object, fourth column: the angle of attack, fifth column: the slope of the flume, sixth column: the projected area of the munition of object, seventh column (ρ_m): the munition density, eighth column (ν): the kinematic viscosity of water, ninth column (ρ_w); the water density, tenth column (H_c): the characteristic depth of the flow (water depth for open channel flows and half the channel height for channel flows), eleventh column (U): critical velocity for initiation of motion, twelfth column (T): the period of the flow for the case of oscillatory flows.

#	Flume	Nominal Size and Type	θ^o [degrees]	Slope [%]	Projected area [m^2]	ρ_m [kg/m^3]	ν [m^2/sec]	ρ_w [kg/m^3]	H_c [m]	U [m/s]	T [sec]
307	LOWST	20 mm shell	0	0	0.000670	2432.20	1.02E-06	998.23	0.30	0.61	8.00
308	LOWST	20 mm shell	0	0	0.000670	2432.20	1.02E-06	998.23	0.30	0.56	6.00
309	LOWST	20 mm shell	0	0	0.000670	2432.20	1.02E-06	998.23	0.30	0.21	4.00
310	LOWST	20 mm shell	0	0	0.000670	2432.20	1.02E-06	998.23	0.30	0.15	2.00
311	LOWST	81 mm mortar	90	0	0.027781	3293.63	1.02E-06	998.23	0.30	0.29	12.00
312	LOWST	81 mm mortar	90	0	0.027781	3293.63	1.02E-06	998.23	0.30	0.20	12.00
313	LOWST	81 mm mortar	90	0	0.027781	3293.63	1.02E-06	998.23	0.30	0.20	10.00
314	LOWST	81 mm mortar	90	0	0.027781	3293.63	1.02E-06	998.23	0.30	0.22	10.00
315	LOWST	81 mm mortar	90	0	0.027781	3293.63	1.02E-06	998.23	0.30	0.26	8.00
316	LOWST	81 mm mortar	90	0	0.027781	3293.63	1.02E-06	998.23	0.30	0.29	6.00
317	LOWST	81 mm mortar	90	0	0.027781	3293.63	1.02E-06	998.23	0.30	0.20	4.00
318	LOWST	81 mm mortar	90	0	0.027781	3293.63	1.02E-06	998.23	0.30	0.15	4.00
319	LOWST	81 mm mortar	90	0	0.027781	3293.63	1.02E-06	998.23	0.30	0.05	3.00
320	LOWST	81 mm mortar	90	0	0.027781	3293.63	1.02E-06	998.23	0.30	0.16	2.00
321	LOWST	81 mm mortar	90	0	0.027781	3293.63	1.02E-06	998.23	0.30	0.04	2.00

Table 6 continued…

#	Flume	Nominal Size and Type	θ° [degrees]	Slope [%]	Projected area [m^2]	ρ_m [kg/m^3]	ν [m^2/sec]	ρ_w [kg/m^3]	H_c [m]	U [m/s]	T [sec]
322	LOWST	81 mm mortar	0	0	0.005002	3293.63	1.02E-06	998.23	0.30	0.40	10.00
323	LOWST	81 mm mortar	0	0	0.005002	3293.63	1.02E-06	998.23	0.30	0.50	8.00
324	LOWST	81 mm mortar	0	0	0.005002	3293.63	1.02E-06	998.23	0.30	0.40	6.00
325	LOWST	81 mm mortar	0	0	0.005002	3293.63	1.02E-06	998.23	0.30	0.40	4.00

Appendix D: The Acceleration/inertia Correction Factor, f_I

In the scaling analysis, we introduced the acceleration/inertia correction factor, f_I. This correction factor can be derived using the Morison equation according to which, in an oscillatory flow the total force that a submerged object experiences can be expressed as:

$$F = \underbrace{\rho C_I V_o \dot{u}}_{F_I} + \underbrace{\frac{1}{2}\rho C_D A_p u|u|}_{F_D},$$

where F is the time varying total force on an object, F_I is the inertia force, F_D is the drag force, C_I is the inertia coefficient, C_D is the drag coefficient, V_o is the volume of the body, A_p is the projected area, $\dot{u}$ is the time varying acceleration of the flow and u is the time varying velocity.

From the above the ratio between the total force and the drag force can be derived as:

$$\frac{F_D + F_I}{F_D} \approx 1 + 4\pi\left(C_I/C_D\right)/\left(KC\right)$$

Thus, a correction factor, f_I, can be defined as:

$$f_I = \left(\frac{F_D + F_I}{F_D}\right)^{1/2} \approx \left(1 + 4\pi\left(C_I/C_D\right)/\left(KC\right)\right)^{1/2}$$

In the following Figure, the correction coefficient, f_I, is plotted versus the KC number. It is shown that for low KC numbers f_I can take values as large as 30 (KC = 0.1) and 1 (KC = 0.01).

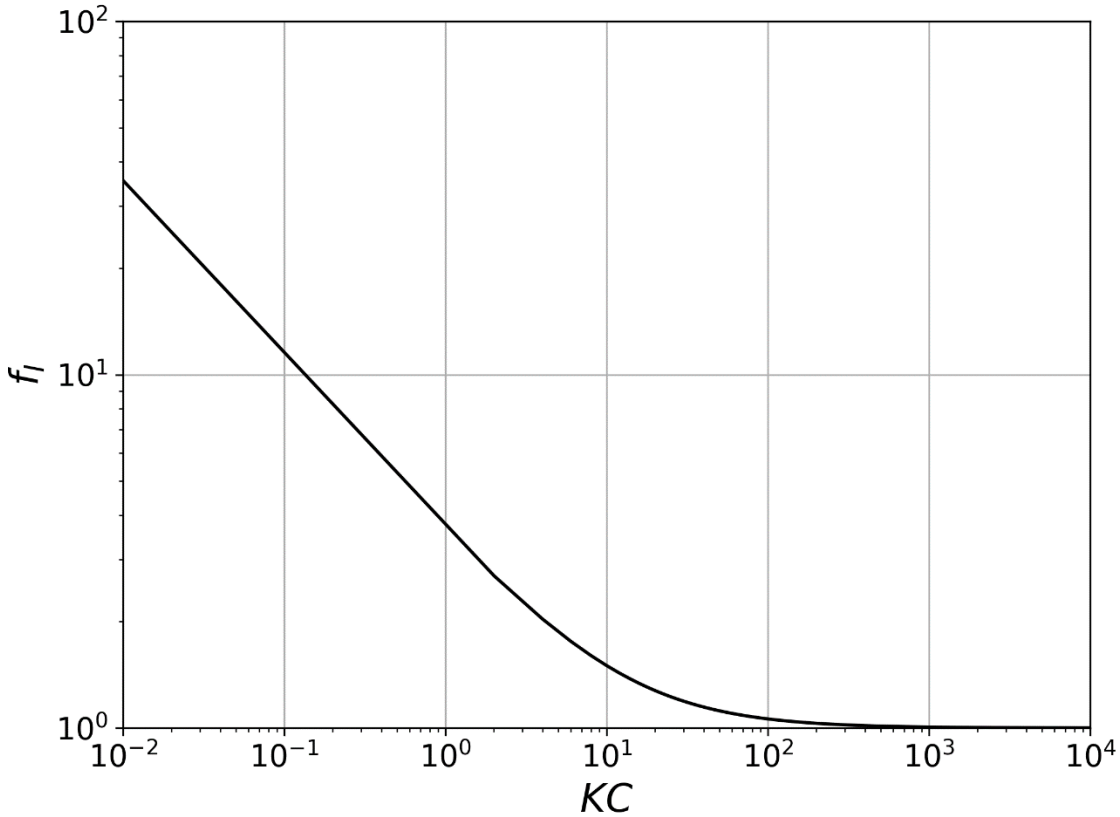

Figure 35: Inertia/acceleration correction factor f_I.

References:

Morison, J. R.; O'Brien, M. P.; Johnson, J. W.; Schaaf, S. A. (1950), "The force exerted by surface waves on piles", Petroleum Transactions, American Institute of Mining Engineers, 189: 149–154, doi:10.2118/950149-G

Appendix E: Enhanced Flow Measurements

Enhanced flow measurements were conducted for some cases to better understand the flow around the munition by employing Particle Image Velocimetry (PIV).

Particle Image Velocimetry (PIV) technique was employed to measure the flow velocity field around the munition. By taking image pairs of the tracers in the flow with a small time separation, the instantaneous flow velocity fields were obtained. The tracers used in the experiments are silver coated hollow glass spheres (40 μm diameter) that can follow the motion of the flow. To capture the motion of the tracers, a laser sheet was positioned vertically into the flow to illuminate the particles in the observation plane. The laser light was scattered by the tracers and captured by a CCD camera. The velocity of the fluid at each grid node in an image was mapped from the average of the velocity of the tracers around the grid node. For more information about PIV, please refer to Raffel *et al.* (1998). Our PIV system includes a New Wave Gemini Nd:YAG laser, Power View 4 MP Plus CCD camera, TSI 610035 synchronizer, and optics such as cylindrical lenses and mirrors to spread and direct the laser sheet vertically into the tunnel. The field of view achieved was about 0.2 m by 0.2 m.

Unidirectional flow experiments were performed in the Illinois Hyporheic Flow Facility (IHFF). Oscillatory flow experiments were performed in the Small Oscillatory Tunnel (SOT).

PIV experiments were conducted in the Illinois Hyporheic Flow Facility (IHFF) to illustrate the flow field around the munition under unidirectional flow when the munition is aligned with the flow on a flat plate. Five tests were conducted in IHFF with different free stream velocities ranging from 0.04 m/s to 0.78 m/s as listed in Table 7 covering the range of flow velocities in which initiation of motion was observed in the WHOI flume or the STF. Results are discussed in the Results section.

Table 7: The conditions of the experiments in IHFF

Test no.	Free Stream Velocity [m/s]
1	0.78
2	0.25
3	0.15
4	0.06
5	0.04

Experiments were done in the Small Oscillatory Tunnel (SOT) to explore the flow field around the munition under oscillatory flow when the munition is fixed on the bottom. Two cases were examined with munition aligned either perpendicular or parallel to the flow.

Table 8: The conditions of the experiments in the Small Oscillatory Tunnel

Test no.	Period, T [s]	Amplitude, A [m]
1	5	0.10
2	5	0.06
3	3	0.08
4	3	0.04
5	2	0.04
6	2	0.02

To construct the mean flow field in three dimensions around the munition under oscillatory flows, PIV measurements were taken at different locations. The measurements were done for six slices when the munition is perpendicular to the flow direction and two slices when the munition is aligned parallel to the flow. The location of the slices on the munition is shown in Figure 36. To date, more than 3 terabytes of PIV slicing image data is being processed to reconstruct the flow field in three dimensions around the munition.

Reflection of the laser light from the munition presented a problem for resolving the velocity field near the munition. To reduce the laser reflection from the munition, the munition is coated with resin that contains Rhodamine WT. The Rhodamine WT paint absorbs the green laser light (wavelength of 532 nm) and emits a light with a different wavelength (545 nm). Applying a band pass filter on the camera lens allows the green light scattered by the PIV seeding particles to be seen by the camera but filters out the 545 nm reflection from the Rhodamine WT coating applied on the munition.

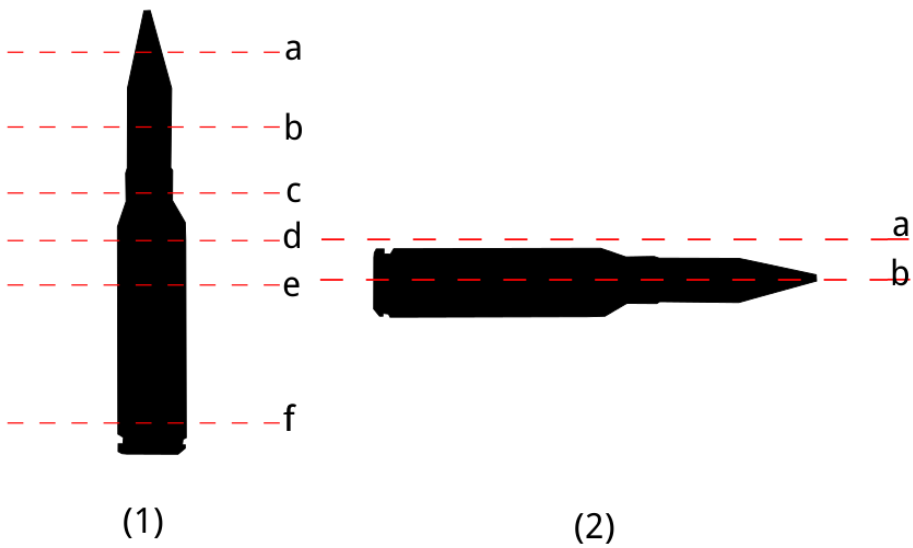

Figure 36: The top view of the locations on the munition where the slices of PIV measurements were taken. "Slice a" is the closest to the camera.

Part I: Understanding flow dynamics of fixed munitions

Part I is conducted to obtain the flow field measurements of munitions fixed to the bottom of a channel to gain insight on the flow dynamics around the munition. For this portion, we perform PIV measurements of the fixed munition in a unidirectional channel and in a small oscillatory tunnel. From the PIV measurements, we have the instantaneous flow velocity fields. With these velocity fields, we can calculate the mean flow velocity fields and the vorticity that can indicate the flow separation zones, relevant in erosion effects. The PIV data shall also aid in the estimation of the forces on the munition and calculation of drag coefficients which can be used to better understand and predict munition migration.

Part II: Flow estimation of moving munition.

The last objective of our flow measurements is to get PIV results for a munition at the instant of imminent motion. The reason is to observe the flow dynamics around the munition at the instant of imminent motion and when the munition is moving while tracking the motion of the munition itself with other techniques (e.g., electronically with the IMU). These measurements were performed in oscillatory flow conditions on a gravel bed. Our intent is also to use the data generated in this portion and to compare it to the plots generated by Friederichs (2013). Note that Komar and Li (1988) have a model that is very similar to the one by Kirchner et al. (1990), used by Friederichs.

Results

Results for Part I: Understanding flow dynamics of fixed munitions

PIV results for mean streamwise velocity and vorticity are plotted in Figure 37 and Figure 38, respectively, for the unidirectional flow experiments performed in the IHFF. Five different flow velocities are shown in each figure. The munition is aligned parallel to the flow for all five cases

and the laser sheet is aligned with the centerline of the munition. In these figures, the free stream is flowing from the left to the right. Figure 37 shows the contours of the mean streamwise velocity fields. The flow is faster in the upper region away from the munition. In the wake region downstream of the munition, the flow is in the reverse direction. To better illustrate the shear between the wake region and the flow above the munition, the vorticity was calculated as shown in Figure 38. The vorticity is close to zero in the free stream. There is a tail of strong vortices immediately behind the munition. The strength of the vortices decreases as the free stream flow velocity decreases.

In addition to the unidirectional flows examined in the IHFF, PIV experiments were also carried out in the SOT for oscillatory flows. Figure 39 shows a sample of the phase-averaged streamwise velocity field. Phase-averaged streamwise velocity is calculated by averaging the streamwise velocity fields at each specific phase in the piston cycle. The test shown here is “slice d” (refer to Figure 36) of the munition aligned perpendicular to the flow direction. The oscillatory flow period is 3 seconds and a half stroke is 0.04 m. Twenty image pairs were acquired per piston cycle. In Figure 39, it can be observed that the free stream flow is a sine wave. The flow velocity field near the munition is well resolved. The region just above the munition has the fastest streamwise velocity that increases and decreases with the speed of the free stream flow. On the downstream side of the munition, the flow is reversed. The region with a reversed velocity grows as the free stream velocity decreases. In the future, we plan to better identify the regions by calculating the vorticities at the various phases in the oscillations.

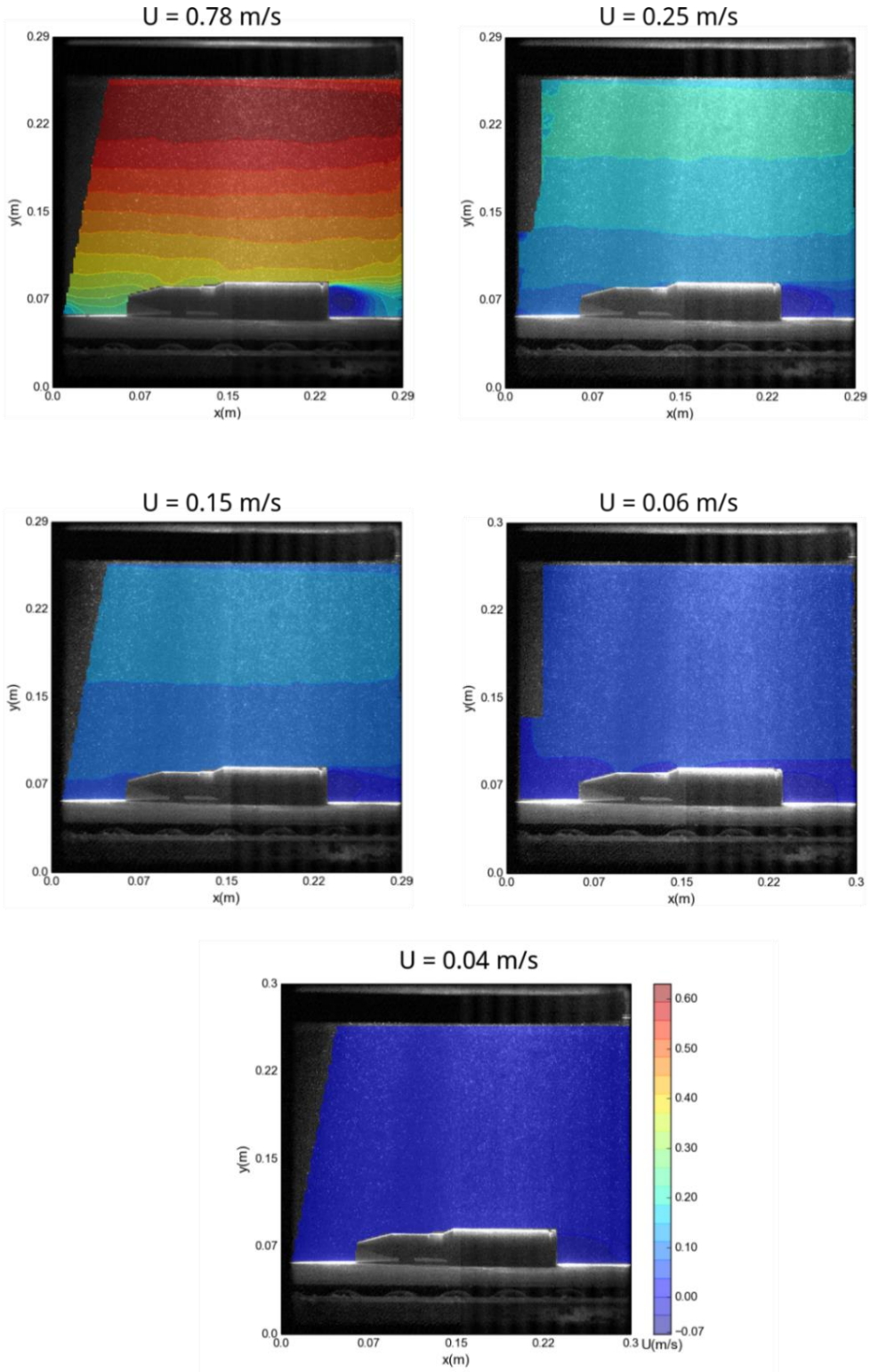

Figure 37: The contours of the mean streamwise velocity field around the munition across the centerline under five different free stream flow velocities (shown in Table 7). Flow is from left to right.

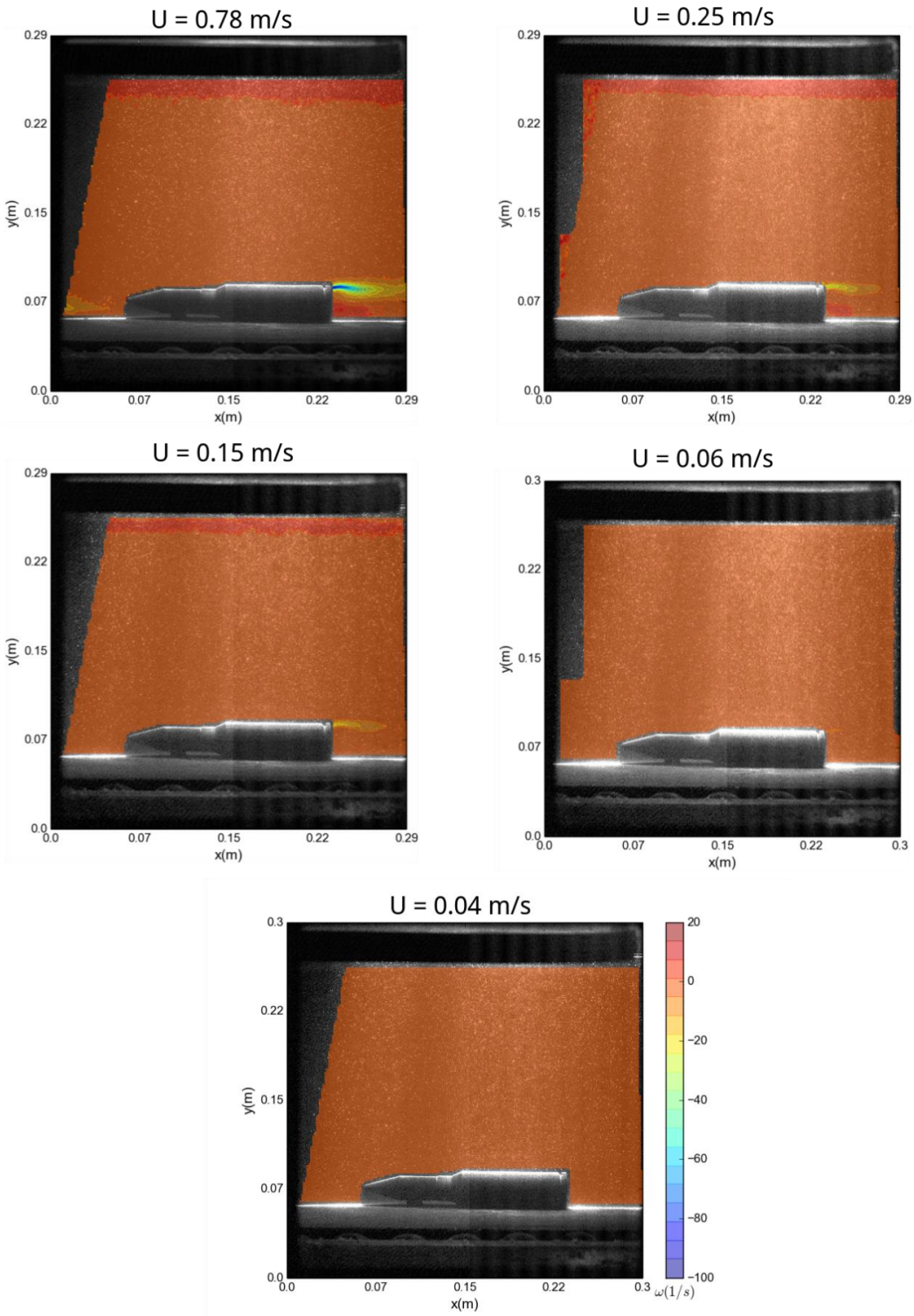

Figure 38: The vorticity around the munition across the centerline under different free stream velocities (shown in Table 7). The positive vorticity is counterclockwise.

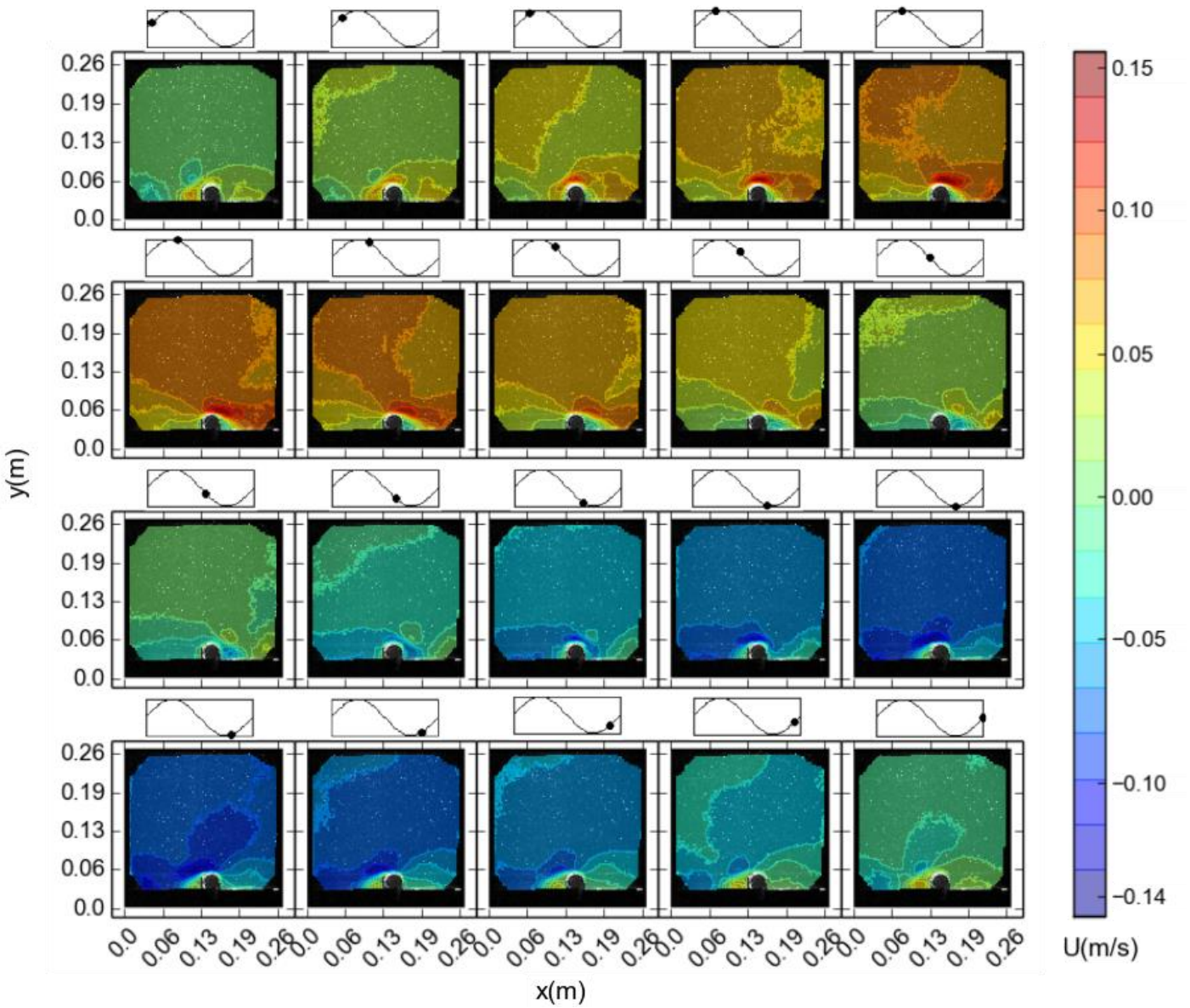

Figure 39: The contour of the streamwise mean velocity at each phase in a cycle. In this test, the period of the piston is 3 sec and the half stroke is 0.04 m

Results for Part II: Flow estimation of moving munition

The incipient motion of the IMU cylinder was tested on a gravel bed for the wave period of 10 seconds. The maximum near bed orbital velocity required to initiate the motion of the IMU cylinder was 0.22 m/s. The incipient motion was observed to occur at around the maximum acceleration rather than at maximum velocity over a cycle, see Figure 40. The result supports the phase lead of the wall shear stress relative to the free stream flow velocity (Jonsson, 1980).

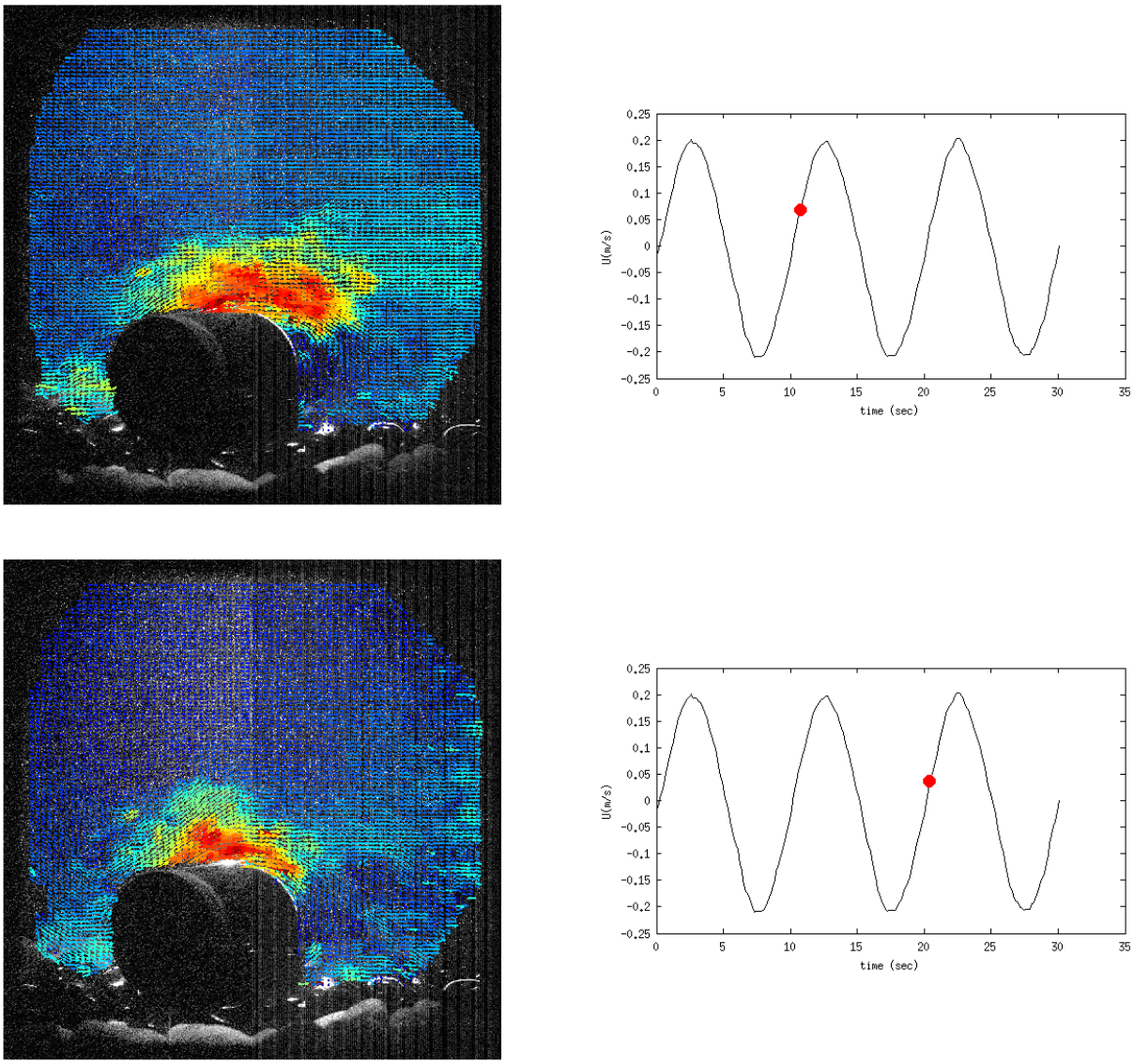

Figure 40: Synchronized PIV and IMU data support phase lead of initiation of motion. The red dot denotes the time when the initiation of motion occurred.

Appendix F: Numerical Modeling

In addition to the laboratory experiments, numerical modeling was also conducted to help estimate the effect of angle of attack through simulations of the flow around near bed placed UXOs using the Reynolds-Averaged Navier-Stokes approach combined with the Computational Fluid Dynamics (CFD) algorithms included in the commercial CFD solver ANSYS Fluent 18.0. In the numerical model, the munition surrogates are placed approximately 1.0 mm above the bottom of the flume in order to mimic the conditions in the experiment. The dimensions of the examined geometry of the UXOs can be found in Table 1.

The dimensions of the computational domain are 3.2 m length, 0.8 m width, and 0.6 m height to reproduce the unidirectional flow experiments carried out in Large Oscillatory Water-Sediment Tunnel (LOWST; Ven Te Chow Hydrosystems Laboratory, UIUC). The corresponding computational gird is shown in Figure 41a). In addition to the LOWST experiments, unidirectional flow scenarios were examined for unidirectional flows in the Illinois Hyporheic Flow Facility (IHFF). For the IHFF experiments, the computational domain had 2.5 m length, 0.8 m width and 0.6 m height. The computational grid for the hyporheic facility experiments modeling can be found in Figure 41b).

For the above scenarios, PIV velocity measurements were available from the experiments conducted in LOWST and hyporheic flume and the obtained velocity profiles have been compared with the present numerical results.

For the unidirectional cases, the boundary conditions applied are: a) velocity profile at the inlet surface (Dirichlet boundary condition) and zero gradient for the pressure, b) “pressure outlet” boundary condition at the surface at the outflow surface (constant relative pressure p = 0.0 Pa and zero gradient for the velocity) c) the rest of the surfaces (bottom, top, side walls and munition surface) were defined as smooth no-slip walls (velocity equals zero at the wall).

In addition to the laboratory experiments, numerical modeling was performed to help estimate the effect of oscillatory flow characteristics (period and amplitude of oscillation). The approach for the simulation of oscillatory flow is similar to the unidirectional flow approach. However, time-dependent boundary conditions are for the Dirichlet boundary condition instead of a steady state profile. The velocity at the inlet assumed to be uniform but time-dependent.

The computational grid is unstructured and had approximately 8,200,000 computational cells. Local refinement was applied in order to capture the geometric details of the examined munition surrogate. Close to the examined obstacle as well as close to the bottom, top and side walls prismatic layers have been used to accurately resolve the close to the wall region which is crucial for the accurate prediction of the drag forces on the munition.

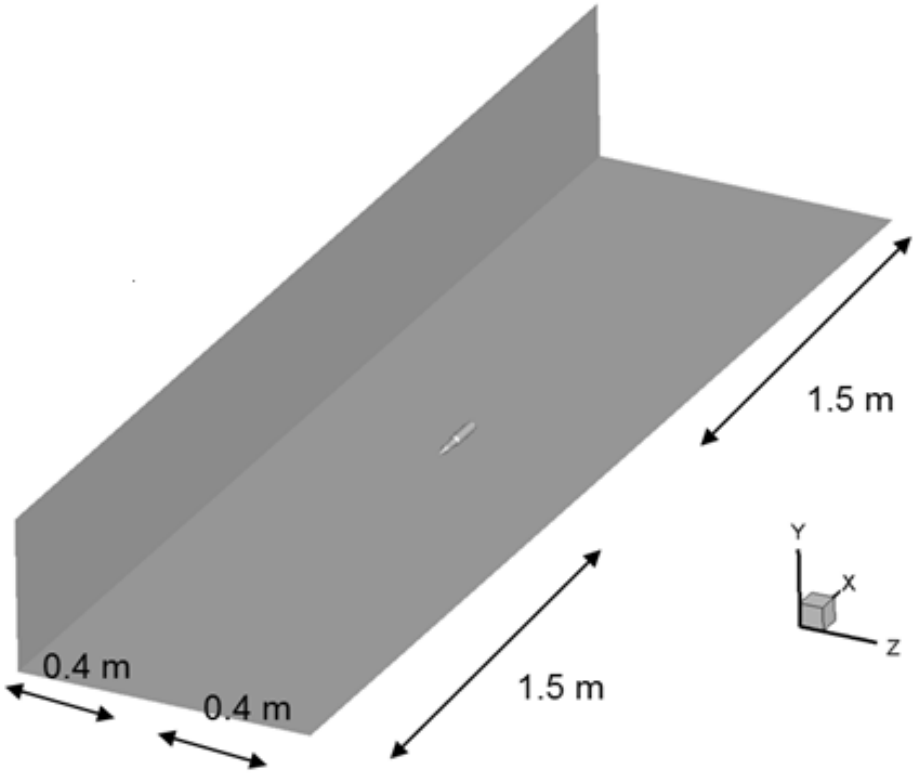

a)

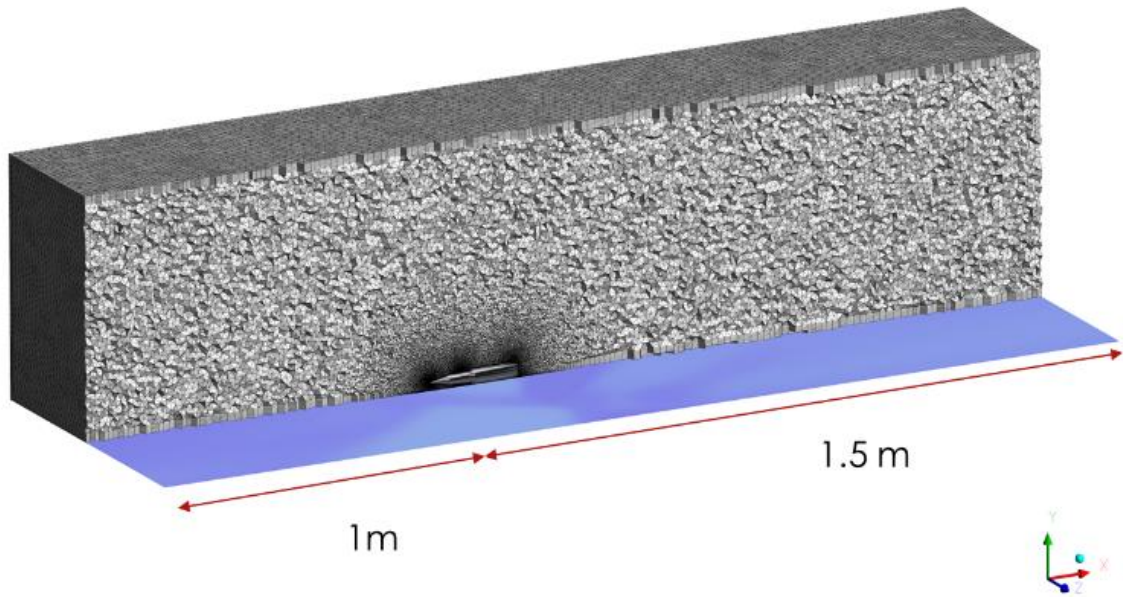

b)

Figure 41: Computational Domain for a) Oscillatory and b) unidirectional flow experiments

The steady-state Reynolds Averaged Navier-Stokes (RANS) equations were solved and are described below. For the turbulence closure, the RNG k-ε turbulence model is adopted. The equations solved using ANSYS Fluent solver 18.0 are as follows

Continuity:

$$\frac{\partial u_i}{\partial x_i} = 0 \; ; \qquad \text{Equation 25}$$

Momentum conservation:

$$\frac{\partial\left(\rho u_i u_j\right)}{\partial x_j} = -\frac{\partial p}{\partial x_i} + \frac{\partial}{\partial x_j}\left[\mu\left(\frac{\partial u_i}{\partial x_j} + \frac{\partial u_j}{\partial x_i} - \frac{2}{3}\delta_{ij}\frac{\partial u_i}{\partial x_i}\right)\right] + \frac{\partial}{\partial x_j}\left(-\rho\overline{u_i' u_j'}\right) + \rho g_i \; , \qquad \text{Equation 26}$$

where ρ is the density (kg/m^3), u_i is the mean velocity component parallel to the x_i coordinate [m/sec], p is the pressure (Pa), μ is the molecular/dynamic viscosity (Pa sec), δ_{ij} is the Kronecker's delta, $\rho\overline{u_i' u_j'}$ is the Reynolds' stress term and ρg_i is the gravity acceleration component parallel to the coordinate (m/sec^2).

For the Reynolds' stresses estimation, a RNG (renormalization group theory) two-equation k-ε turbulence model is used for the closure of the set of equations. According to the RNG k-ε model both turbulence kinetic energy (k) and its dissipation rate (ε) are estimated using a semi-empirical set of transport equations. Thus, the turbulence kinetic energy and the turbulent kinetic energy dissipation rate (ε) are calculated using the following transport equation (ANSYS Inc, 2017):

$$\frac{\partial}{\partial x_j}\left(\rho k\right) = -\frac{\partial}{\partial x_i}\left(\rho k u_i\right) + \frac{\partial}{\partial x_j}\left[\alpha_k \mu_{eff}\frac{\partial\left(k\right)}{\partial x_j}\right] + P_k - \rho\varepsilon + S_k \; ; \qquad \text{Equation 27}$$

$$\frac{\partial}{\partial x_j}\left(\rho\varepsilon\right) = -\frac{\partial}{\partial x_i}\left(\rho\varepsilon u_i\right) + \frac{\partial}{\partial x_j}\left[\alpha_\varepsilon \mu_{eff}\frac{\partial\varepsilon}{\partial x_j}\right] + C_{1\varepsilon}\frac{\varepsilon}{k}P_k - C_{2\varepsilon}\rho\frac{\varepsilon^2}{k} - R_\varepsilon + S_\varepsilon \; , \qquad \text{Equation 28}$$

where P_k is the turbulence kinetic energy production due to the mean velocity gradients ($P_k = -\rho\overline{u_i' u_j'}\frac{\partial u_j}{\partial x_i} = \mu_t S^2$), μ_t is the turbulent (or eddy) viscosity ($\mu_t = \rho C_\mu \frac{k^2}{\varepsilon}$), S is the modulus of the mean strain rate tensor calculated as ($S \equiv \sqrt{2S_{ij}S_{ij}}$),$C_{1\varepsilon}$ and $C_{2\varepsilon}$ are constants, S_k and S_ε are additional source terms for the k, α_k and α_ε are the turbulent Prandtl number for k and ε calculated using the following equation

$$\left|\frac{\alpha-1.3929}{\alpha_o-1.3929}\right|^{0.6321}\left|\frac{\alpha-2.3929}{\alpha_o-2.3929}\right|^{0.3679}=\frac{\mu_{mol}}{\mu_{eff}}, \qquad \text{Equation 29}$$

where α_o =1.0, μ_{mol} is the dynamic or molecular viscosity and μ_{eff} is the effective viscosity. Note that for highly turbulent flows ($\frac{\mu_{mol}}{\mu_{eff}} << 1$) $\alpha_k = \alpha_\varepsilon \approx 1.393$. Finally, ε equations includes the R_ε term which is the RNG term which is calculated as

$$R_\varepsilon=\frac{C_\mu\eta^3\left(1-\eta/\eta_o\right)}{1+\beta\eta^3}\frac{\varepsilon^2}{k}, \qquad \text{Equation 30}$$

where C_μ is a constant, $\eta \equiv Sk/\varepsilon$, η_o is a constant. Note that for $\eta<\eta_o$ R_ε has a positive contribution while for $\eta>\eta_o$ R_ε has a negative contribution increasing the dissipation of ε. RNG model tends to give higher turbulent viscosity values compared to standard *k-ε* model for weakly and moderately strained flows and lower turbulent viscosity for rapidly strained flows (again compared to the standard *k-ε* model). This sensitivity of RNG model for rapid stain and streamline curvature make it superior compared to the standard *k-ε* model for certain flows. The constants of the applied RNG *k-ε* model can be found in Table 9.

Table 9: Constants used for the RNG k-ε

Constants	C_μ	$C_{1\varepsilon}$	$C_{2\varepsilon}$	η_o	β
Value	0.0845	1.42	1.68	4.38	0.012

For the turbulence boundary condition at the walls the "scalable wall functions" approach is adopted (ANSYS Inc., 2017), which for the RNG *k-ε* model is a two-layer model that uses a blending/smoothing function for the turbulent viscosity in order to smoothly switch from the viscous to the high Reynolds number region (Jongen, 1992). This method has no restriction regarding the first near-wall cell height. Scalable wall functions become identical to the standard wall functions when $y^*=\frac{C_\mu^{1/4}k_p^{1/2}y_p}{\nu}>11$.

For the solution of the momentum and pressure terms second order schemes are used for the spatial discretization. For the turbulent quantities a second order schemes are applied. Finally, the velocity-pressure coupling is achieved using the SIMPLE algorithm (Patankar 1980). Convergence criterion for all the partial equations was set 10^{-6}.

In addition to the PIV measurements, numerical modeling is conducted to study the flow structure around munitions, validate the numerical model as well as examine the effect of angle of attack and oscillatory flow properties such as period and amplitude of oscillation on the drag forces that munitions experience. In Figure 42, the comparison between PIV measurements and CFD numerical results is presented for the mean velocity profiles for the case of flow around a 25 mm munition with an angle of attack of 0 degrees and free stream velocity of 0.32 m/sec. The velocity profile used for the numerical modeling was estimated using the PIV measurements at the most upstream end of the examined section and by fitting a logarithmic law distribution. Three characteristic profiles are shown (α., β. and γ.). The comparison between the numerical results and the experimental data agrees well.

Additional simulations were conducted (see section 5.1) to examine the effect of the angle of attack on the flow structure around the munitions as well as the forces that they experience. In Figure 43a, the complex flow structure around a 20 mm munition placed perpendicular to the mean flow (90-degrees angle of attack) is shown together with the relative pressure distribution on the munition. The pressure results show the importance of flow field (stagnation points, flow acceleration etc.) on the forces that the munitions experience. The orientation of the munition alters highly the acceleration/deceleration regions on the surface of the munitions while vortexes are and flow separation significantly change the pressure/force distribution on the munitions. Figure 43b and Figure 43c also present the flow velocity vectors in two characteristic slices of the flow. Both the figures show the strong recirculation and secondary flows behind the munition.

Similar modeling analysis was conducted for the case of oscillatory flow. In Figure 44, the comparison between numerical results and experimental data is presented for the case of IMU munition placed over a very rough/gravel bed (U_{max}=0.22 m/sec, T=10 sec). The comparison between the numerical results and the experimental data agrees well.

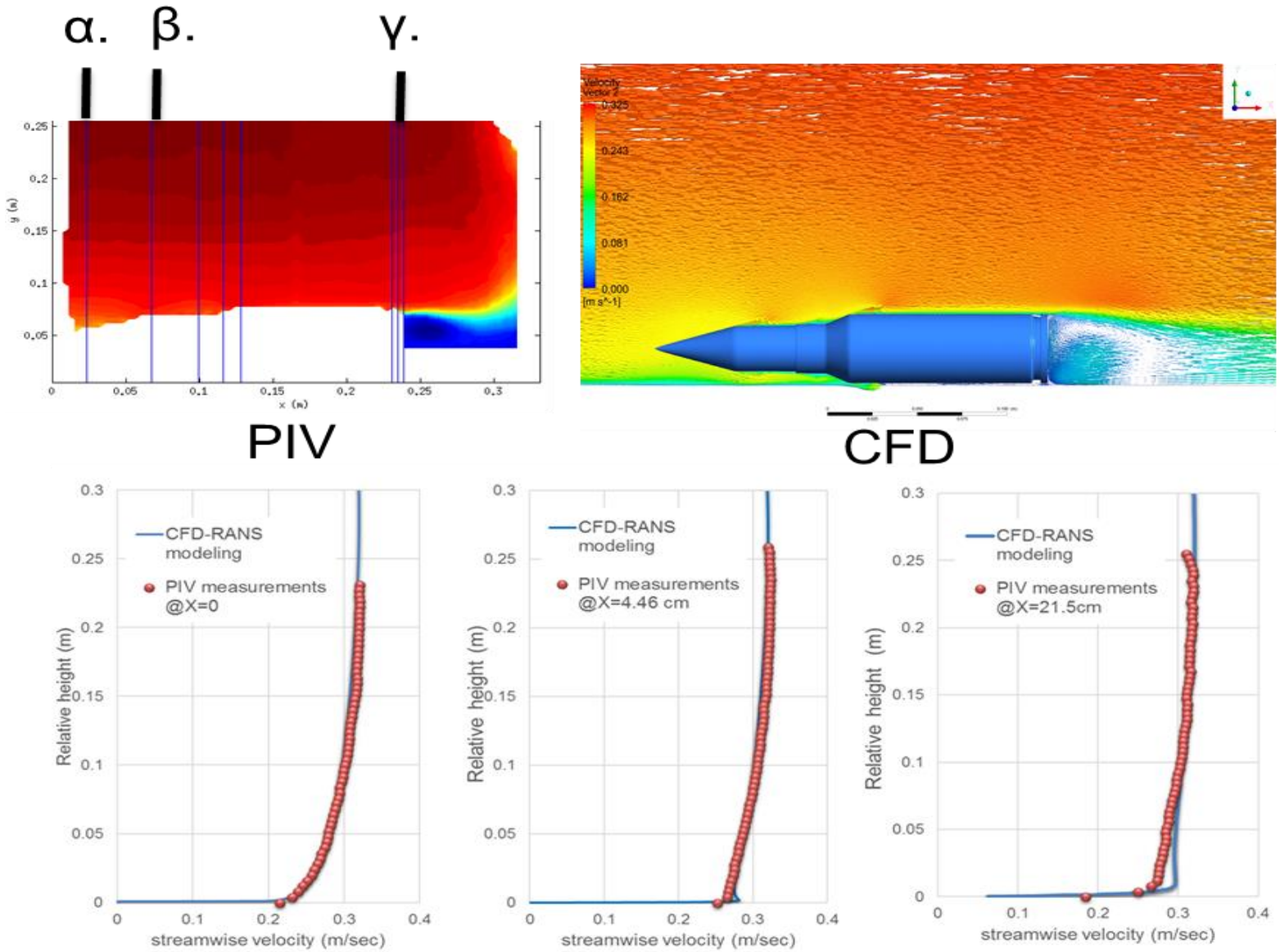

Figure 42: Comparison between PIV measurements and CFD results for the case of unidirectional flow.

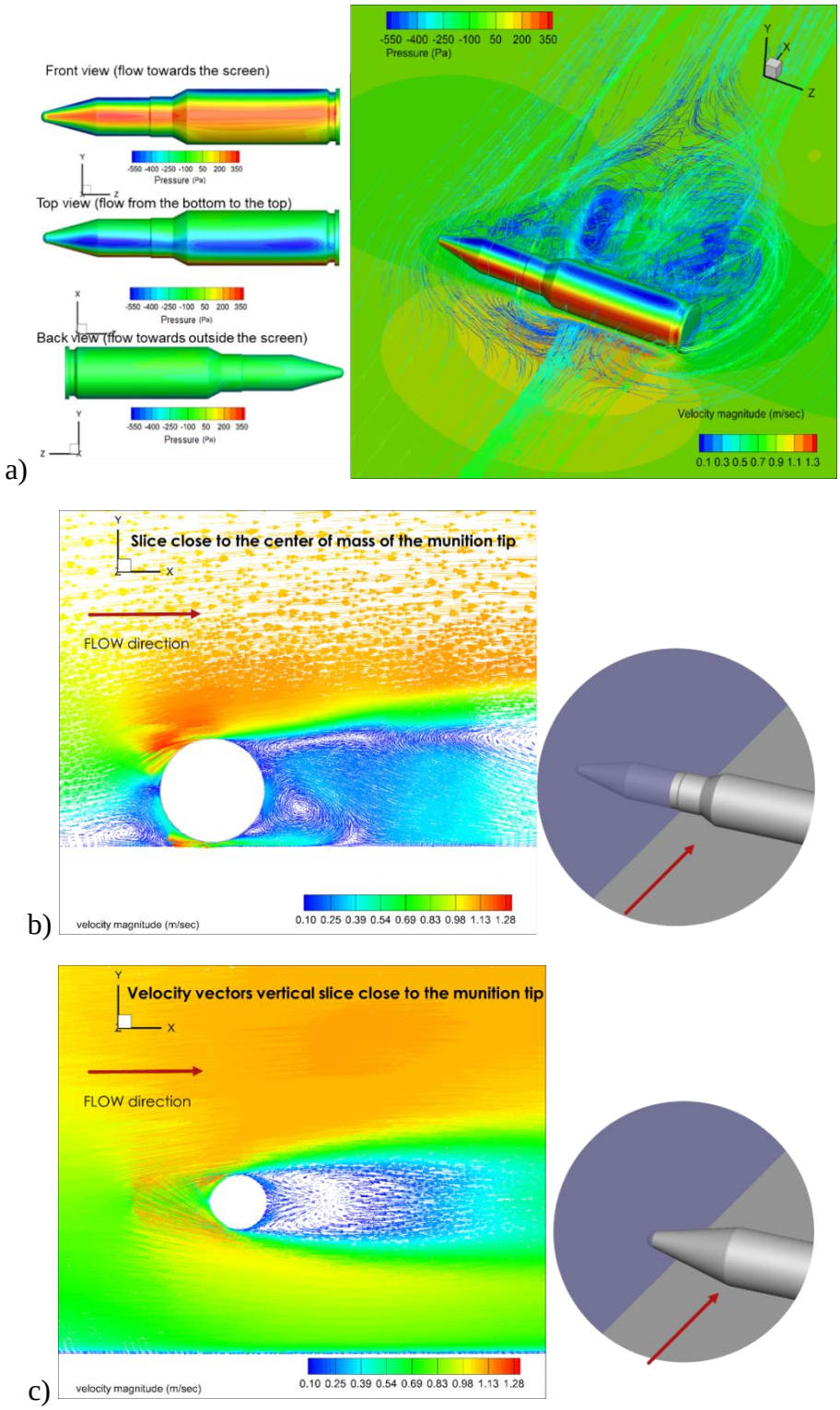

Figure 43: CFD results for the case of unidirectional flow: a) complex flow pattern and relative pressure field distribution on the munition surface b) velocity vectors for a slice close to the center of mass of the 20 mm munition c) velocity vectors for a slice close to the tip of the 20 mm munition

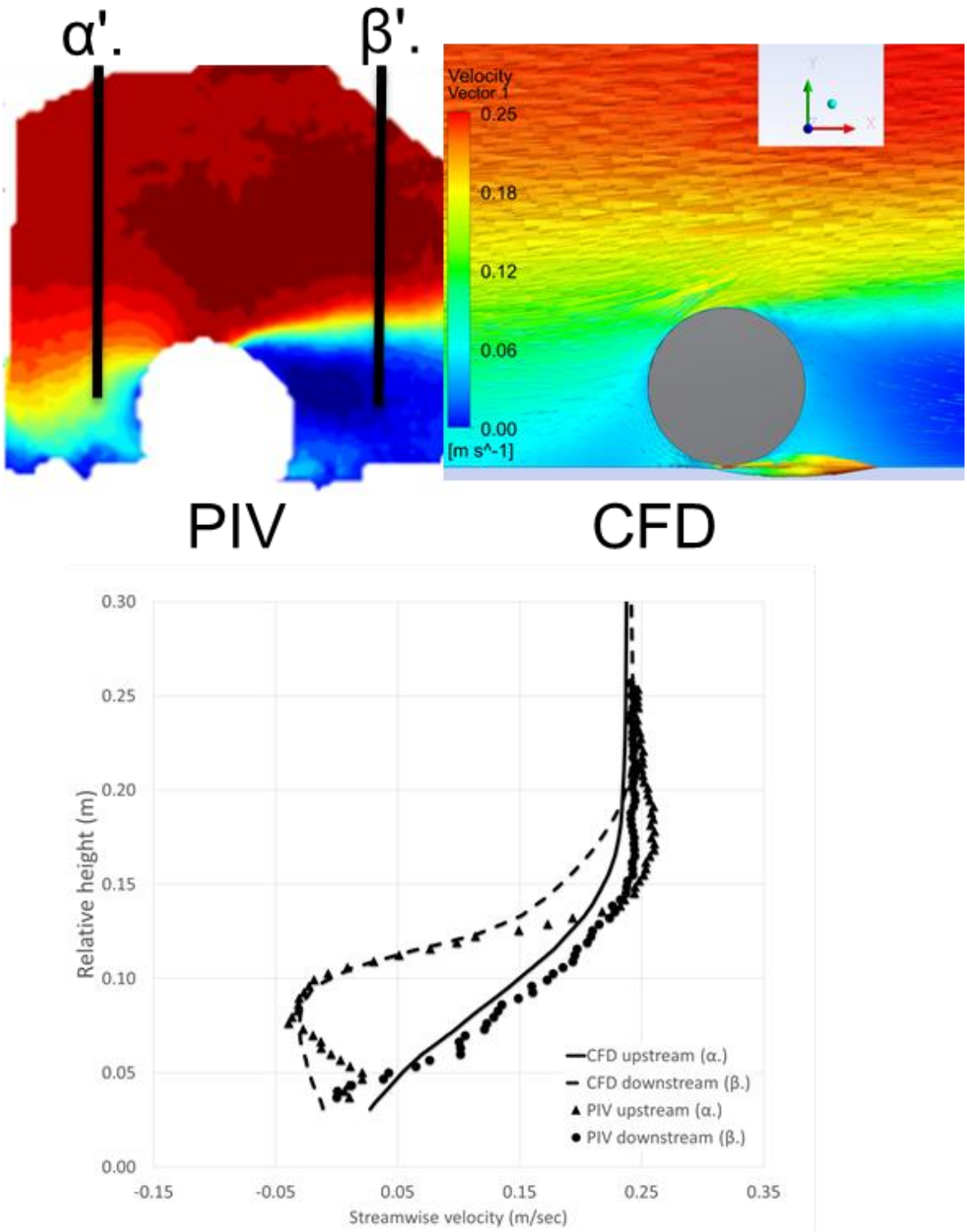

Figure 44: Comparison between PIV measurements and CFD results for the case of oscillatory flow.

Appendix G: Python Script in a Jupyter Notebook for Initiation of Munition Motion on Hard Substrates

An interactive tool for the prediction of the initiation of motion of objects under Currents and Waves

MR-2410 Large-Scale Laboratory Experiments of Incipient Motion, Transport, and Fate of Underwater Munitions under Waves, Currents, and Combined Flows, PI: Marcelo H. García & Blake Landry

interface developed by Dimitrios K. Fytanidis & Heng Wu

In [1]:
```
import matplotlib.pyplot as plt
%matplotlib inline
import  numpy as np
import scipy
from ipywidgets import *
import ipywidgets as widgets
import csv
```

In [2]:
```
def CriticalF3(projectile,Angle,Roughness,U,T,H):
    viscosity=1.79e-6/(1+0.03368*T+0.00021*T**2);
    density=1000*(1-((T+288.9414)*(T-3.9863)**2)/(508929.2*(T+68.12963
)));
    Roughness=Roughness/1000

    if (projectile == 20):
        d       = 2683.53
```

```
        Parea   = 6E-11*(Angle**5) - 1E-08*(Angle**4) - 2E-06*(Angle**
3) - 0.0002*(Angle**2) + 0.0947*(Angle) + 0.9608 #in inch^2
        Parea   = 0.00064516*Parea #inch^2 to m^2
        volume  = 7.60627E-05 #m^3
        l=(Parea**2)/volume
    if (projectile == 25):
        d=2374.73
        Parea   = -1E-20*(Angle**5) + 3E-08*(Angle**4) - 1E-05*(Angle*
*3) + 0.0002*(Angle**2) + 0.1443*(Angle) + 1.6231
        Parea   = 0.00064516*Parea #inch^2 to m^2
        volume  = 0.000164266 #m^3
        l=(Parea**2)/volume
    if (projectile == 81):
        d=3293.63
        Parea   = -5E-20*(Angle**5) + 2E-07*(Angle**4) - 6E-05*(Angle*
*3) + 0.0027*(Angle**2) + 0.5566*(Angle) + 7.1652
        Parea   = 0.00064516*Parea #inch^2 to m^2
        volume  = 0.00118441 #m^3
        l=(Parea**2)/volume

    if(T==0):
        eta= 0.01*H*(U*H/viscosity)**(-3/4)
        fi=1
    else:
        eta= 0.01*np.sqrt(viscosity*T/np.pi)
        fi=(1+4*np.pi*2/(U*T/(volume/Parea)))**(1/2)

    s=Roughness+eta
    #F3=((H/s)**(-0.5))*
    FF3=(H/(np.maximum(Roughness,1.5E-05)))**(-0.5)*U*fi/np.sqrt(9.81*
(d-density)/d*np.maximum(l,1.5E-05))

    xx=np.linspace(0.0001,100000,10)
    yy=0.1709*(xx)**(-0.6311)

    if(FF3>0.1709*(l/s)**(-0.6311)):
        flag='red'
    elif( FF3 <( 0.1709*(l/s)**(-0.6311))/0.46730896 and  FF3 > ( 0.17
09*(l/s)**(-0.6311))*0.46730896 ):
        flag='darkorange'
    else:
        flag='blue'
    ils = np.zeros(393)
    if1 = np.zeros(393)
    if2 = np.zeros(393)
    if3 = np.zeros (393)
    y=np.zeros(50)
    i=0
    with open('Figure24.csv') as csvfile:
        readCSV = csv.reader(csvfile, delimiter=',')
```

```
        for row in readCSV:
            #l_s=np.append(row[0])
            #print(row[0])
            #print(row[0],row[1],row[2],)
            a = row[0]
            b = row[1]
            c = row[2]
            d = row[3]
            ils[i]=a
            if1[i]=b
            if2[i]=c
            if3[i]=d
            i=i+1
    plt.scatter(ils,if3,marker ='o',color='lightgrey',s=15)
    plt.plot(xx,yy,color='black',label="Empirical Curve")
    plt.plot(xx,yy*0.6836000655668103*0.6836000655668103,color='lightg
rey',label="Empirical Curve")
    plt.plot(xx,yy/0.6836000655668103/0.6836000655668103,color='lightg
rey',label="Empirical Curve")

    plt.scatter(l/s, FF3, marker ='o',color=flag)
    plt.xlabel(r'$\ell/s$')
    plt.ylabel(r"$\Phi_{l}= f_{I}U_{cr}/\sqrt{g'\ell}$")
    plt.yscale('log')
    plt.xscale('log')
    plt.xlim(0.1, 100000)
    #plt.ylim(0.0001, 10)
    plt.show()
    #print ("taumax =", taumax,',','Failure:', failureflag)
    print()


    return 'done'
print ('done')
```

```
done
```

In [3]:
```
CriticalF3(81,0,0.1,0.1,0,10) #(projectile,Angle,RoughnessInMM,U,T,H)
```

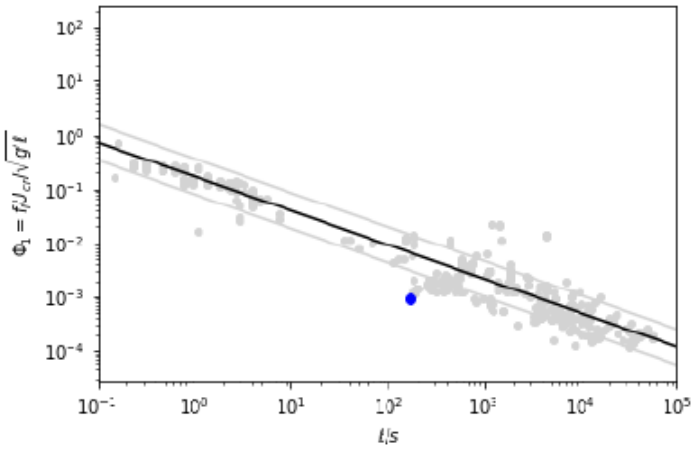

Out[3]: 'done'

In [6]:
```
style = {'description_width': 'initial'}
interact_manual(CriticalF3,projectile=[20, 25, 81],
                Angle=widgets.FloatSlider(min=0.,max=180.,description=
'angle of attack (degrees)',style=style),
                Roughness=widgets.FloatText(min=0,step=0.001,descripti
on='Roughness (in mm)',style=style),
                U=widgets.FloatText(step=0.01,value=0.01,description='
near munition velocity (in m/sec)',style=style),
                T=widgets.FloatSlider(min=0.,max=15.0,step=0.01,descri
ption='Period (in sec)',style=style),
                H=widgets.FloatSlider(min=0.5,max=20,step=0.01,descrip
tion='water depth (in m)',style=style))
```

Out[6]: <function __main__.CriticalF3>